SAPIENZA
UNIVERSITÀ DI ROMA

Quantum Dots for Quantum Networks

Facoltà di Scienze Matematiche Fisiche e Naturali
Scuola Dottorale in Scienze Astronomiche, Chimiche, Fisiche, Matematiche e della Terra "Vito Volterra"

Dottorato di Ricerca in Fisica – XXXIII Ciclo

Candidate

Michele Rota
ID number 1276713

Thesis Advisor

Prof. Rinaldo Trotta

2020/2021

Thesis defended on 21/05/2021
in front of a Board of Examiners composed by:

Prof. Stefano Lupi (chairman)

Prof. Dario Gerace

Dr.ssa Miriam Vitiello

Quantum Dots for Quantum Networks
Ph.D. thesis. Sapienza – University of Rome

This thesis has been typeset by LaTeX and the Sapthesis class.

Author's email: michele.rota@uniroma1.it

Abstract

Single and entangled photon sources are fundamental building blocks of future light-based quantum technologies such as quantum communication, optical quantum computing, and, more in general, for quantum networks. Despite the high number of photon sources proposed over the last years, their exploitation in quantum optical technologies has been limited so far. One of the main reasons for this is that the envisioned applications set very stringent requirements on the properties of the photon source to be used. An ideal photon source should provide single and entangled photons deterministically, with high purity, high efficiency, high indistinguishability, and, in the case of entangled photons, a high degree of entanglement. Among the different photon sources available to date, semiconductor quantum dots (QDs) are arguably one of the most promising.

A QD is a nanometric crystalline structure capable of confining the wavefunction of charge carriers in a semiconductor in all three dimensions. The discrete, atom-like states forming due to confinement can be exploited for the emission of single photons and, in specific conditions, entangled photon pairs. QDs can be grown in a variety of semiconductor combinations. This feature, together with the possibility to tune their optoelectronic properties by changing their physical dimensions and/or via the application of external fields, allows for the control of their light emission with high precision over a broad spectral range. Over the years, several demonstrations of a QD-based source meeting the requirements of the wish-list appeared in the literature. The best source is yet to be disclosed though, as not all the requirements were reached simultaneously in the same experiment.

The work performed during my Ph.D. aims to test the suitability of QDs as sources of entangled photons for future quantum networks. The thesis focuses on the fabrication and study of near-ideal nanophotonic devices based on GaAs QDs fabricated by droplet etching and their exploitation in advanced quantum optics experiments.

In the first part, I will show and discuss the demonstration of quantum teleportation and entanglement swapping using single and entangled photons generated quasi-deterministically from a single GaAs QDs. More specifically, in the teleportation experiment a single quantum state is transferred from one photon to another via an entangled photon pair. In the entanglement swapping instead, the interference of two photons coming from two different entangled pairs is exploited to transfer entanglement to the remaining two, previously uncorrelated, photons. These two experiments represented the first benchmark to test the suitability of QDs for quantum communication, as the two quantum protocols lay at the base of a fundamental element of a quantum network, i.e., the quantum repeater. The

obtained results highlighted that additional improvement of the photon source is still needed to optimize the fidelity of the protocols, especially for what concerns photon-indistinguishability and -extraction efficiency. For this reason, in the second part of the thesis great efforts have been devoted to the fabrication of photonic devices.

The photonic structure we investigated, i.e., a circular Bragg resonator, consists of a single QD in the center of a central cylindrical cavity surrounded by a circular Bragg grating. It features a modest Purcell enhancement with a broadband resonance and an improved extraction efficiency. Record-high values of indistinguishability and brightness were recently reported in the literature using this structure. Building upon these results, we decided to make an additional step and integrate this photonic device onto micro-machined piezoelectric actuators. This is needed to achieve full control over the QD electronic structure and generate entangled photons with near-unity fidelity and tunable energy. The fabrication of the full device requires several steps: It starts from the epitaxial growth of the semiconductor sample containing the GaAs QDs which is reduced into a semiconductor membrane via wet-chemical etching. A patterned mask is then written on it using electron beam lithography and transferred on the membrane through reactive ion etching. In parallel, we also built an imaging setup to locate the position of the QDs across the wafer allowing us to position the cavity around a single QD with nanometric precision. We fabricated the first photonic cavities onto micro-machined piezo-actuators and, in the very last part of this thesis, we report the first experiments using them as sources of light.

Contents

List of Figures

Chapter 1

Toward a solid-state based quantum network: an introduction

The 21st century has been characterized by a steep increase in the number of long distance connections among people, a phenomenon which never occurred in this proportion in known human history. The long distance communication advances started with the invention of the telegraph in the 19th century, continued throughout the 20th century with the appearance of more and more sophisticated ways of communicating over long distances and peaked with the development of the computer and its connection to the internet.

Networks to share information grew steadily in terms of number of users and connections but exploded after the beginning of mass production of affordable cellphones able to connect to the internet. Alongside the growth of information exchange, increased the need of secure ways to exchange sensitive data like bank transactions and private communications. Secure communication is nowadays insured by ciphers based on public-key cryptography protocols [1]. The strength of the protocols relies mainly on the impossibility of a brute force attack due to insufficient computational power of a potential attacker, while man-in-the-middle attacks are prevented with the use of certificates released by trusted organizations.

The cryptography game changed after scientists started to realize the potential enclosed in the application of quantum mechanics to the world of the informatics. Since the publication of the Schor's algorithm [2], it was clear that with the advent of quantum computing, the difficulties of factorizing prime numbers, upon which most of the secure protocols are based, were going to be soon removed. But if quantum mechanics ruined the party of secure communications it could also help in setting it

back. Together with quantum computation, came also quantum cryptography, with the appearance of quantum key distribution protocols [3, 4]. What the quantum mechanics added to the plot is that a cryptographic key distribution based on the exchange of quantum states provides an intrinsically secure method of sharing a key, which can then be used to encrypt messages through an authenticated but potentially wiretapped channel. If an eavesdropper tries to intercept a quantum secret signal traveling between two locations, the quantum state, in which the information is encoded, is measured and the presence of the unwanted guest will be noticed, provided that some requirements on the protocol are met. In future networks then, alongside the classical communication links, quantum channels must be present, together with devices capable of producing and manipulating quantum states, combined in the creation of a quantum network. As we will see, the adjective quantum not only means that the information is encoded in quantum states but also that the system exploits the most peculiar properties of a quantum system, namely: superposition and entanglement.

1.1 The quantum repeater

Independently of the platform that will be used for the different nodes and links of a quantum network it is widely accepted that photons are the best candidates for the role of flying quantum bits to interface distant nodes. Photons feature interesting properties such as low decoherence over long distances, they can be manipulated and detected with the use of commercially available technology, and their several degrees of freedom, i.e., polarization, orbital momentum, path, time-bin, can be used to encode quantum information [5]. So, from now on, when we speak about a quantum state, we will mean a single photon and vice-versa, with the quantum information encoded in one or more of its degrees of freedom. In the most simple quantum link, the sender, named Alice, would simply send a photon with information encoded, e.g., in the polarization degree of freedom, to the receiver, Bob. If they want to share entanglement instead, Alice could create an entangled pair of photons, store one of them and send the other to Bob through the same link.

This simplistic picture falls short when we want to establish efficient communication between nodes which are at a distance of kilometers or higher [6]. One major drawback concerning light is that, as opposed to radio waves, it cannot be sent over long distances without being completely absorbed or scattered. Fiber optics offers the best option for long distance communications but, even in the most favorable conditions, i.e., in pure silica core fibers at 1550 nm wavelength, the lowest loss observed of $0.15\,\mathrm{dB\,km^{-1}}$ [7, 8] leads to a 50% attenuation of the signal after only

20 km of travel distance.

When dealing with classical signals, optical amplifiers are routinely used, allowing, for example, the over 3000 km long optical link laid on the bed of the Atlantic ocean. With the amplification of a quantum signal the situation changes dramatically. A hard constraint in quantum signal amplification is set by the non-cloning theorem [9], which states that a single quantum state cannot be copied and, consequently, cannot be amplified. This theorem comes directly from the collapse of the wavefunction of a quantum state when interacting with a probe. After a measurement is performed the quantum state will be found in the basis wavevector corresponding to the result of the measurement. The probabilistic nature of the measurement means that part of the information enclosed in the state before measurement is lost, making impossible to reconstruct an unknown generic state by measuring a single copy of it, and thus preventing its replication and amplification.

The solution to circumvent the amplification blockade comes again from the quantum world: By exploiting the non-locality properties of entangled states in a quantum repeater. By combining a procedure known as teleportation, with devices capable of storing a quantum state, a quantum repeater can increase the distance that a quantum signal can travel without suffering from hindering losses [10–14].

1.2 Entanglement and state teleportation

In the framework of quantum mechanics it is possible to construct, without much theoretical difficulty, a two-particle quantum state, e.g., the polarization part of a two-photon state in the basis of two orthogonal states of polarization $|0\rangle$ and $|1\rangle$, which cannot be described as the tensor product of a state of particle 1 and the state of particle 2:

$$|\psi\rangle_{12} = \frac{1}{\sqrt{2}} \left(|1\rangle_1 |0\rangle_2 + |0\rangle_1 |1\rangle_2 \right) \tag{1.1}$$

such a state is called non separable or entangled. By looking at Eq. 1.1 we can clearly see that if a measurement of the polarization state of photon 1 gives $|1\rangle$ as a result we know for sure that the other photon will be found in state $|0\rangle$ and vice-versa, if the measurement gives as a result $|0\rangle$. By carefully preparing the experiment we can ensure that the distance between the measurements is space-like, i.e., the two points cannot be linked by a ray of light and share no causality relations. Such an experiment apparently violates the principles of special relativity, since the result of a measurement immediately affects the state of the other part of the system. We will see in the following paragraphs that no superluminal communication is possible and causality is preserved.

This "spooky" feature [15] of quantum mechanics started bitter discussions in the scientific community about the completeness of quantum mechanics [16, 17] until J.S. Bell imagined an experiment in which a local-hidden variables theory and a non-local quantum mechanics theory would have produced different results. To test the nature of reality, Bell wrote a set of inequalities [18] whose violation or confirmation would have told if quantum mechanics is a non-local theory or has hidden variables. The first experimental test of the Bell's theorem were performed in 1981 by Aspect *et al.*, as soon as technological advances made possible to have efficient emitters of entangled photons [19–21]. Their measurements violated Bell's inequality by more than 9 standard deviations, and represented a first proof of non-locality. Over the years, several objections about possible loopholes in the demonstration of the inequalities were presented and more and more refined experiments closed one by one each of the loopholes until recently, when a loophole-free demonstration was claimed [22, 23], eventually setting the argument over the nature of reality.

We can see that for the Hilbert space of two two-photon states the number of independent entangled states is 4. These states are called Bell states, for obvious reasons, and, in the computational base, can be written as:

$$\begin{aligned}
|\phi^+\rangle &= \frac{1}{\sqrt{2}}\left(|0\rangle_1|0\rangle_2 + |1\rangle_1|1\rangle_2\right) \\
|\phi^-\rangle &= \frac{1}{\sqrt{2}}\left(|0\rangle_1|0\rangle_2 - |1\rangle_1|1\rangle_2\right) \\
|\psi^+\rangle &= \frac{1}{\sqrt{2}}\left(|0\rangle_1|1\rangle_2 + |1\rangle_1|0\rangle_2\right) \\
|\psi^-\rangle &= \frac{1}{\sqrt{2}}\left(|0\rangle_1|1\rangle_2 - |1\rangle_1|0\rangle_2\right)
\end{aligned} \tag{1.2}$$

These states are an orthogonal set and form a complete basis for the Hilbert space.

The key idea of a quantum repeater [24] is that entanglement can be created between the two nodes at a distance L by subdividing it in several segments and establishing entanglement in all of them independently, see Fig. 1.1(a). Once entanglement is established between the end of each segment, we can extend the distance at which the entanglement is shared by swapping the entanglement [25] between adjacent nodes, see Fig. 1.1(b). A cascade of entanglement swappings, can increase the distance between the entangled nodes until the ending nodes of the channel are in an entangled state, see Fig. 1.1(c).

This scheme alone does not increase the transmission rate in the channel, as the losses summed over all the segments are still exponential with the total length L. In order for this scheme to work we need a way to tell when entanglement is established in a segment, so that we know when to start the entanglement swapping cascade, and quantum memories capable of storing the entangled photons while

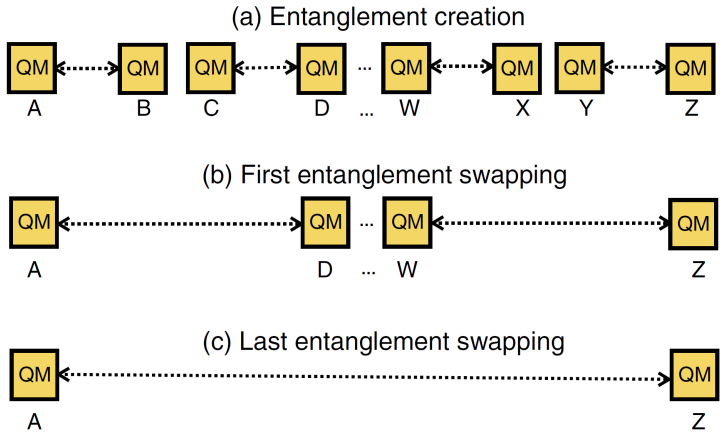

Figure 1.1. Principle of a quantum repeater. (a) Entanglement (dotted line) is first created independently in each segment of the link, and the photons are stored in quantum memories (QM). (b) Entanglement is swapped between neighboring links. (c) Entanglement swapping operations are performed successively in a nested hierarchical procedure until the entanglement is distributed between the two ending nodes of the link. From Ref. [10].

we wait that entanglement is established in all the links. If the two conditions we described subsist, we are able reduce the losses in a channel from an exponential law to a polynomial one [10].

1.2.1 Entanglement teleportation

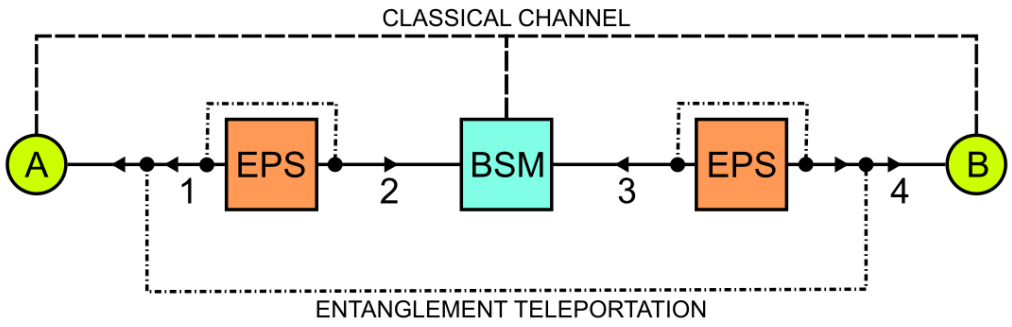

Figure 1.2. Entanglement teleportation scheme. The entangled photon source (EPS) is in an orange box. The Bell state measurement device (BSM) is in a light blue box. Photons travelling in the quantum channel are depicted as solid arrowed lines, the classical channel is depicted with a broken line. The transfer of entanglement is depicted with a dash-dot line.

To transfer entanglement to two distant, uncorrelated photons with entanglement swapping [25] we need two pairs of entangled photons. We use two entangled photon

sources (EPS), see the scheme of Fig 1.2, each emitting a pair of entangled photons, e.g., in the $|\phi^+\rangle$ state. The joint four-photon state can be written as:

$$|\Psi\rangle_{1234} = |\phi^+\rangle_{12} \otimes |\phi^+\rangle_{34} = \frac{1}{2}\left(|0\rangle_1 |0\rangle_2 + |1\rangle_1 |1\rangle_2\right) \otimes \left(|0\rangle_3 |0\rangle_4 + |1\rangle_3 |1\rangle_4\right) \quad (1.3)$$

Since the Bell states are a complete base for any two-photon state we can rewrite the joint 4-photon polarization state in the basis of Bell states linking photons 2-3 and 1-4:

$$|\Psi\rangle_{1234} = |\psi^+\rangle_{23} |\psi^+\rangle_{14} + |\psi^-\rangle_{23} |\psi^-\rangle_{14} + |\phi^+\rangle_{23} |\phi^+\rangle_{14} + |\phi^-\rangle_{23} |\phi^-\rangle_{14} \quad (1.4)$$

When we make a measurement on the state of photon 2 and 3 in the basis of the Bell states, photons 1 and 4 will always be projected on an entangled state, despite never having been correlated before. In particular, if the photons state is projected on $|\psi^-\rangle_{23}$ with a measurement, the remaining photons 1-4 will be left in the same $|\psi^-\rangle$ state. The result of performing a Bell state measuremente (BSM) on photons 2-3 is then to transfer the entanglement from the photons 1-2 and 3-4 to the photons 1-4 and 2-3, explaining the name of swapping. An alternative way of seeing the procedure, which highlights the quantum communication side, is that we have teleported entanglement which was shared by two local couples of photons onto photons that are in the remote locations A and B.

It is important to stress that, in order to use the new entangled couple, information must be shared on the result of the BSM. Only in this case we know which type of correlations to expect between the photons in the two distant sites. The need of classical information exchange ensures the impossibility to send signals at a superluminal speed.

1.2.2 State teleportation

With a state teleportation [26], see scheme in Fig. 1.3, we can transfer the generic state of photon 1 from A to B by performing a BSM between the initial photon and one of the two photons of an entangled pair. We can write the generic polarization state of the target photon 1 as a linear combination of orthogonal polarizations, e.g., in the linear basis HV:

$$|\varphi\rangle_1 = a\,|0\rangle_1 + b\,|1\rangle_1 \quad (1.5)$$

where the normalization of the state is ensured by $|a|^2 + |b|^2 = 1$. We now take a pair of entangled photons, again in the $|\phi^+\rangle$ state. The entangled pair could be stemming from an EPS or could be shared by two distant nodes as a result of an entanglement swapping procedure. The three-photon state of the entangled pair

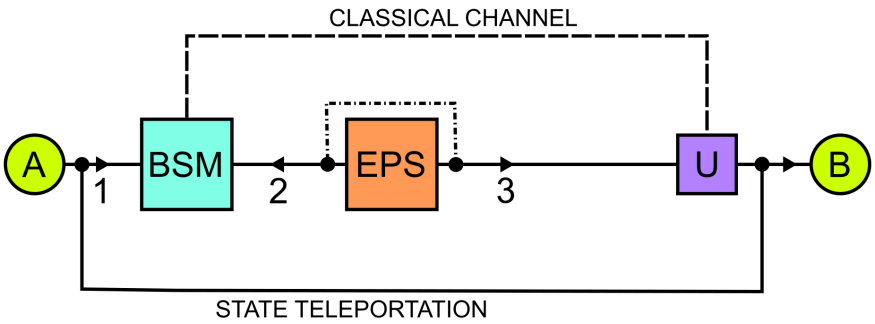

Figure 1.3. State teleportation scheme. The entangled photon source (EPS) is in an orange box. The Bell state measurement device (BSM) is in a light blue box. Photons travelling in the quantum channel are depicted as solid arrowed lines, the classical channel is depicted with a broken line. The entanglement is depicted with a dash-dot line.

and the incoming photon can be written as the direct product of the two separated states:

$$|\Psi\rangle_{123} = |\phi^+\rangle_{23} \otimes |\varphi\rangle_1 = \frac{1}{\sqrt{2}} \left(|0\rangle_2 |0\rangle_3 + |1\rangle_2 |1\rangle_3\right) \otimes \left(a |0\rangle_1 + b |1\rangle_1\right) \tag{1.6}$$

The joint state can be rewritten as a linear combination in the basis of the 4 Bell states of photons 1 and 2 as:

$$\begin{aligned} |\Psi\rangle_{123} = \frac{1}{2} \Big(& |\phi^+\rangle_{12} \left(a |0\rangle_3 + b |1\rangle_3\right) + \\ & + |\phi^-\rangle_{12} \left(a |0\rangle_3 - b |1\rangle_3\right) + \\ & + |\psi^+\rangle_{12} \left(b |0\rangle_3 + a |1\rangle_3\right) + \\ & + |\psi^-\rangle_{12} \left(b |0\rangle_3 - a |1\rangle_3\right) \Big) \end{aligned} \tag{1.7}$$

If we now perform a BSM on the state $|\varphi\rangle_{12}$, we will project (or teleport) the polarization state of photon 1 onto photon 3, with a rotation. This rotation can be best seen by expressing the state of Eq. 1.7 in terms of Pauli matrices:

$$|\Psi\rangle_{123} = \frac{1}{2} \left(|\phi^+\rangle_{12} \hat{\sigma}_0 + |\psi^+\rangle_{12} \hat{\sigma}_x + i |\psi^-\rangle_{12} \hat{\sigma}_y + |\phi^-\rangle_{12} \hat{\sigma}_z\right) |\varphi\rangle_3 \tag{1.8}$$

As an example let us see what happens if the BSM device detects a $|\psi^-\rangle_{12}$ Bell state. This is equivalent to projecting the 1-2 modes of the three-photon state on the wavevector $\langle\psi^-|$. The remaining photon will be then left in the state,

$$|\varphi\rangle_3 = i |\psi^-\rangle_{12} \hat{\sigma}_y = b |0\rangle_3 - a |1\rangle_3 \tag{1.9}$$

if we apply the unitary transformation

$$\hat{U} = \begin{pmatrix} 0 & 1 \\ -1 & 0 \end{pmatrix} \tag{1.10}$$

on the photon 3, for example with a combination of two half-waveplates with the fast axis at an angle of 0° and 45° with respect to the H axis respectively, we can retrieve the original state:

$$\hat{U} |\varphi\rangle_3 = \begin{pmatrix} 0 & 1 \\ -1 & 0 \end{pmatrix} (b |0\rangle_3 - a |1\rangle_3) = a |0\rangle_3 + b |1\rangle_3 \tag{1.11}$$

It is important to stress again that, in order to obtain the exact copy of the state, two classical bits of information on the outcome of the BSM must be sent in order to choose which unitary transformation to apply to get back the original state.

1.2.3 Bell state measurement

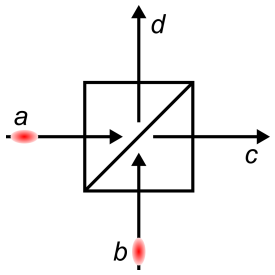

Figure 1.4. Schematic representation of a beamsplitter. A single photon (red torpedo) approaches each input port a and b. The possible outcomes of photon coincidences from output ports depend on the symmetry of the two-photon state wavefunction.

As we have seen in the previous paragraphs, one of the two cores of the teleportation protocols is a device capable of efficiently measuring the Bell state of two photons. Such a device is, at least for a partial measurement of the set of Bell states, rather simple, consisting of a balanced beamsplitter and two single photon detectors. The behavior of single photons interacting with a beamsplitter is non-trivial, as phenomena of quantum interference may appear, depending on the symmetry of their wavefunctions.

Referring to Fig. 1.4, a single photon impinging on the entrance a or b of a balanced beamsplitter will come out in a superposition state of the two exit ports

modes c and d:

$$|a\rangle \rightarrow \frac{1}{\sqrt{2}}\left(|c\rangle + i\,|d\rangle\right) \tag{1.12}$$

$$|b\rangle \rightarrow \frac{1}{\sqrt{2}}\left(i\,|c\rangle + |d\rangle\right) \tag{1.13}$$

Gaining a π phase when reflected and no phase change when transmitted.

Two-photon interference

If we now let two photons with the same frequency and wavepacket impinge each on one of the two entrance ports a and b, depending on the particular symmetry of their joint state, we have two different behaviors: If the two photons entering the beamsplitter have the same energy and wavepacket, we have no way of telling which path each photon took and their state must then be a normalized superposition of the two possible cases $|a\rangle_1 |b\rangle_2$ and $|b\rangle_1 |a\rangle_2$ with a plus/minus if their wavefunction is symmetric/anti-symmetric:

$$|\varphi\rangle_g = \frac{1}{\sqrt{2}}\left(|a\rangle_1 |b\rangle_2 + |b\rangle_1 |a\rangle_2\right) \rightarrow \frac{i}{\sqrt{2}}\left(|c\rangle_1 |c\rangle_2 + |d\rangle_1 |d\rangle_2\right) \tag{1.14}$$

$$|\varphi\rangle_u = \frac{1}{\sqrt{2}}\left(|a\rangle_1 |b\rangle_2 - |b\rangle_1 |a\rangle_2\right) \rightarrow \frac{1}{\sqrt{2}}\left(|c\rangle_1 |d\rangle_2 - |d\rangle_1 |c\rangle_2\right) \tag{1.15}$$

From Eqs. 1.14 and 1.15 we see that two photons entering the beamsplitter with a symmetric (g) spatial (and spin) wavefunction will always come out from one output of the beamsplitter together, whereas if both their spatial and spin wavefunction are anti-symmetric (u) they will never come out together from the same port, but always separated. The former case is known in literature as the Hong-Ou-Mandel effect [27] and it is a quantum phenomenon of a two-photon interference [28]. Its exploitation gives us a powerful tool to measure the indistinguishability of photons emitted by a source of singe photons. We will see its use in section 2.1.3.

To measure a two-photon state in the basis of the four Bell states we can exploit the different behaviors of Bell states when the two photons that make up the state impinge one in each entrance of a balanced beamsplitter [29]. By looking at the four Bell states in Eq. 1.2, describing the polarization state of two photons, we see that we can discriminate between them by looking at their symmetry under exchange of particles. The $|\psi^-\rangle$ is the only state which is anti-symmetric under exchange of particles, while the other three are symmetric. Since photons are bosons, their total wavefunction must be symmetric under under exchange of labels. If we write the

Bell states including also the spatial part of the wavefunction:

$$
\begin{aligned}
|\phi^+\rangle &= \frac{1}{\sqrt{2}} \left(|0\rangle_1 |0\rangle_2 + |1\rangle_1 |1\rangle_2\right) \left(|a\rangle_1 |b\rangle_2 + |b\rangle_1 |a\rangle_2\right) \\
|\phi^-\rangle &= \frac{1}{\sqrt{2}} \left(|0\rangle_1 |0\rangle_2 - |1\rangle_1 |1\rangle_2\right) \left(|a\rangle_1 |b\rangle_2 + |b\rangle_1 |a\rangle_2\right) \\
|\psi^+\rangle &= \frac{1}{\sqrt{2}} \left(|0\rangle_1 |1\rangle_2 + |1\rangle_1 |0\rangle_2\right) \left(|a\rangle_1 |b\rangle_2 + |b\rangle_1 |a\rangle_2\right) \\
|\psi^-\rangle &= \frac{1}{\sqrt{2}} \left(|0\rangle_1 |1\rangle_2 - |1\rangle_1 |0\rangle_2\right) \left(|a\rangle_1 |b\rangle_2 - |b\rangle_1 |a\rangle_2\right)
\end{aligned} \tag{1.16}
$$

we see that the spatial part of a $|\psi^-\rangle$ state must be anti-symmetric as well, for the complete state to be symmetric, while the remaining Bell states feature a symmetric spatial wavefunction.

The simplest BSM device consist of a balanced beamsplitter, two single photon detectors (SPD), and the electronics to correlate the signal coming from the SPD. Such a device is sketched Fig. 1.5(a). When a $|\psi^-\rangle$ state enters the BSM setup we will observe an increase in the coincidences rate with respect to temporally detuned photons. In the case of a $|\phi^\pm\rangle$ and $|\psi^+\rangle$ state, with a symmetric wavefunction, both photons are coming out of the same output of the beamsplitter and a drop in the coincidences will be observed. It is clear that this simple device is only able to project on a $|\psi^-\rangle$ state. Its theoretical efficiency (without considering losses and noise) is then 25%, as all the events originating from the other three Bell states cannot be discriminated against each other. With a small effort in terms of setup complexity, a 50% efficiency BSM can be implemented, see Fig. 1.5(b), by adding two polarizing beampsplitters and two detectors more. In this case, all the $|\psi^+\rangle$ states coming out of one of the two ports of the first beamsplitter will be separated due to the different polarization of the photons making up the state. These photons will produce coincidences on the SPDs pairs at the outputs of the PBSs. By taking instead coincidences from the outputs of the two different PBSs which are cross-polarized we can retrieve the $|\psi^-\rangle$ states. A further step to extend the efficiency of the BSM to all four Bell states requires the use of non-linear optics in the setup [30].

All the calculations we carried out for the behavior of Bell states entering a beamsplitter took into account photons whose wavepacket is identical in terms of central wavelength and dispersion. Another way to say it is that the photons are indistinguishable. When photons start to differ from one another, for example if their arrival time is not perfectly matched, or their wavelength and spatial overlap is slightly out of tune, the precision of the BSM is reduced. A numerical treatment of the magnitude of the effect of the degree of indistinguishability on the BSM will be given in Section 3.1.

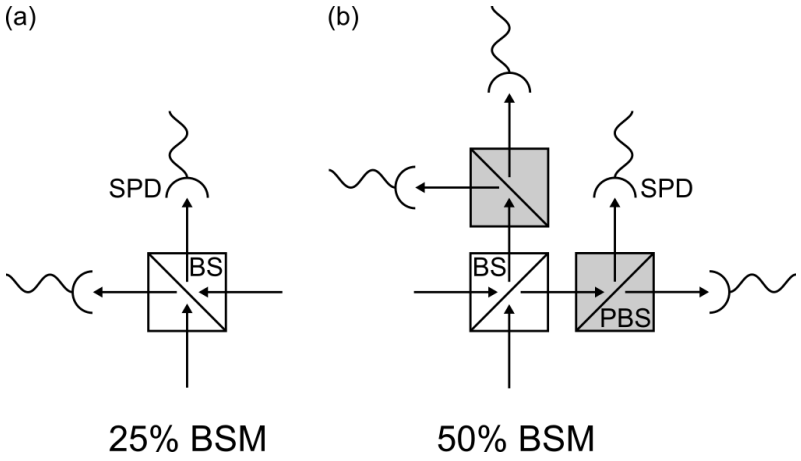

Figure 1.5. (a) Sketch of a 25% efficiency Bell state measurement setup (only the $|\psi^-\rangle$ state is detected) consisting in a single 50:50 beamsplitter (BS) and two single-photon detectors (SPD). (b) Sketch a the Bell state measurement setup with a 50% efficiency (both $|\psi^-\rangle$ and $|\psi^+\rangle$ states are detected), obtained by adding two polarizing beamsplitters (PBS) and two more SPD.

1.3 Semiconductor quantum dots: a source of entangled photons

In the previous Section we sketched the operation of a quantum repeater with its two basic protocols, i.e., state and entanglement teleportation. We also presented in more details one of the two cores of the protocols, the BSM device. It is now time to shift our attention to the other core of the protocols: the source of the entangled photons.

Currently, spontaneous parametric down-conversion (SPDC) crystals are considered the entangled-light workhorses, delivering pairs of entangled photons with high count rates, degree of entanglement and indistinguishability and working at room temperature [23, 31, 32]. They in turn have a major intrinsic limitation: in order to have a higher flux of photons, one must increase the laser power that triggers the down-conversion and the spurious multiple photon events increases, ruining the single-photon purity.

The limitations of current sources have led to intensive efforts on the study and fabrication of solid-state based quantum emitters [33]. Among the others, semiconductor quantum dots (QDs) are arguably one of the most attractive [34]. They can generate pairs of entangled photons [35, 36], deterministically [37], with record-low multiphoton emission [38], high efficiency [39, 40], high indistinguishability [39–41], high degree of entanglement [42], also in response to electrical triggers [43–45]. Moreover, their emission properties can be easily tuned via external perturbations [36, 46] and the generated photons can be interfaced with other QDs [47, 48] or

other quantum systems [49]. Yet, the exploitation of entangled photons from QDs in quantum teleportation protocols has been extremely limited so far, with only a few experiments on state teleportation [50–52] and only two very recent reports on entanglement teleportation [53, 54].

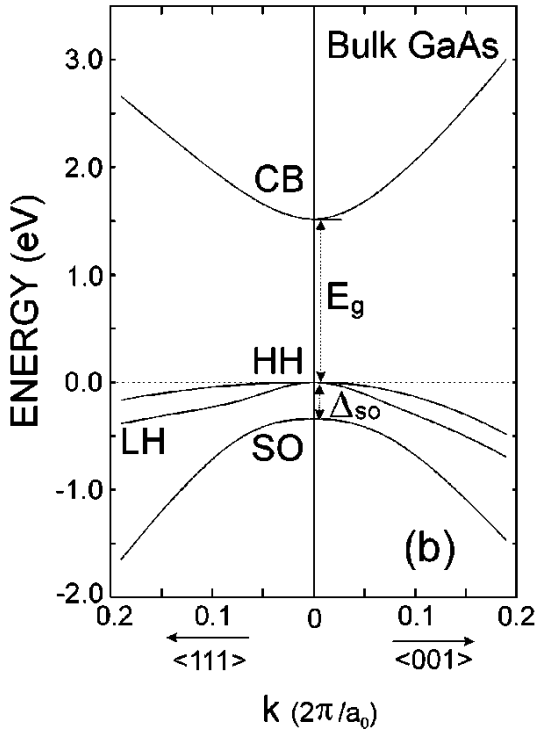

Figure 1.6. Diagram of the band structure in the vicinity of the energy gap (E_g) of bulk GaAs. The valence band is distinguished in the heavy hole (HH) and light hole (LH) bands. From Ref. [55].

To model the opto-electronical properties of a semiconductor QD we need to start from its basic constituent, i.e., a semiconductor material. A semiconductor is any crystal with the Fermi energy laying in an energy gap (E_g) in the electronic dispersion band, whose optical and electronic properties can be changed at will by the controlled insertion of impurities in the lattice. A semiconductor material without a noticeable amount of dopants is called intrinsic and has the Fermi level in the middle of the bandgap. At 0 K all the electrons in a semiconductor fill all the available states in the valence band (VB). By giving an electron an energy larger than the E_g of the material, for example with the use of electric fields, or by shining light with a frequency ν such that $h\nu \geq E_g$, we could remove it from the VB and promote it in the next available band, called conduction band (CB).

An important discrimination among semiconductor materials is between direct and indirect bandgap materials. If the minimum of the CB is at a different crystal

momentum k with respect to the maximum of the VB, the promotion or demotion of an electron among these bands needs a non-negligible k contribution from another excitation, usually a phonon. If the minimum of the CB in the k-space is directly above the maximum of the VB then the promotion (demotion) of an electron can be performed with just the absorption (emission) of a single quantum of light, which, at the energies comparable to the E_g of semiconductors, has a negligible k vector with respect to the orders of magnitudes of k of electrons in a crystal. Direct bandgap semiconductors are widely used for absorption and emission of light in light emitting diodes, lasers and sensors. Among the direct-bandgap semiconductors place of interest for optoelectronics and in this thesis is occupied by Gallium Arsenide (GaAs), see its band structure in Fig. 1.6.

After an electron is promoted from the VB to the CB, it leaves an empty space in the VB. The collective excitation of the whole VB minus one electron is called hole (h) and it behaves as a positively charged particle with a mass which is proportional to the inverse of the curvature of the band in that k. After excitation, the electron and the hole will relax toward the minimum of the CB and the maximum of the VB respectively, through electron-electron interaction and fast scattering with phonons (order of tens of picoseconds), and will live in the crystal, before annihilation by either emitting a photon (luminescence) or through non-radiative alternative channels, for a time which could range between nanoseconds and hundreds of picoseconds depending on the efficiency of the recombination process. If the excitation of an electron from VB to CB is triggered by the absorption of light the phenomenon takes the name of photoluminescence (PL).

1.3.1 Electron in a box

If we reduce the physical dimensions of a semiconductor in all three directions down to the de Broglie length of the electron in the material, the electronic structure and, consequently, the emission of light from the material changes dramatically. Such a system is called semiconductor QD. The situation experienced by electrons and holes in a QD is similar to that of a particle in a box. If we look at the simple 1D model of a quantum particle of mass m forced on a segment of length L by an infinite potential well $V(x)$, the solutions of the Schrödinger equation

$$-\frac{\hbar^2}{2m}\frac{d^2\psi}{dx^2} + V(x)\psi(x) = E\psi(x) \tag{1.17}$$

are stationary waves that vanish outside the segment, with nodes in the boundaries

$$\phi_n(x) = \sqrt{\frac{2}{L}}\sin\frac{n\pi x}{L} \tag{1.18}$$

and energy eigenvalues:

$$E_n = \frac{\hbar^2 \pi^2 n^2}{2mL^2} \tag{1.19}$$

where $n = 1, 2, 3...$ labels the different solutions at increasing energy.

The extension to a 3D box is straightforward if we decompose the potential $V(x, y, z)$ into a sum of potentials which depend on one coordinate only $V(x, y, z) = V_x(x) + V_y(y) + V_z(z)$, the problem is then separable into three 1D problems and the solution reads as:

$$\psi(x, y, z) = 2\sqrt{\frac{2}{L_x L_y L_z}} \sin\frac{\pi n_x x}{L_x} \sin\frac{\pi n_y y}{L_y} \sin\frac{\pi n_z z}{L_z} \tag{1.20}$$

where $n_x, n_y, n_z = 1, 2, 3...$ are the three independent quantum numbers describing the state. The energy eigenvalues are:

$$E(n_x, n_y, n_z) = \frac{\hbar^2 \pi^2}{2m} \left[\left(\frac{n_x}{L_x}\right)^2 + \left(\frac{n_y}{L_y}\right)^2 + \left(\frac{n_z}{L_z}\right)^2 \right] \tag{1.21}$$

From Eq. 1.21 we can derive some qualitative indications of the situation experienced

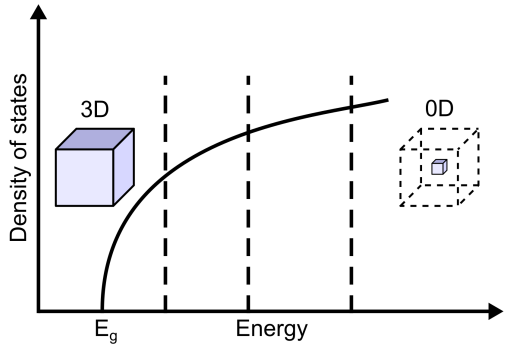

Figure 1.7. Sketch of the density of states versus energy for a bulk material (solid line) and a 0-dimensional quantum dot (dashed lines).

by an electron in a quantum box. The energy of the electron is not a continuum anymore but it is discretized according to the three quantum numbers n_x, n_y, n_z. This fact is reflected in the density of states which changes from a continuous curve to a series of Dirac's delta, corresponding to the different available states, see Fig. 1.7. The ground state energy of the electron $E_0 = E(1, 1, 1)$ is bigger than zero and is dominated by the shortest side length. This means that electrons will be found at energies that are higher than the E_g of the material. The energy distance between the ground state and the first excited state is instead determined by the largest side

length. These considerations are true for the simplistic model we have described but holds with a good approximation in other models.

1.3.2 Effective-mass approximation

To obtain the exact solution of the single-particle problem of electron and holes in a semiconductor QD we would need to add the three-dimensional potential well to the periodic Hamiltonian of the crystal. Even a numerical solution to this problem would be a formidable task, so we need to make some drastic approximations in what is called the effective-mass approximation [56]. Following the calculations in Ref. [57] we first start by adding a perturbation (for example an impurity in the crystal) to the Hamiltonian of the crystal:

$$\left[\mathcal{H}_{crys} + V_{imp}(\mathbf{R})\right]\psi(\mathbf{R}) = E\psi(\mathbf{R}) \tag{1.22}$$

We then expand the wavefunction of the electrons in terms of the Bloch wavefunctions of the bulk crystal $\phi_{nk}(\mathbf{R}) = u_n(\mathbf{k})e^{i\mathbf{kR}}$:

$$\psi(\mathbf{R}) = \sum_n \int_{-\pi/a}^{\pi/a} \tilde{\chi}(\mathbf{k})\phi_{nk}(\mathbf{R})\frac{dk}{2\pi} \tag{1.23}$$

and then assume that only one band has a significant role, dropping the summation over n.

We then restrict our calculations only to transitions in a small region of the k-space, at the bottom of the CB, which is in the Γ point ($k = 0$) for GaAs. Under these approximations, the electron wavefunction can be rewritten as a product of the crystal wavefunction modulated by an envelope function $\chi(\mathbf{R})$ slowly varying with respect to the crystal lattice constant:

$$\psi(\mathbf{R}) = \phi_{n0}(\mathbf{R})\chi(\mathbf{R}) \tag{1.24}$$

The problem can be reduced to solving the pseudo-Schrödinger equation for the envelope function:

$$\left[\varepsilon_n(-i\nabla) + V_{imp}(\mathbf{R})\right]\chi(\mathbf{R}) = E\chi(\mathbf{R}) \tag{1.25}$$

Where $\varepsilon_n(\mathbf{k})$ is the dispersion curve for the n-band which can be simplified under the assumption of considering only wavefunctions from a small region of the k-space. At the bottom of the CB we can approximate the energy dispersion as parabolic:

$$\varepsilon_n(\mathbf{k}) \approx E_c + \frac{\hbar^2 k^2}{2m_0 m_e} \tag{1.26}$$

where E_c is the energy of the bottom of the conduction band and m_e is the effective mass of electrons. If we substitute this expression back into Eq. 1.25, replacing $\mathbf{k} \rightarrow -i\nabla$, we get a Schrödinger equation similar to that of free electrons with an effective mass and energy measured from the bottom of the CB:

$$\left[-\frac{\hbar^2}{2m_0 m_e}\nabla^2 + V_{imp}(\mathbf{R})\right]\chi(\mathbf{R}) = (E - E_c)\chi(\mathbf{R}) \tag{1.27}$$

We can use Eq. 1.27 in the case of an etherojunction between to different materials using the offset in the energy bands as the potential V_{imp}. Indeed, a way to fabricate a QD is by enclosing a semiconductor material with dimensions in the orders of the nanometer inside another one with a higher bandgap and by choosing the materials so that we have a band alignment of type I, i.e., the smaller bandgap material CB and VB are respectively lower and higher than the CB and VB of the larger bandgap material, see the hybrid diagram in Fig. 1.8 where the CB minimum and VB maximum are plotted against the three physical dimensions. In this situation, the potential well is represented by the energy mismatch between the CB minimum and VB maximum at the boundary of the two materials. In a heterostructure, effective masses and Bloch functions are in principle different between materials and we need to check that the approximations we introduced are still valid. The different effective masses, for example, produces a discontinuity in the derivative of the envelope function and the effective-mass approximation is still valid under the assumption that the envelope function varies slowly on the atomic scale. Under these approximations electron and holes in a QD can be then modeled as free particles with effective masses depending on the curvature of bands at the Γ point, enclosed in a potential well of the same magnitude of the CB and VB offsets respectively.

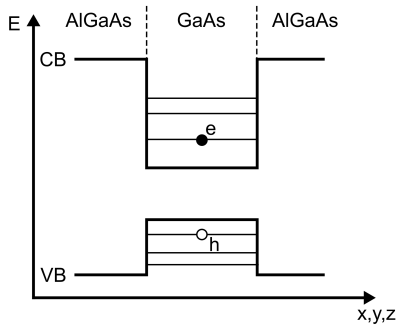

Figure 1.8. Hybrid energy diagram of the bandgap energy in a QD with type I band alignment. On the horizontal axis is represented one of the physical dimensions of the QD and on the y axis is plotted the energy. The flat bands reflects the effective-mass approximation around the CB minimum and VB maximum.

We can also give an estimation of the boundary in the dimensions of a semi-

conductor below which we can consider it a QD. We will start to see confinement effects as soon as the dimensions of the box approach the typical wavelength of electrons in a semiconductors (around 24 nm at 300 K in GaAs), but in order to have a particle remaining in the ground state, its thermal energy must not be bigger than the difference between the ground state and the first excited state in all three dimensions, implying that $L < \frac{\pi\hbar}{\sqrt{2mk_BT}}$.

1.3.3 Excitonic complexes

When we take into account also the Coulomb interaction between electrons and holes, the Hamiltonian needs to be corrected with the term:

$$W(\mathbf{r}_e, \mathbf{r}_h) = -\frac{1}{4\pi\varepsilon_0\varepsilon_r}\frac{e^2}{|\mathbf{r}_e - \mathbf{r}_h|} \tag{1.28}$$

The Schrödinger equation for electrons and holes is similar the problem of the hydrogen atom and we can resort to the same solution methods. In particular we can see that the attractive Coulomb interaction between an electron and a hole results in the formation of a bound state called exciton (X), with a binding energy which we can calculate as in a hydrogen-like atom with the effective masses of the two particles and the relative dielectric constant of the semiconductor:

$$E_X(n) = -\frac{\mu}{m_0}\frac{1}{\varepsilon_r^2}\frac{R_H}{n^2} \tag{1.29}$$

where μ is the reduced mass of the system and R_H is the Rydberg constant. For GaAs, the binding energy of the first state is approximately 4.2 meV resulting in a radius of the X of 13 nm, which is large compared to the lattice constant of 0.5 nm, justifying the effective-mass approximation.

Due to the resemblance with an atomic system, an X with both the electron and the hole in the ground state will be said to be in the *s*-shell. Excited states, usually reached at high excitation power or higher temperatures, are named after the higher atomic orbitals *p*-shell, *d*-shell, etc.

In a QD at low temperature, because of quantum confinement, no free electron-hole pairs can exist and the fundamental excitation is the neutral X. For the purpose of our study we will concentrate only on the *s*-shell. Due to the Pauli exclusion principle, only two electron/hole pairs, with discording spin directions, can occupy the same level. We can combine all the possibilities of partial filling and spin-configurations.

The confinement (and, possibly, strain) in a QD lifts the degeneracy between light holes with projection of the total angular momentum $J_z^{lh} = \pm\frac{1}{2}$ and heavy holes

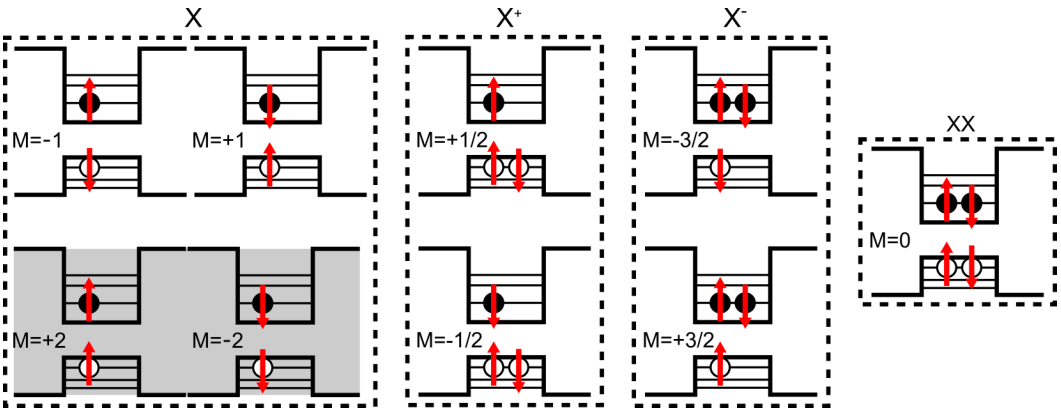

Figure 1.9. Electron (filled circle) and hole (blank circle) spins configurations for the *s*-shell of a quantum dot. The projection of the total angular momentum M is given for every configuration. The exciton (X) states has four configurations that are distinguished between "bright" states (top part, with white background) which can decay emitting a single-photon and "dark" (bottom part, with gray background) states which cannot decay emitting a single photon. The two trion states (X^+ and X^-) have two configurations each. The biexciton state (XX) represents the complete shell and has a single configuration.

($J_z^{hh} = \pm\frac{3}{2}$) so that the maximum of the VB is usually only composed of heavy-hole states with no mixing of the two bands. The combination of the heavy-holes and electrons ($S^e = \frac{1}{2}$) spin configurations can be subdivided according to the projection of the total angular momentum $M = S_z^e + J_z^h$ along the growth direction labeled as z axis, which in typical epitaxial QD is the main confinement direction. For the neutral X we have 4 states in the basis of M, see Fig. 1.9. The two states with $|M| = 2$ cannot decay to the ground state with the emission of a single photon and are then called "dark" states. The remaining two, with anti-parallel spin projection configuration and $|M| = 1$ can emit a photon when decaying to the ground state and are known as "bright" states,. An odd particle number state is known as a trion or charged exciton (X^+ with $|M| = 1/2$ and X^- with $|M| = 3/2$). When the whole *s*-shell is complete, two electron-hole pairs are present and we have a single configuration, called biexciton (XX), with $|M| = 0$, see right panel of Fig. 1.9.

The Coulomb interaction between electrons and holes in a QD is enhanced due to the close proximity of the charges and it competes with the confinement energy in the ordering of the different excitonic species [58, 59]. To reconstruct the different energies of the excitonic complexes we first restrict our calculations to only direct Coulomb interaction between first excited states:

$$W_{ij} = \iint \frac{q_i q_j}{4\pi\varepsilon_r\varepsilon_0} \frac{|\psi_i(\mathbf{r}_i)|^2 |\psi_j(\mathbf{r}_j)|^2}{|\mathbf{r}_i - \mathbf{r}_j|} d\mathbf{r}_i d\mathbf{r}_j \tag{1.30}$$

where i and j are indexes for either electron (e) and hole (h). The magnitude and sign of the different terms depends on the particle types (being repulsive for the same

particle type so that $W_{ee}, W_{hh} > 0$ or attractive in the case of different particles so that $W_{eh} < 0$), on the spatial extent of the single particles wavefunctions, and on their relative positions inside the QD. If the electron and holes wavefunction share the same barycenter and the electron wavefunction is larger than the hole wavefunction (due to its lower effective mass) the magnitudes of the Coulomb terms is such that $W_{ee} < |W_{eh}| < W_{hh}$.

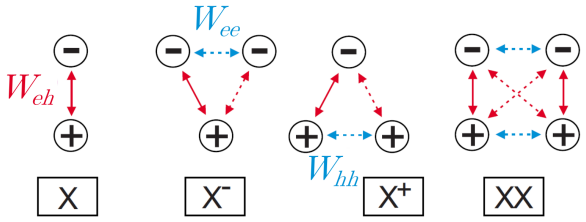

Figure 1.10. Picture of the direct Coulomb interactions between electrons and holes in the four excitonic complexes in the *s*-shell of a QD. Adapted from Ref. [58].

Following the scheme in Fig.1.10, the energies of the four species will be:

$$\begin{aligned} E(\mathrm{X}) &= [\varepsilon(e) - \varepsilon(h)] + W_{eh} \\ E(\mathrm{XX}) &= [2\varepsilon(e) - 2\varepsilon(h)] + 4W_{eh} + W_{ee} + W_{hh} \\ E(\mathrm{X}^-) &= [2\varepsilon(e) - \varepsilon(h)] + 2W_{eh} + W_{ee} \\ E(\mathrm{X}^+) &= [\varepsilon(e) - 2\varepsilon(h)] + 2W_{eh} + W_{hh} \end{aligned} \tag{1.31}$$

where $\varepsilon(i)$ represents the energy of a single particle.

In a spectroscopic experiment we only access transition energies corresponding to the emission of photons from the recombination of single electron-hole pairs. We then need to compute the energy differences between the starting and ending state in the luminescence process:

$$\begin{aligned} \hbar\omega_{\mathrm{X}}(\mathrm{X} \to 0) &= E(X) \\ \hbar\omega_{\mathrm{XX}}(\mathrm{XX} \to \mathrm{X}) &= E(\mathrm{XX}) - E(\mathrm{X}) \\ \hbar\omega_{\mathrm{X}^-}(\mathrm{X}^- \to e) &= E(\mathrm{X}^-) - \varepsilon(e) \\ \hbar\omega_{\mathrm{X}^+}(\mathrm{X}^+ \to h) &= E(\mathrm{X}^+) - \varepsilon(h) \end{aligned} \tag{1.32}$$

The binding energies, i.e., the energy difference from the neutral X state, are then:

$$\begin{aligned} \Delta_{bind}(\mathrm{XX}) &= \hbar\omega_{\mathrm{X}} - \hbar\omega_{\mathrm{XX}} = -2W_{eh} - W_{ee} - W_{hh} \\ \Delta_{bind}(\mathrm{X}^-) &= -W_{eh} - W_{hh} \\ \Delta_{bind}(\mathrm{X}^+) &= -W_{eh} - W_{ee} \end{aligned} \tag{1.33}$$

These binding energies would lead to a transition ordering from lower to higher energy: X^-, X, XX, X^+, see Fig. 1.11(b).

When accounting also for the correlations among electrons and holes wavefunctions and their spins a binding XX may appear, see Fig. 1.11(c). The ordering and magnitude of the effects strongly depends on the geometrical structure and chemical composition of the QD, in a way such that it is even possible to have different orderings between QDs in the same sample [60].

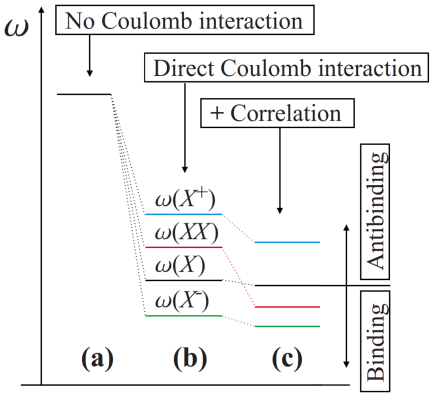

Figure 1.11. Evolution of the excitonic transition energies. (a) When no Coulomb interaction is taken into account all the transitions are degenerate. (b) Direct Coulomb interaction lifts the degeneracy on the transition energies and an energy ordering is expected. For InGaAs QDs with electrons and holes sharing the same barycenter and a larger electron wavefunction we expect a binding X^- and anti-binding XX and X^+. (c) When taking into account correlation terms, a binding XX can be observed. Adapted from Ref [58].

The different possible decay paths from the excitations of the *s*-shell are beautifully depicted in the PL spectrum of a single InGaAs QD in Fig. 1.12. Here, electrons are excited using photons with an energy above the bandgap of the barrier semiconductor. The generated electron-hole pairs are trapped in the QD and there thermalize to the lowest available energy levels before recombining with the emission of a photon.

The GaAs QDs used in this work are larger in size with respect to the InGaAs QDs we have shown before. This in turns means that the electrons and holes will experience a smaller confinement. The situation regarding the ordering and the number of the transition energies is much more complicated and PL spectra from these QDs will feature several lines. In this case, an atomistic many-body theory can be used to simulate the emission spectra of such QDs [59]. Figure 1.13 shows the results of the calculations for a lens-shaped GaAs/AlGaAs QD with a base diameter of 40 nm and a height of 2 nm. The main features of the GaAs QDs used in these work are very well reproduced, with an isolated X line and all the other transitions

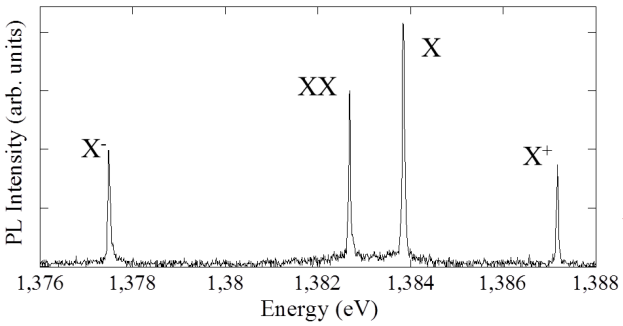

Figure 1.12. Photoluminescence spectrum of a single InGaAs QD with a 10 nm to 20 nm diameter and a 2 nm to 5 nm height, with labeled transitions. Courtesy of Prof. R. Trotta.

at lower energies, see for example the PL spectra of QDs in Section 4.3.

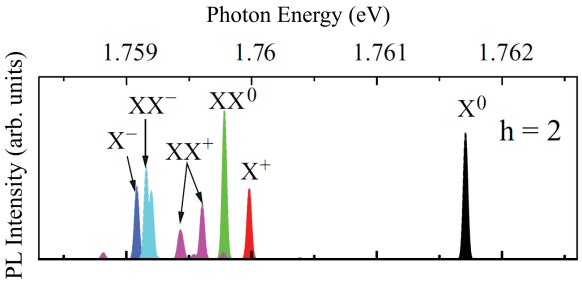

Figure 1.13. Atomistic many-body calculation of the excitonic complexes emission lines in a lens-shaped GaAs/AlGaAs QD with a base diameter of 40 nm and a height of 2 nm. Adapted from Ref. [59].

1.3.4 Entangled-photon emission

The emission of an entangled photon pair from a QD is achievable from the two-photon radiative cascade from the XX state. One of the two electron-hole pairs of the XX recombines via the emission of a photon, leaving the QD with a single X in it. In an ideal QD the two bright states ($|M| = 1$) of the X are degenerate in energy. This implies that the first photon, whose energy is equal to the difference between the XX state and X state, will be emitted with either right (R) or left (L) circular polarization depending on which of the two X states is reached after the emission, see Fig. 1.14. A second photon is then emitted after the recombination of the remaining X in the QD, with an energy corresponding to the X state energy and orthogonal circular polarization with respect to the previously emitted XX photon. If the X state is truly degenerate, i.e., the energy difference between the two exciton state, commonly known as fine structure splitting (FSS), is much smaller then the homogeneous linewidth of the photons, the two-photons cascade generates

the entangled state $\frac{1}{\sqrt{2}}(|R\rangle_X |L\rangle_{XX} + |L\rangle_X |R\rangle_{XX})$, which corresponds to the $|\phi^+\rangle$ state.

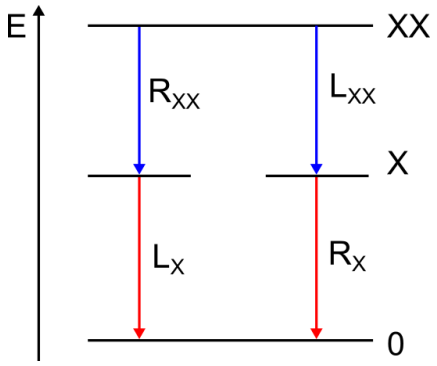

Figure 1.14. The two-photon cascade from the XX state in a QD. The two radiative decay paths toward the ground state pass through the degenerate X state emitting two photons with orthogonal polarization configurations. If the degeneracy is not lifted the two paths are indistinguishable and the emitted photon pair will be entangled in polarization.

Entanglement fidelity

To evaluate the degree of entanglement of a pair of photons, we have to first reconstruct the two-photon density matrix by performing a set of (at least) 16 projective measurements on several identical copies of the state [61] and then extract the parameters quantifying the level of entanglement of the state (such as the concurrence). However, if the polarization properties of the setup are known, and we make sure that the emission from the QD is not polarized, it is easier to calculate the degree of entanglement via a measure of the overlap of the measured state to the expected Bell state. The result of the projection is known in literature as fidelity, *f*. This parameter which is 1 (0.5) for perfect entangled (classically correlated) states, can be evaluated with a reduced set of 6 co- and cross-polarized coincidence measurements between the two photons of the pair, in the three polarization bases corresponding to equally spaced points in the Poincaré sphere, namely linear *HV*, diagonal *DA*, and circular *RL*.

For each polarization basis, we can calculate the cross-correlation visibilities between the X and XX photons with the formula:

$$C_{ij} = \frac{g_{ii}^{\mathrm{X,XX}}(0) - g_{ij}^{\mathrm{X,XX}}(0)}{g_{ii}^{\mathrm{X,XX}}(0) + g_{ij}^{\mathrm{X,XX}}(0)} \tag{1.34}$$

where i and j represents the two orthogonal polarizations of a basis, and then the

fidelity to the $|\phi^+\rangle$ state with the formula [62]:

$$f^{|\phi^+\rangle} = \frac{1 + C_{HV} + C_{DA} - C_{RL}}{4} \tag{1.35}$$

In a semiconductor QD, there are several effects that may lead to a degradation of the degree of entanglement of the emitted photons: The most prominent is the presence of a FSS between the two intermediate X states with a magnitude comparable with the X state linewidth combined with the finite time resolution of the experimental setup.

Fine structure splitting

In Section 1.3.3 we have mentioned that the bright exciton state is doubly degenerate. If we consider only the direct Coulomb term, we see that all the four exciton states, dark and bright, share the same energy level. The degeneracy of the bright states is fundamental for the generation of entangled photons during the two-photon cascade from the XX state to the ground state. The Coulomb exchange interaction couples the spins of the electron and the hole of the X, and introduces an energy difference between the X states, if the symmetry of the QD is lowered. The Hamiltonian of the electron-hole exchange interaction, calculated from symmetry arguments, reads as:

$$\mathcal{H}_{exc} = -\sum_{i=x,y,z} \left(a_i J_{h,i} S_{e,i} + b_i J^3_{h,i} S_{e,i} \right) \tag{1.36}$$

where a and b are spin-spin coupling constants. In a QD with D_{2d} symmetry the two states are degenerate. If we lower the rotation symmetry of the QD in the plane (C_{2v} group) by a uniaxial deformation, e.g., by strain, so that the shape of the dot becomes ellipsoidal, the projection along the growth axis of the angular momentum is no longer a good quantum number and the two eigenstates of $\mathcal{H}_{exc}$ are symmetric and antisymmetric linear combinations of $|\pm 1\rangle$ states. The degeneracy between the two bright X states is removed and the two states $|B_\pm\rangle = |1\rangle \pm |-1\rangle$, parallel to the [110] and [1$\bar{1}$0] crystal directions, are split by the FSS. In real QDs with no symmetry, i.e. belonging to the C_1 group, there is an additional mixing of the $|B_\pm\rangle$ states which introduces an angle in the polarization of the exciton emission, $\theta_\pm$, with respect to the crystal directions [110] and [1$\bar{1}$0] [63].

The XX state instead, being a non-degenerate spin singlet, is unaffected by spin exchange interactions. A finite FSS will then produce only two distinguishable paths in the cascade from the XX state to the X state and then to the ground state. The two paths can be distinguished with a polarization resolved measurement even if the

FSS is smaller than the spectral resolution of the setup by observing the mutual oscillation of X and XX transitions while changing the angle of half-waveplate before a polarizer in front of a spectrometer, see Fig 1.15.

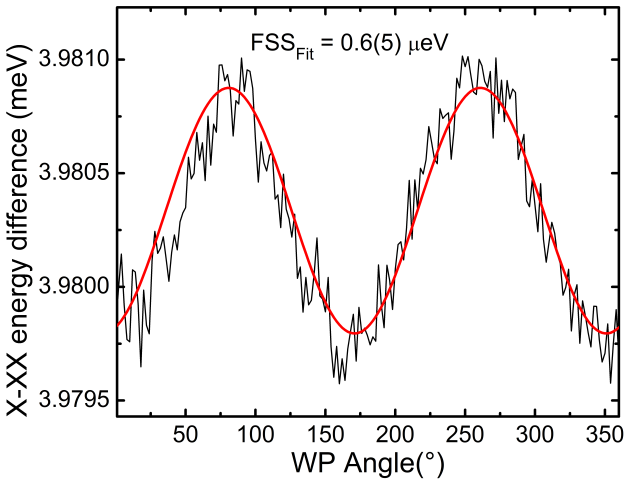

Figure 1.15. Oscillation of the energy difference between the XX and X states in the resonant excitation spectrum of a single GaAs QD. The oscillation is produced by rotating a lambda-half waveplate in front of a linear polarizer placed before the spectrometer. The splitting of the X state is equal to half the amplitude obtained with a $\cos^2(\theta)$ fit (red curve).

In the presence of a FSS, the entangled XX-X photon polarization state turns into

$$|\phi\rangle_t = \frac{1}{\sqrt{2}}\left(|H\rangle_{XX}|H\rangle_X + e^{\frac{iSt}{\hbar}}|V\rangle_{XX}|V\rangle_X\right) \tag{1.37}$$

where S is the magnitude of the FSS and t is the (randomly distributed) time span between the XX and X photon emission. The average fidelity to $|\phi^+\rangle$ state can be strongly reduced from unity when $S \gtrsim \hbar/\tau_X$, where τ_X is the radiative lifetime of the X state which determines the probability distribution of t. With post-selection and good time-resolution detectors, the state can be projected again on a completely entangled state. While there are other decoherence mechanisms (such as re-excitation and multiphoton emission, and exciton spin-scattering processes due to excess charges in the QD surrounding), recent results have demonstrated that in GaAs QDs with suppressed FSS [42, 62, 64] an entanglement fidelity as high as 0.98 can be achieved without temporal and spectral post-selection, thus suggesting that QDs can be regarded as dephasing-free sources of entangled photons [65]. The suppression of FSS via the application of strain fields will be discussed in greater details in the next Section. As we will see in Section 3.1, the slight difference in energy between the two states will also affect the outcome of the BSM by making

the two X photons more distinguishable.

1.4 Strain tuning of quantum dots

Self-assembled QDs features strikingly good emission properties but suffer from the statistical nature of the growth process. The mean wavelength of a single sample can be tuned by changing the growth conditions but every single QD on a sample will be almost unique in terms of emission energy and FSS. If on the one hand this means that, starting from a sample with low mean FSS, it is possible (but not easy) to find a single QD with an extremely low FSS ($< 1\,\mu eV$), on the other hand finding a second QD with same low FSS and same emission energy, so as to implement quantum communication protocols with distinct QDs, is an impossible task. To transfer this in numbers, theoretical calculations showed that a very low portion ($\sim 10^{-3}$) of as-grown QDs feature a FSS low enough to retain a high entanglement fidelity [66] event though the situation gets better when dealing with highly symmetrical QDs samples. The typical distribution broadening of the QDs emission in the same sample is 10 meV, while radiative linewidth is $\sim$1 µeV. The combined probability to interface two cherry-picked QDs with low FSS and equal emission energy at the same time is of the order of $\sim 10^{-9}$. For this reason, all the demonstrations of quantum communication protocols were performed with the same "hero" QD acting as the two sources of entangled pairs needed [52–54]. Moreover, in a realistic scenario, we would also expect that to build up a QD-based quantum network one would need to interface QDs with other quantum systems, such as quantum memories, thus posing additional constraints on the QD emission properties. This implies that it is impossible to use as-grown self-assembled QDs for quantum communication and the need of post-growth fine-tuning is mandatory.

The emission properties of QDs can be tuned with the application of either electric [67–69], magnetic [70], or strain fields [49], or in a combination of them [46]. To get tunable sources of maximally entangled photon pairs we would need to achieve the tunability of the QD emission while keeping the FSS at zero. As we will see in the next Section, this task can be performed with the use of a three-axial stress application [49].

1.4.1 Three-axial stress application

The method proposed by Trotta *et al.* to erase FSS and tune the emission of any QD of a sample is based on the application of an in-plane three-axial stress to reshape the electronic structure of QDs [64]. The application of controlled stress on the sample can be achieved by exploiting the conversion of an electric field into

volume deformation in some materials via a phenomenon known as piezoelectricity. By bonding the QD sample onto a piezoelectric material we can control the amount of stress induced in QDs by applying a tunable DC voltage on the two faces of the piezoelectric slab. The resulting strain contribution enters in the Hamiltonian and can be engineered in such a way that the degeneracy between the two bright X states can be reestablished, in principle, on any starting QD, provided that the magnitude of the produced strain is large enough.

As mentioned in the previous Section a real, asymmetric QD belongs the C_1 symmetry group. We can write its exchange Hamiltonian in the basis of the $|B_\pm\rangle$ states as:

$$\mathcal{H}_{exc} = \begin{pmatrix} E_0 + \eta & k \\ k & E_0 - \eta \end{pmatrix} \tag{1.38}$$

where E_0 is the energy of the degenerate X state in a D_{2d} QD and η and k are coefficients that account for the lowering of the symmetry down to C_1. The solution of the Hamiltonian in Eq. 1.38 leads to two states with energy $E_\pm = E_0 \pm \sqrt{\eta^2 + k^2}$. The two eigenstates can be written as combinations of the $|B_\pm\rangle$ states as $|\Psi_\pm\rangle = k\,|B_+\rangle + (-\eta \pm \sqrt{\eta^2 + k^2})\,|B_-\rangle$ forming angles with respect to the crystal axes $\tan\theta_\pm = (-\eta \pm \sqrt{\eta^2 + k^2})/k$. Because of the Wigner-von Neumann non-crossing rule, a single external field cannot remove the FSS and to circumvent this problem we would need the application of two independent fields.

In-plane stress fields offer three independent degrees of freedom in the form of the three different components of the stress tensor $\sigma_{xx}, \sigma_{xy}, \sigma_{yy}$, which can be equivalently viewed as two principal stresses S_1 and S_2, and the angle ϕ of application with respect to the crystal [110] axis. The Hamiltonian associated to strain is:

$$\delta\mathcal{H}_{strain} = \begin{pmatrix} \overline{\alpha}\ \overline{p} + \alpha\Delta p\cos 2\phi & \gamma\Delta p\sin 2\phi \\ \gamma\Delta p\sin 2\phi & \overline{\alpha}\ \overline{p} - \alpha\Delta p\cos 2\phi \end{pmatrix} \tag{1.39}$$

where $\overline{\alpha}$, α, and γ are parameters related to the elastic constants renormalized by the deformation potentials, $\overline{p} = S_1 + S_2$ is the hydrostatic part of the stress, and $\Delta p = S_1 - S_2$ is the stress anisotropy. As we we will see, only three parameters are relevant: $\overline{p}$, Δp, and ϕ. The X level degeneracy can be restored by setting the angle of the applied stress ϕ so that the resulting strain angle ϕ_ϵ is roughly parallel to the anisotrpy angle θ^+ and then by adjusting Δp accordingly (we remind that ϕ and ϕ_ϵ are related via the elastic compliance constants S_{ij} with $\tan 2\phi = \frac{S_{44}}{2(S_{11}-S_{12})}\tan 2\phi_\epsilon$). The level degeneracy requires that the effective Hamiltonian $\mathcal{H}_{eff} = \mathcal{H}_{exch} + \delta\mathcal{H}_{strain}$

in the $|B_{\pm}\rangle$ base features the following properties:

$$\begin{aligned} \langle B_+| \mathcal{H}_{eff} |B_-\rangle &\equiv 0 \\ \langle B_+| \mathcal{H}_{eff} |B_+\rangle &\equiv \langle B_+| \mathcal{H}_{eff} |B_+\rangle \end{aligned} \tag{1.40}$$

In turns, this sets the equations that the stress parameters have to fulfill:

$$\eta = -\alpha \Delta p \cos 2\phi \tag{1.41}$$

$$k = -\gamma \Delta p \sin 2\phi \tag{1.42}$$

The FSS will be suppressed when the stress is applied at an angle ϕ^* such that the resulting strain angle ϕ_ϵ^* follows the relation $\tan 2\phi_\epsilon^* = \frac{2(S_{11}-S_{12})}{S_{44}} \tan 2\theta^+$ where we have used $k/\eta = \gamma/\alpha \tan 2\phi$ and the bisection formula for the tangent so that $\tan 2\theta^+ = k/\eta$.

We have thus confirmed that for the extinction of the FSS we need to control two parameters, namely Δp and ϕ. In order to also have control over the emission wavelength, a third parameter must be added into the equations. Here comes in help the hydrostatic term $\overline{p}$ that contributes as a diagonal term on the $\delta\mathcal{H}_{strain}$, see Eq. 1.39. Its effect is that of changing the X energy without affecting the FSS. If we fix the difference between S_1 and S_2, i.e., Δp, and their application angle ϕ, we can then play with their magnitude $\overline{p} = S_1 + S_2$ and change the X energy while keeping the FSS pinned at zero. For a numerical treatment of this process one can refer to the original paper discussing this method in Ref. [64].

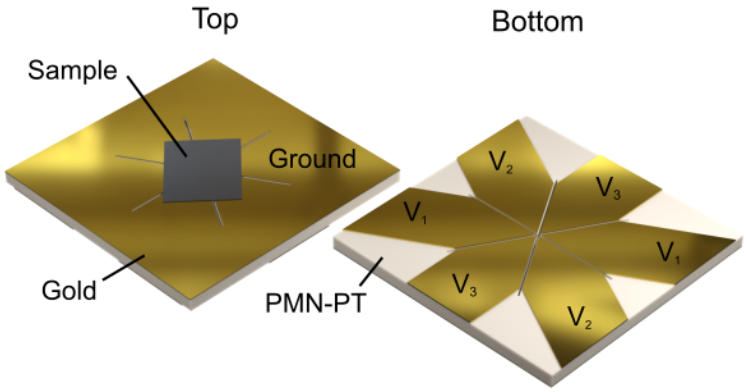

Figure 1.16. Top and bottom view of the six-legged piezoelectric device used to engineer the strain status of a nanomembrane sample containing QDs. The three cuts are obtained with laser ablation on a PMN-PT thin sample with a side of 5 mm. Contacts for ground and for each of the legs are obtained by patterning gold on the surface of the device. The opposing legs are at the same voltage to prevent shifting of the QD under the microscope.

To achieve the three-axial stress tuning, Trotta *et al.* designed a piezoelectric substrate that features three cuts at 60° with respect to each other, see sketch in Fig. 1.16. The three cuts create six separated areas in the piezoelectric, which can be contacted separately and addressed independently with almost no cross-talk. The application of three independent quasi-uniaxial stresses onto the membrane plane is done by applying three independent voltages (V_1, V_2, V_3) on the pairs of facing legs to avoid shifting of the membrane when applying the voltage. The original design to transfer this stress to the QDs contemplates that the as-grown sample is glued onto a piezoelectric $[Pb(Mg_{1/3}Nb_{2/3})O_3]_{0.72}$-$[PbTiO_3]_{0.28}$ (PMN-PT) crystal where electric contacts were previously established.

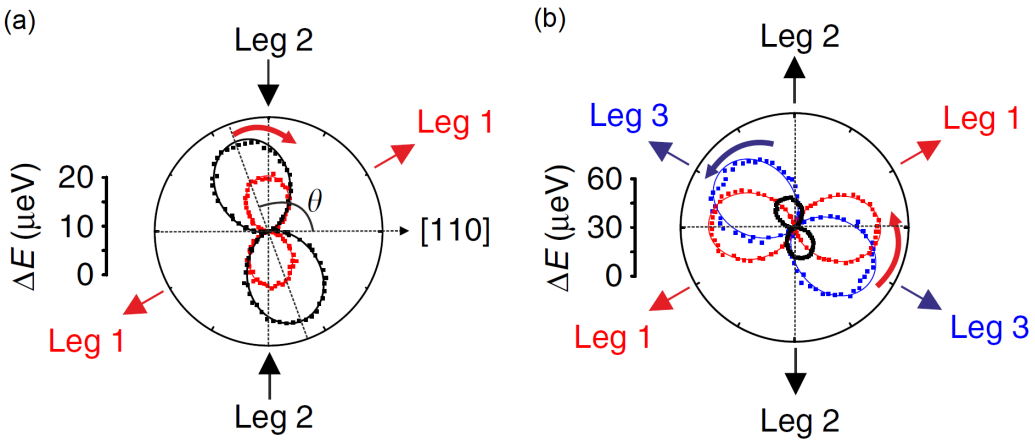

Figure 1.17. (a) Dependence of ΔE as a function of the angle the linear polarization analyzer forms with the [110] crystal axis. The length and orientation of the petals give the value of the FSS s and the angle θ^+, respectively. The black data points correspond to zero applied voltages, while the red data points show the configuration in which Leg 1 is used to achieve $\theta \sim \phi_2$. The solid lines are sinusoidal fits to the experimental data. (b) Same as in (a) when Leg 3 is used to change the QD strain status (see the blue data points) while Leg 1 is again used to achieve $\theta \sim \phi_2$ (see the red data points). The curve for zero applied voltages is also reported for reference (see the black data points). From Ref. [49].

The theory of strain tuning we developed above ensures that one can always find a combination of Δp, ϕ, $\overline{p}$ that erases the FSS in a QD. To transfer this in the practice one can follow the following empirical procedure. First one needs to find the angle θ^+ of orientation of the FSS by a polarization resolved measurement, see black points in the polar plot of Fig. 1.17(a). By applying the voltage to the correct leg, e.g., Leg 1, one orients the FSS angle θ^+ so that it is roughly parallel to the nearest leg of the device, e.g., Leg 2, at ϕ_2, see red polar plot of Fig. 1.17(a). At this point, by changing the V_2 on Leg 2 we can tune the stress status of the QD and erase the FSS. To also change the energy of X transition we make use of voltage applied to Leg 3. By setting a static voltage V_3 to Leg 3 and repeating the FSS rotation and

suppression procedure with Leg 1 and 2, the QD will reach the condition of null FSS at a different energy, see polar plot in Fig. 1.17(b).

Figure 1.18 shows graphically how the FSS magnitude (s) changes when applying voltage to the single legs (every point in a plot corresponds to a different voltage growing or decreasing monotonously from left to right). The orange curve shows that the application of the voltage to a single leg when there is a finite difference between the direction of stress and FSS, leads to an anti-crossing of the two X states so that the FSS has a non-zero minimum. When rotating the direction of FSS θ^+ with another leg (purple curve), the minimum decreases until it reaches below the 1 µeV threshold for the recovery of entanglement (black curves) [41, 62, 70]. When changing the voltage V_3 applied to the third leg of the device and sweeping again V_2 after having realigned θ^+ to ϕ_2 with Leg 1, the minimum of the FSS is reached at different X energy conditions, see the right part of the graph. In the paper which demonstrated the feasibility of this procedure the authors were able to tune the energy of the QD in a range up to 7 meV while keeping the FSS to zero [49].

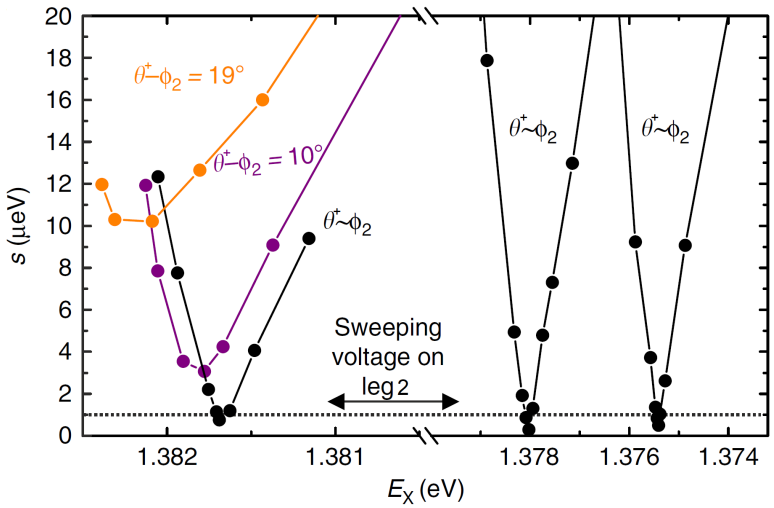

Figure 1.18. Behavior of the FSS as a function of E_X. The voltage on Leg 1 is changed until the angle of FSS is aligned with the direction of Leg 2 (left part of graph, orange, violet, and black curve), when the alignment condition is achieved, a voltage sweep on Leg 2 brings the FSS below the threshold of 1 µeV (dashed line). By changing the voltage on Leg 3 and repeating the procedure the minima of the FSS are achieved for different E_X values (right part of the graph). From Ref. [49].

The restoration of entanglement fidelity was experimentally demonstrated with three-axial stress application by Huber *et al.* in 2018 [36]. In their work they reached values of raw fidelity as high as 0.960(0), which was pushed up to 0.978(5) when accounting for the imperfections in the measurement setup. As this value is below unity, the authors suggested the presence of a residual decoherence mechanisms

probably related to spin-scattering. This can be alleviated using a photonic structures that decrease the lifetime of the transitions via the Purcell effect, while also allowing to tackle the indistinguishability and extraction efficiency issues [39, 40, 71]. This would raise the entanglement fidelity up to values of 0.99 lifting the QDs on the same level of SPDC source [23, 72–74].

Chapter 2

Light emission from single quantum dots

In the previous Chapter we described the theoretical foundations of the entanglement and state teleportation protocols. A teleportation protocol in a real-life application would require the deterministic generation of light signals with an almost null multiphoton emission (to implement error-free and secure quantum key distribution protocols), a high photon flux (as teleportation rates have a steep power dependence on light extraction efficiency), a high degree of indistinguishability (needed to efficiently implement Bell state measurements), and a high degree of entanglement (needed to overcome the classical limit, or, even better, violate Bell inequality, with the teleported photons). We also gave a short introduction of the main characteristics of semiconductor QDs as sources of entangled light. In this Chapter we will describe in more details the figures of merit of our particular choice of QD, i.e., droplet-etched epitaxial GaAs QDs, trying to show why they are promising candidates for the role of entangled-light sources in future quantum networks and focusing on the possible improvements toward the fabrication of an ideal source.

2.1 GaAs semiconductor quantum dots

The quantum light source used in the entanglement teleportation experiments consists of GaAs QDs grown with Al-droplet etching [75]. GaAs QDs grown with this technique exhibit a high in-plane symmetry resulting in a low average FSS ($\sim 4\,\mu$eV) [76]. The samples are grown in the molecular beam epitaxy (MBE) facility of the Institute of Semiconductor and Solid-State Physics of the Johannes Kepler University of Linz (AT). The fabrication of QDs starts with an $Al_{0.4}Ga_{0.6}As$ layer grown on a (001) GaAs commercial wafer. Nanoholes are drilled on the surface of the $Al_{0.4}Ga_{0.6}As$ layer by evaporating Al droplet, see Fig. 2.1(a), followed by an

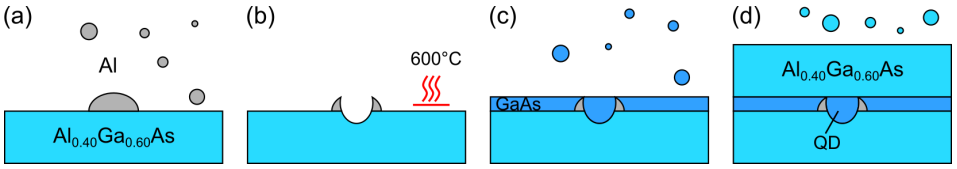

Figure 2.1. Growth steps of GaAs quantum dots with droplet-etch epitaxy. (a) Al droplet are evaporated on the surface of an $Al_{0.4}Ga_{0.6}As$ layer. (b) Nanoholes are drilled on the surface of the $Al_{0.4}Ga_{0.6}As$ layer by evaporating the Al droplet at 600 °C. (c) The nanoholes are filled with a 2 nm thick GaAs layer. (d) The GaAs layer is capped with another $Al_{0.4}Ga_{0.6}As$ layer for a 123 nm total thickness.

annealing step at 600 °C, see Fig. 2.1(b). The nanoholes are then filled with a 2 nm thick GaAs layer, see Fig. 2.1(c), and capped with another $Al_{0.4}Ga_{0.6}As$ layer for a 123 nm total thickness, see Fig. 2.1(d), with QDs laying in the middle of the layer. The resulting QDs have a height of 7 nm to 8 nm and base diameters in the order of 50 nm to 60 nm, resulting in a weak confinement and emissions in the order of 1.56 eV at low temperature [76]. The full active layer is grown between two 60 nm thick $Al_{0.2}Ga_{0.8}As$ layers, which together constitute a λ-cavity. To complete the full planar cavity, two sets of distributed Bragg reflectors (DBRs) are grown, constituted respectively by 9 and 2 pairs of $Al_{0.95}Ga_{0.05}As$ (70 nm) and $Al_{0.2}Ga_{0.8}As$ (60 nm) layers, see Fig. 2.2. The cavity, in combination with a SIL, increases significantly the extraction efficiency up to values of $\sim 12\%$.

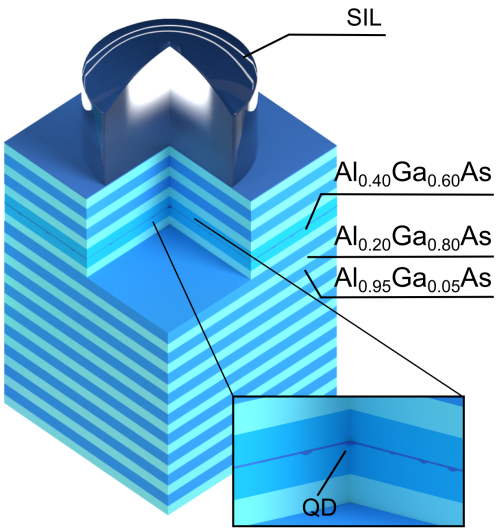

Figure 2.2. Cut diagram of the GaAs droplet etched sample combined with diffused Bragg reflectors (DBR) and a solid immersion lens (SIL). The QD layer is obtained by filling nanoholes in a $Al_{0.4}Ga_{0.6}As$ layer with a 2 nm GaAs layer for a total thickness of 123 nm. The cavity is completed by adding two 60 nm thick $Al_{0.2}Ga_{0.8}As$ layers around the active layer and two DBRs constituted by 2 pairs (top) and 9 pairs (bottom) of $Al_{0.95}Ga_{0.05}As$ (70 nm) and $Al_{0.2}Ga_{0.8}As$ (60 nm) layers.

2.1.1 Two-photon excitation

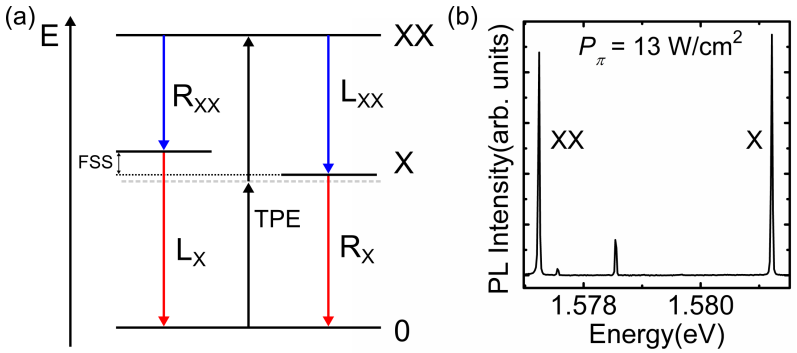

Figure 2.3. (a) Energy scheme of the X-XX cascade and sketch of the two-photon excitation scheme (TPE). In TPE, the QD is excited by a pulsed laser tuned at half the energy difference between the XX level and the ground state (0). The two-photon cascade follows two paths leading to a polarization-entangled state. (b) Photoluminescence spectrum of the QD under TPE resonant scheme. The X and XX lines are clearly distinguishable. The power density at π-pulse (P_π) is obtained with an 80 MHz repetition rate and a pulse FWHM of about 10 ps. From Ref. [77].

In order to achieve an on-demand operation, we need to coherently populate the XX state with a pulsed source. A two-photon resonant excitation scheme (TPE), see Fig. 2.3(a), is routinely employed [37, 78]. The XX state is populated by shining a laser tuned at half the energy of the 0-XX transition. It is worth mentioning that in the GaAs QDs used in this work, the two-particle energy of the XX state with respect to the ground state is lower than double the energy of the X state [60], see Section 1.3.3, thus removing the possibility to directly excite the X state with a single photon from the laser. The resulting emission spectrum is shown in Fig. 2.3(b), where the excitation laser is strongly suppressed by using notch filters. The equal peak intensity of X and XX lines also suggests that dark-exciton scattering plays a secondary role in this excitation scheme.

A way to assess the efficiency of the TPE is the probability that a single laser pulse excites the QD. The preparation fidelity (η_{prep}) is the parameter that describes the efficiency of the excitation scheme and can be measured in a few ways. An indirect method quite commonly used in literature consists in the analysis of the Rabi oscillations with increasing excitation power [37, 79]. Taking into account the phonon contribution in the damping of the Rabi oscillations, the preparation fidelity can be estimated as the ratio between the intensity at π-pulse and the intensity at zero laser power, extrapolated with an exponential fit of the oscillation maxima, see Fig. 2.4(a). A second and more reliable method consists in measuring the normalized counts at zero-time delay in an intensity cross-correlation measurement between the X and XX photons. When the preparation fidelity is below unity, the probability of

finding an X photon is higher if a XX photon belonging to the same radiative cascade is also detected. More specifically, the intensity cross-correlation histogram (with no polarization selection) allows to directly compare the probability of detecting an X photon if a XX photon excited from the same or a subsequent laser pulse is observed. In this case, the preparation fidelity is simply the ratio between the coincidence peaks belonging to subsequent pulses and the one belonging to the same excitation pulse, see Fig. 2.4(b). A preparation fidelity as high as 0.91(3) [52] is measured with a TPE scheme on the epitaxial GaAs QDs reported in the Figure. It is important to note that comparing the events triggered by consecutive pulses may neglect processes related to optical inactivity on longer time scales. These effects, commonly referred to as blinking, can be accounted for by comparing the zero-time delay peak in the coincidences histogram with its limit value at longer time delays, as assessed in more detail in the following Section.

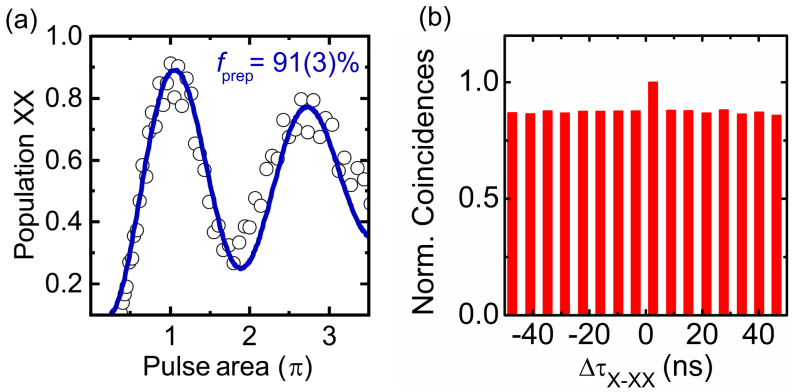

Figure 2.4. (a) Rabi oscillations of the XX emission intensity vs laser power. The preparation fidelity (η_{prep}) is calculated as the ratio between the intensity of the π-pulse and the maximum intensity reachable considering only a phonon-induced damping of the oscillations, from Ref. [52]. (b) XX-X cross-correlation histogram without any polarization selection. The peak at zero-time delay represents photons belonging to the same cascade. The higher correlation with respect to subsequent pulses is a direct estimation of the preparation fidelity. From Ref. [77].

2.1.2 Multi-photon emission

One of the fundamental requirements for many quantum cryptography protocols is the absence of multiphoton emission. If we restrict ourselves to the excitonic transition we can consider the QD as a two-level system. After being excited, the X state in the QD is occupied and the QD cannot accept further excitations. This represents a hard constraint in emitting two photons at the same time so that the emission of light from a QD state is intrinsically single-photon like.

In order to evaluate the multi-photon emission probability of a source, the

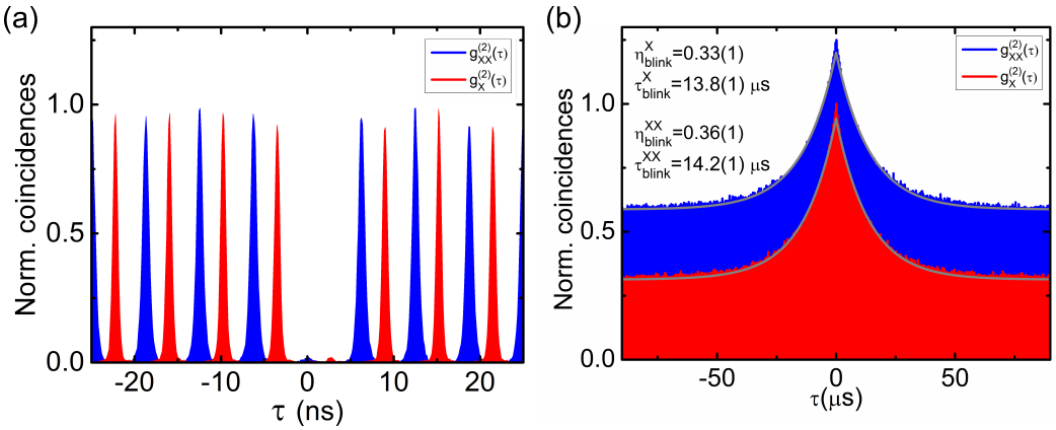

Figure 2.5. (a) Second-order autocorrelation function, $g^{(2)}(\tau)$, measured for the XX (blue histogram) and X (red histogram) emission showing suppressed emission around zero-time delay. The histograms are shifted in time for clarity. The values of the $g^{(2)}(0)$ are 0.027(2) and 0.022(2) for the X and XX respectively. (b) Long-range $g^{(2)}(\tau)$ measured for the X and XX emission, the XX histogram has a 0.25 vertical offset for clarity. It is visible an enhancement in the coincidences rate at short time scales ($|\tau| < 25\,\mu s$) due to the effect of blinking. Two exponential fits (gray line) extract the mean fraction of on-time of the QD $\eta^{X}_{blink} = 0.33(1)$ and $\eta^{XX}_{blink} = 0.36(1)$ and the mean active time of the emitter $\tau^{X}_{blink} = 13.8(1)\,\mu s$ and $\tau^{XX}_{blink} = 14.2(1)\,\mu s$. Adapted from Ref. [77].

Hanbury-Brown and Twiss interferometer is routinely used [80]. The signal from the investigated source is sent to the entrance port of a balanced beamsplitter and the signal intensity at the two output ports is measured with two SPD. The second-order intensity correlation function $g^{(2)}(\tau)$ is reconstructed from the histogram of the coincidences at the two detectors. The value of the $g^{(2)}(\tau)$ at $\tau = 0$ gives a good estimation of the multiphoton-emission probability. The vanishing $g^{(2)}(\tau \to 0)$ for light emitted from a QD is a clear indication of single-photon emission.

For the GaAs QDs used in the experimental implementations of the teleportation protocols values of the $g^{(2)}(0)$ of 0.027(2) and 0.022(2) for the X and XX respectively are reached, see Fig. 2.5(a). This already very low values are mostly limited by non-perfect laser suppression and detector afterpulsing, as demonstrated by the record-low value of $g^{(2)}_{XX}(0) = (75(16)) \times 10^{-6}$ which has been recently reported in literature for the same QD system, with the same excitation scheme, polarization suppression of the laser, and low-dark count detectors [38]. As mentioned above, the long-time ($|\tau| > 25\,\mu s$) $g^{(2)}(\tau)$ of either the XX or the X (see Fig. 2.5(b)) provides information on the intermittent emission of single photons from the source, also known as blinking. This is an important QD parameter that has to be taken into account when coincidence measurements are to be evaluated [74]. The origin of blinking is still under investigation, the most widely accepted explanation is that long-lived charged states hinder the absorption of light by the QD until the charge

is thermodynamically removed or neutralized. Using a telegraphic model [81] one can estimate from the $g^{(2)}(\tau)$ measurements the fraction of time in which the QD is optically active, η_{blink} as well as the mean blinking time τ_{blink}. For example, for the GaAs QDs which will be presented in the next Chapter, these values were estimated to be $\eta_{blink} = 0.36(1)$ and $\tau_{blink} = 9.0(1)\,\mu s$. As blinking in QDs is not negligible, one has to consider it for correct normalization of the $g^{(2)}(\tau)$. This is generally true and needs to be considered whenever the multiphoton emission probability has to be estimated. In the experiments described below, we let interfere photons generated by subsequent laser pulses separated by 2 ns time intervals. The behavior of the $g^{(2)}(\tau)$ relevant for the experiments will then be the one in the short ($|\tau| \sim$ ns) time range.

2.1.3 Indistinguishability

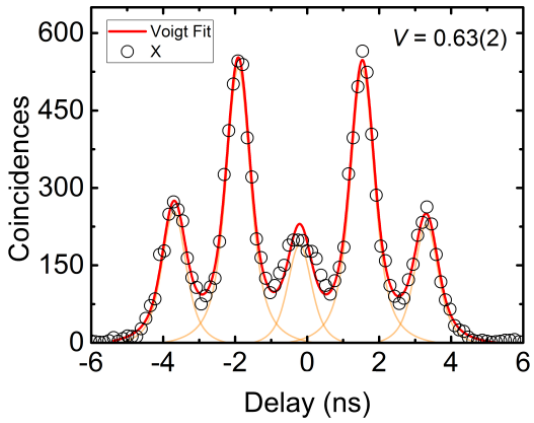

Figure 2.6. Intensity correlation histogram in an HOM experiment for co-polarized X photons emitted at a 1.8 ns delay from the same QD. The value of $V = 0.63(2)$ is extracted from a fit of 5 Voigt peaks fixed width for the Gaussian and Lorentzian parts. From Ref. [53].

The key element of any entanglement-based teleportation protocol is the measurement of the Bell state of two indistinguishable photons. As we saw previously, the correct outcome of a BSM depends on the degree of indistinguishability of the incoming photons and the spatial and temporal overlap of the wave packets.

A correct evaluation of this parameter is therefore of utmost importance for the comparison between theory and experiments. To assess the indistinguishability of our photons we excite the QDs with two π-pulses separated by a delay of $\tau = 2$ ns. The emitted photons are then guided to an unbalanced Mach–Zehnder interferometer equipped with the same 2 ns delay line and are let to interfere at the beamsplitter in co-polarized configuration. The resulting correlation histogram consists of five peaks corresponding to all the possible path combinations of the traveling pulses. If

the two photons are indistinguishable and overlapping in space and time, the HOM effect rules out coincidences at zero delay. From Fig. 2.6, however, one can clearly see that the correlation peak at zero-time delay, corresponding to photons entering the beamsplitter at the same time) is lower than the side peaks (corresponding to photons that entered the beamsplitter at different times) but not zero. This highlights a non-perfect degree of indistinguishability. We use five Voigt functions as an empiric choice to include the instrument response and fit the integrated area of the correlation peaks [53], and we estimate the raw HOM visibility $V = 1 - I(0)/I(\tau)$ (that in a first approximation we assume to be equal to the indistinguishability [82]), which is found to be about 65% for all the experiments discussed in the next Chapter. The accuracy of the visibility estimation is limited by the modeling of the peak at zero-time delay which does not take into account the presence of quantum beats [83] and can be improved when these features are resolved with detectors with better time resolution [84].

The indistinguishability of the two photons from the cascade is limited by an additional time-energy entanglement due to the time ordering of the two-photon emission, which introduces correlations between the arrival times of the emitted photons to the detectors [85, 86]. By using resonant fluorescence schemes, values as high as 0.95(5) for the visibility of the X line were reached with the same GaAs QD, without the need for Purcell enhancement [84]. Unfortunately, this approach cannot provide entangled photon pairs. For this reason, tailoring a different Purcell enhancement for the XX and X transitions to strongly reduce the XX lifetime with respect to the X lifetime can be a viable approach [87, 88].

The indistinguishability of photons emitted by the same QD in short succession is also limited by pure dephasing induced by the solid state environment consisting of phonons and spin noise at nanosecond scale [89, 90]. Their contribution to the indistinguishability is $M = \gamma_{se}/(\gamma_{se}+2\gamma^*)$, where γ_{se} is the spontaneous emission rate and γ^* is the environment induced dephasing [89, 91, 92]. This contribution could be alleviated by increasing the rate of spontaneous emission with Purcell enhancement in an optical cavity [39, 40] or by using spectral filtering at the expenses of source brightness [93].

Spectral diffusion of lines on longer timescales is not an issue when using a single QD excited at short timescales and therefore its effect is usually ignored. When interfacing two remote QDs instead, the independent fluctuations can lead to a massive reduction in values of indistinguishability and their effect must be taken into account [48].

2.1.4 Extraction efficiency

A bright source of photons is a fundamental piece of any quantum communication protocol, and as-grown QDs suffer from one main issue: The high refractive index of semiconductors and the total internal reflection which occurs when light escapes toward a lower index material. The $Al_{0.4}Ga_{0.6}As$ matrix hosting GaAs QDs, for example, has an index of refraction (n) of 3.4 at 780 nm [94]. From Snell's law, when a ray of light passes from an higher n material to a lower one, it cannot cross the interface if it hits the boundary surface with an angle higher than a critical value. In the case of $Al_{0.4}Ga_{0.6}As$ to vacuum (or air) the critical angle is $\sim 17°$. If we imagine that the QD emits light isotropically and a high numerical aperture (NA) objective is used in the collection optics, we can extract from one side of the semiconductor roughly 1% of the photons emitted. And if we also take into account the Fresnel reflection at the surface, this value gets even lower [95].

The total internal reflection is the biggest loss we experience in our system and preventing it would lead to a steep increment in the photon counts at the detectors. Engineering light-matter interaction via nano/micro photonic cavities can alleviate for this problem. Several solutions were proposed during the years, ranging from planar cavities [96], solid immersion lenses [95], optical antennas [97, 98], etched microlenses [99], micropillars [100], hybrid cavities with circular Bragg gratings [101], tapered nanowires [102, 103], microdisks [104], photonic crystals [105], etc.

A simple geometrical solution to alleviate the n mismatch is using a solid immersion lens (SIL) on the surface of the sample. A SIL is a truncated sphere, usually made of high n N-glass (1.84 at 706 nm), with a suitable antireflection coating. The flat side is applied on the the surface of the sample. Since our emitter is very close to the surface ($< 0.5\,\mu m$) with respect to the dimensions of the SIL ($\sim$ mm) we can consider it as it is laying on the surface of the semiconductor. Depending on the distance of the flat surface from the center of the sphere we can distinguish two situations. If the center of the sphere is laying on the flat surface, i.e., the sphere is cut in half, we have a hemisphere SIL. If the center is above the surface by a distance which is equal to r/n, then we are in the so called Weierstrass regime [95].

The main advantage of a hemisphere SIL is that all rays coming from the center of the flat surface cross the top surface of the lens at a 90° angle. No refraction will occur on this surface, which means no total internal reflection and no chromatic aberration occurs. Moreover, the focus of the objective is not changed by the presence of the SIL, a fundamental request when working with high-NA objectives with very low working distances. An hemispherical SIL would then only increase the emission cone angle by reducing the mismatch between the n of the semiconductor and vacuum and by geometrically avoid further refraction at the SIL-vacuum interface

since all rays will come out orthogonal to the SIL surface. The formula for the maximum angle is $\theta_M = \arcsin \frac{n_{SIL} NA}{n_{SC}}$ where we see that for a SIL n approaching the n of the semiconductor we go toward a 100% collection efficiency, when coupled with a mirror on the bottom and not considering Fresnel reflections on surfaces.

The Weirstrass SIL can further improve the situation at the cost of introducing aberrations (irrelevant in the case of monochromatic, point-like single emitters such as QDs) and reducing the working distance of the collection optics (casting its use only to long working-distance optics).

Another approach to increase the emission properties of a QD is to place it in a planar microcavity. By tuning the position of the emitter and the thickness of the cavity we can create constructive interference of the emitted light when reflected from the surfaces and obtain an enhancement of the light extracted from one side of the semiconductor. For the sample used in the experiments described in the next Chapter, the QDs are grown in the middle of a slab enclosed between two DBR. The DBRs are built in the same MBE machine that grows QDs. The machine allows for the controlled growth with nanometric precision of layers of AlGaAs with different Al content. The mirror is created by tuning the n mismatch and thickness of layers so that the light hitting on the DBR is coherently reconstructed in the opposite direction of propagation. DBRs offer the advantage, with respect to metal mirrors, of not creating optical absorption into plasmonic modes. The fact that they can be grown in the same machine that grows the QDs also reduces the number of post-processing steps. Microcavities that are based on DBRs suffer from the limitations of these reflectors, which are not broadband and work only for light hitting at a specific angle, so that some photons can leak into unwanted directions.

The total efficiency of a DBR sample together with the use of a SIL is estimated from experimental data to be 10% [53] for a hemispherical N-glass SIL with antireflection coating and 12% [52] with a Weierstrass zirconia SIL with no coating.

As already mentioned above, better but far more complicated solutions to improve the extraction efficiency can be used and an interesting cavity model that offers a broadband collection efficiency will be discussed in Section 2.2.2.

2.2 Single emitter in a resonator

In order to reach a near-ideal source of entangled photons on demand we first need to be able to address a single emitter and excite it efficiently and then to harvest all the emitted light and direct it to our optical system. As we introduced in Section 2.1.4, the extraction of light from a QD is mainly limited by index of refraction mismatch between the semiconductor and the vacuum. As we will see, two

issues of QDs, i.e., brightness and indistinguishability, can be tackled simultaneously by placing the emitters into an optical microcavity.

By changing the boundary conditions of the electromagnetic field around the emitter we can change the photonic mode density in its neighborhood. With photonic enclosure we can induce a three dimensional confinement of the electromagnetic radiation and the appearance of discrete cavity modes. If the single modes are spread enough so that the emitter can only be coupled to one mode then there will be only one possible channel for the radiative decay and all the photons will be transferred through this channel. If the mode confinement is strong, i.e., if the cavity volume is in the order of some λ^3, the emitting dipole will experience an enhancement of the emission rate with respect to its value in bulk. This effect is named after E. M. Purcell who first observed the phenomenon in microwave cavities [106]. The increment in the emission rate means that the electronic excitations in a QD will interact less with the noisy solid-state environment and, moreover, that the detrimental effect of the time jitter introduced by the two-photon cascade can be reduced. Both these effects would increase the indistinguishability of photons emitted by the same source as well as the entanglement fidelity in QDs with non-zero value of the FSS.

2.2.1 Optical cavities

The most basic optical cavity is constituted by a planar cavity, with a light emitter placed in the center of the distance between two identical planar mirrors. The cavity will allow standing waves only at certain frequencies, enhancing the resonant modes and suppressing the out-of-resonance ones. By tuning the distance of the two mirrors we can tune the resonant mode at the same wavelength of the emission of the emitter. In this way we are altering the allowed electromagnetic modes near the QD and the emission will be enhanced by the presence of the cavity. The interaction of a two-level system, e.g., an atom or a QD, with photons in a cavity requires the introduction of the quantization of the electromagnetic field [107]. To describe the system we resort to the Jaynes-Cummings Hamiltonian:

$$\begin{aligned} \mathcal{H} &= H_{field} + H_{emitter} + H_{interaction} = \\ &= \hbar\omega \left(a^\dagger a + \frac{1}{2} \right) + \hbar\omega \frac{\hat{\sigma}_z}{2} + i\hbar g \left(\hat{\sigma}_- a^\dagger - \hat{\sigma}_+ a \right) \end{aligned} \tag{2.1}$$

where $a^\dagger$ and a are the creation and annihilation operators of the single mode electromagnetic field at frequency ω, $\hat{\sigma}_z$, $\hat{\sigma}_+$, and $\hat{\sigma}_-$ are the pseudo-spin operators of the two level system with $|e\rangle$ and $|g\rangle$ eigenstate for the excited and ground state respectively, and g determines the strength of the interaction. If we have a single

emitter in a cavity with no photon, the system will interact with the vacuum field and its state will oscillate between the ground and excited state with a Rabi frequency $\Omega_R = 2g$. If we consider losses in the cavity by introducing a photon decay rate γ_C, linked to the cavity quality factor Q by the relation $\gamma_C = \omega/Q$, we can distinguish two regimes. If the dissipative losses rate is larger than the light-matter coupling rate, i.e., the interaction between the emitter and the photons in the cavity is slower than the decay rate of the photons, then no oscillation is observed and we are in the so called weak coupling regime. If instead the interaction between the emitter and the photons in the cavity is faster than the decay rate of photons, the QD can reabsorb photons in a reversible process. We call this the strong coupling regime and is usually observed in high-Q cavities [108, 109].

In the weak coupling regime we can treat the coupling to the cavity as a perturbation of the free-space spontaneous emission. The emission of photons is an irreversible process but the light-matter interaction accelerates the spontaneous emission process in what is known in the literature as the Purcell effect.

The Purcell effect

The transition rate for the spontaneous emission from a QD is given by the Fermi's golden rule:

$$\Gamma_{12} = \frac{2\pi}{\hbar^2}|M_{12}|^2\rho(\omega) \tag{2.2}$$

where M_{12} is the transition matrix element and $\rho(\omega)$ is the density of photon states. When we enclose the QD in a cavity with only a single cavity mode ω_c, with a width $\Delta\omega_c$ determined by the cavity quality factor $Q = \omega/\Delta\omega$, the density of states for the cavity will follow a Lorentzian distribution with central frequency of the cavity and FWHM equal to $\Delta\omega_c$. Since there is only one resonant mode, the emission to that mode will be enhanced:

$$\Gamma_{12}^{cav} = F_P \cdot \frac{2\pi}{\hbar^2}|M_{12}|^2\rho(\omega) \tag{2.3}$$

where F_P is the Purcell factor of the cavity defined for a perfectly mode and spatial match of the QD in the cavity as:

$$F_P = \frac{3\lambda_c^3}{4\pi^2}\frac{Q}{V} \tag{2.4}$$

with $\lambda_c = \lambda/n$ the wavelength of the mode in the material with index of refraction n, and V the mode volume in the cavity, which we can approximate as the volume of the cavity. If the emission is strongly enhanced on a single mode, most of the

spontaneous emission will be funneled in that mode and the lifetime of the transition will be reduced. One of the first demonstration of the Purcell effect in semiconductor QDs is dated back to 1998, by J. M. Gérard *et al.* [110]. Since then, the technological achievements disclosed the possibility of QDs emitting inside of cavities with quality factors up to order of 10^6 [111] and mode volumes down to a few λ^3.

Increasing the emission outside of the cavity alone does not mean in general that the collection efficiency of the source, and thus the brightness, is increased. The problem of collecting photons from the QD into the numerical aperture of an objective lens still remains. In this regard, micropillars are extremely good in funneling the radiation into a beam with extremely low divergence and thus a well collimated far-field emission. Light from the QD enclosed in these microcavities can be efficiently collected by objectives with a standard NA of 0.5 [100].

While increasing the quality factor of a cavity represents an exploitable way to produce high-repetition rate single-photon sources [82], it comes with the downside of reducing the width of the resonance and introducing a negative trade-off for the brightness of the source [112, 113]. In the GaAs QDs used in our experiments the binding energy of the XX corresponds to a wavelength distance between the two emitted entangled photons of roughly 2 nm. If we want to accommodate both transitions in the cavity mode to allow for highly efficient entangled-pair emission, we need a broadband cavity and thus a low-Q cavity.

2.2.2 Circular Bragg resonators

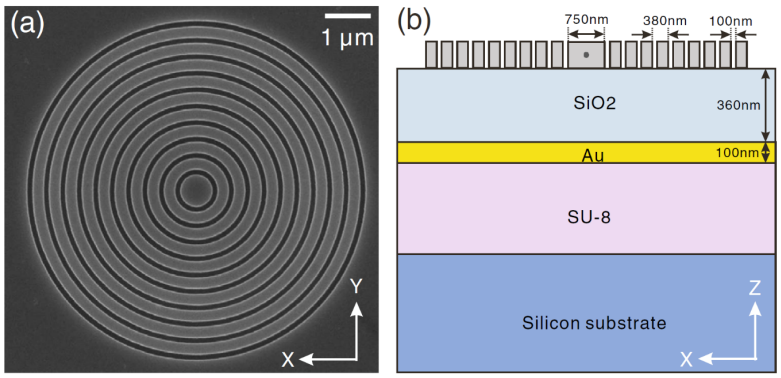

Figure 2.7. (a) Top view of a scanning electron microscope image of the circular Bragg resonator for InGaAs QDs. (b) Side view scheme of the same device. From Ref. [40].

Regarding the emission of entangled photons from a QD in a cavity, a few solutions can be found in literature. Photonic molecules made by two coupled pillars allowed the demonstration of Purcell enhanced emission of entangled photon with a pair rate of 0.12 and a 0.63 entanglement fidelity for unfiltered photons

[71]. Unfortunately, pillar cavities are not ideal for application of strain technology and their fabrication requires several non-trivial processing steps. Another solution worth mentioning is the emission of entangled photon pairs from QDs embedded in nanowires [114, 115]. Also in this case, the geometry of the cavity prevents the efficient transfer of stress and the proximity of the QD to the host semiconductor surface could be detrimental for the indistinguishability of the emitted photons.

The solution we decided to pursue for entangled light generation from QDs is a hybrid photonic structure featuring a single QD in the center of a cylindrical cavity surrounded by a circular second-order Bragg grating. The cavity is known in literature as circular Bragg resonator (CBR), but also commonly referred to as "bullseye" cavity, due to the resemblance to the target of the popular game of dart, see Fig. 2.7(a). The whole structure features a broad cavity mode ($Q \sim 150$), with a simulated Purcell enhancement not exceeding 30 for the cavity central wavelength. The role of the second order Bragg grating is to reflect upwards the photons emitted in the horizontal direction. In the first proposal [101], the membrane containing the QDs was partially etched to create the grating and then back-etched to suspend it and introduce a preferential upwards emission direction. Due to difficulties in the process and leaking downwards photons, the suspended membrane design was substituted by transferring the membrane containing the QDs onto a broadband reflector built with a metal mirror separated from the semiconductor by an oxide layer to avoid coupling with plasmons [39, 40], see Fig. 2.7(b). The cavity is obtained by dry-etching a cylindrical cavity in the AlGaAs membrane, surrounded by a set of concentric rings, with duty cycle and period of the grating tuned to match the second-order Bragg condition. The cavity resonance wavelength shifts linearly with the central cavity diameter and the period of rings, with two different coefficients [40]. The upwards coupling of the in-plane emission is ensured by the second order circular Bragg grating, a concept borrowed from grating couplers in waveguides [116, 117]. The thickness of the AlGaAs/oxide stack is carefully tuned to ensure that the photons leaking downwards are back-reflected and recaptured by the cavity. The simulated collection efficiency is effectively broadband, being above 90% across a bandwidth of 33 nm with a 0.65 NA collection optics. The simulated Purcell factor is above 2 in a bandwidth of 13 nm around the cavity mode. By tuning the cavity mode around the QD emission energy, so that both X and XX photons experience Purcell effect, one could play with the ratio of enhancement to both decrease dephasing by noisy environment on both transition and reduce the time jittering due to emission time uncertainty. The planar geometry of the cavity makes it fully compatible with the strain-tune technology.

Two papers reporting experimental results on CBRs were independently published

in 2019, with identical photonic structures design applied on two different QD materials, that are GaAs [39] and InGaAs [40]. For the GaAs QDs, the presented structures features a 0.86/0.65 single photon/entangled pair extraction efficiency with a modest 3.5 Purcell factor for the X transition, with indistinguishability peaking at the high value of 0.9 for both X and XX photons. The natural low FSS of droplet-etched QDs and the reduced recombination times allowed for high values of entanglement fidelity (0.88) without any external tuning. Similar results hold for the InGaAs QDs.

In Chapter 4 we will present our results in replicating this photonic structure with its integration on micromachined piezo actuators.

Chapter 3

Entanglement teleportation with light from quantum dots

In the previous Chapter we

listed the properties of the light source of choice for the experimental implementation of the entanglement and state teleportation protocols.

In the first section of this Chapter we will offer a theoretical discussion of the entanglement teleportation protocol using a QD entangled photon source. This model helped us to better understand the results of the experiments and to light the path toward the realization of the near-ideal source for the quantum networks.

In the second Section, we give all the details of the experimental setup and the techniques used to investigate the quantum communication protocols described in the previous Chapter and, in the third Section, we will describe the experimental results and give details on the photon correlation analysis performed.

In the fourth and last Section we will apply the theory by simulating the experimental results and we will give a complete review of the effects of the imperfections of the source and of the experimental setup on the final result. At the end of this Chapter, it will be clear why we devoted our efforts in the realization of tunable QDs in CBR cavities.

3.1 Entanglement teleportation protocols with real emitters

After discussing the ideal operation of the entanglement teleportation, we proceed to assess the effects of using real and non-ideal emitters based on QDs, see Refs. [52, 53, 77]. As we already mentioned in the previous Chapter, several physical parameters of the emitter impact the performance of a QD based entangled photon source in

terms of fidelity and the indistinguishability of photons.

For what concerns the generation of entangled photons, the role of the electronic structure of the QD can be mainly ascribed in an effective way to the FSS. The FSS magnitude, S, decreases the entanglement fidelity by introducing a phase evolution (see Section 1.3.4) dependent on the X recombination time. Since this quantity is undetermined within the transition lifetime, the polarization state of the radiative cascade is described as a mixed state between the expected $|\phi^+\rangle$ and the $|\phi^-\rangle$ Bell states, whose purity decreases by increasing the ratio of FSS over radiative linewidth $\hbar/\tau_{\mathrm{X}}$. The FSS also affects negatively the accuracy of the BSM because of the small energy detuning between the two X states which reduces the mode overlap at the beamsplitter of two consecutive X photons.

As expected for an emitter embedded in a solid-state environment, decoherence mechanisms should be considered as well in the source characterization. The interactions that induce decoherence are due to different causes, namely phonon-induced dephasing [118], charge and spin noise [89]. Regardless of the detailed description of the interplay among these effects, the radiation emitted from the QD is described by the coherence time T_2 [119], which depends on the transition lifetime τ and on the dephasing time T_2^*. The presence of dephasing effects lowering the coherence time with respect to the Fourier limit directly affects the photon indistinguishability [120]. Consequently, the accuracy of the optical BSM based on two-photon interference is lowered. As already mentioned in Section 2.1.3, the effect can be empirically quantified by measuring the interference visibility in an HOM experiment, an approach that also helps to keep into account the dynamics of dephasing and spectral diffusion when photons are emitted at a different time from the same source [90, 92]. On the other hand, it is known that most of the decoherence effects that are quantified by the coherence times of the individual XX and X lines do not affect the grade of polarization entanglement from the XX-X cascade [70]. Indeed, the polarization state of the photon pair is only affected by the physical processes that cause decoherence between the two bright X states during the time spent by the system in their superposition state, namely during the intermediate step of the XX-X cascade. To refer to these effects, we define two specific decoherence mechanisms, each with its characteristic time. The distinction is based not on the physical origin, but rather on the effect on the polarization state, specifically on processes that affect the state population and that only act on phase coherence. Consistently with previous works [41, 70], we consider any physical mechanism that cancels any polarization correlation between the photons as a spin scattering term with the characteristic time τ_{SS}. Instead, we name cross-dephasing (with typical time τ_{HV}) the events in which there is a loss in phase coherence between the two

bright X states.

Another possible cause of non-ideal behavior in an on-demand photon source is time jittering. The negative impact of random fluctuations in the pumping process of the XX can be virtually suppressed by the use of resonant excitation [78]. However, time correlations between the photons emitted in the two-photon radiative decay can also affect the indistinguishability of photons taken from different XX-X cascades [87, 88, 121]. Modeling the impact of this contribution and its interplay with other decoherence mechanisms with their dependence on the emission delay is not necessary since all this information is included in the measured values of HOM visibility. Also, the impact of time jittering on the accuracy of the BSM can hence be quantified due to the knowledge of an easily accessible experimental quantity.

Finally, multiphoton emission and background laser light both decrease the entanglement fidelity and BSM accuracy by introducing spurious coincidence events at the detectors. We can describe this effect by introducing the fraction of photon pairs that both come from a radiative XX-X cascade with respect to the total number of detected pairs. We call this quantity k. We can estimate the fraction k of the exploitable photons by first defining a parameter g as the $g^{(2)}(0)$ autocorrelation function for X and XX normalized with the mean value of the autocorrelation peaks around zero-time delay [122]. The parameter g is the normalized probability of multiphoton events and corresponds to the probability that two photons are detected from the same pulse for either of two subsequent pulses, divided by the probability that a single photon is detected from each pulse. This quantity is most relevant to the experiment discussed here, in which two entangled pairs emitted consecutively are considered.

If we assume strong photon anti-bunching, the value of k can be estimated, taking also into account the preparation fidelity η_{prep}, as $k \approx 1 - \eta_{prep} \cdot (g_{\mathrm{X}} + g_{\mathrm{XX}})/2$. In the following calculations, we will only consider multiphoton emission from the XX side as the effect of g_{X} already enters in the BSM accuracy (see below) so that $k \approx 1 - \eta_{prep} \cdot g_{\mathrm{XX}}/2$.

In our experiments, the two EPSs are simulated by exciting the same QD twice with delayed laser pulses. This results in the generation of two entangled photon pairs, that are identified according to their time of creation as early (E) and late (L): $|\phi^+\rangle_E$ and $|\phi^+\rangle_L$. We introduce the indices XX_E, X_E and XX_L, X_L in place of the numbers 1–2 and 3–4 we used in Section 1.2.1, so that the labeling more closely reflects the physical system used in the experiments.

In general, we should better describe the two-photon polarization state by introducing the density matrices of the two states $\rho_{\mathrm{X}_E,\mathrm{XX}_E}$ and $\rho_{\mathrm{X}_L,\mathrm{XX}_L}$ and by taking into account all the contributions from the non-idealities discussed so far.

We assume that the probability that, at a given X recombination time t, the system has totally lost the polarization correlation, due to either background emission or a spin scattering event, is given by

$$p_{k,\tau_{SS}}(t) = (1-k) + \int_0^t dt' \cdot \frac{k \cdot e^{t'/\tau_{SS}}}{\tau_{SS}} = 1 - k \cdot e^{-t/\tau_{SS}} \tag{3.1}$$

This term acts by bringing the state toward the direction of a completely mixed diagonal state. Similarly, we estimate the probability that the phase coherence is lost, yet without any spin-flip of the exciton state, by a cross-dephasing event as:

$$p_{\tau_{HV}}(t) = (1 - p_{k,\tau_{SS}}(t)) \cdot \int_0^t dt' \cdot \frac{e^{-t'/\tau_H V}}{\tau_{HV}} = k \cdot e^{-t/\tau_{SS}} \cdot \left(1 - e^{-t/\tau_{HV}}\right) \tag{3.2}$$

This term affects the two-photon state by destroying the entanglement but keeping the classical polarization correlation of the XX-X cascade. Last, we add the FSS contribution. The FSS makes the state oscillate between the $|\phi^+\rangle$ and $|\phi^-\rangle$ Bell states with an angular frequency equal to $S/\hbar$ and its contribution to the matrix is multiplied by the probability of not having any decoherence or spin-flip. The time-dependent density matrix for the XX-X state in the two qubits base $|HH\rangle, |HV\rangle, |VH\rangle, |VV\rangle$ reads as:

$$\begin{aligned}
\rho_{\mathrm{X,XX}}(t) = &\left(1 - k \cdot e^{-\frac{t}{\tau_{SS}}}\right) \cdot \frac{1}{4} \begin{pmatrix} 1 & 0 & 0 & 0 \\ 0 & 1 & 0 & 0 \\ 0 & 0 & 1 & 0 \\ 0 & 0 & 0 & 1 \end{pmatrix} + \\
&+ k \cdot e^{-\frac{t}{\tau_{SS}}} \cdot \left(1 - e^{-\frac{t}{\tau_{HV}}}\right) \cdot \frac{1}{2} \begin{pmatrix} 1 & 0 & 0 & 0 \\ 0 & 0 & 0 & 0 \\ 0 & 0 & 0 & 0 \\ 0 & 0 & 0 & 1 \end{pmatrix} + \\
&+ k \cdot e^{-}\frac{t}{\tau_{SS}} \cdot e^{-\frac{t}{\tau_H V}} \cdot \frac{1}{2} \begin{pmatrix} 1 & 0 & 0 & e^{-\frac{iSt}{\hbar}} \\ 0 & 0 & 0 & 0 \\ 0 & 0 & 0 & 0 \\ e^{\frac{iSt}{\hbar}} & 0 & 0 & 1 \end{pmatrix}
\end{aligned} \tag{3.3}$$

The other figure of merit we need to consider in our calculation is the photon indistinguishability. As already mentioned, a value below unity of indistinguishability affects the performance of the BSM. If the space-temporal overlap of the modes [83] involved in the two-photon interference is not perfect, double-clicks at the detectors could be triggered by Bell states other than $|\psi^-\rangle$. Thus, errors in the BSM will directly lower the success rate of the teleportation. This effect can be estimated

from an experimentally accessible quantity, as the indistinguishability M can be approximated by the HOM visibility V. These quantities differ when background light and multiphoton emission are also considered. However, for the purposes of the following derivation and taking into account the small values of g_{X} typical of our source we can just consider the HOM visibility V. The HOM visibility is measured by sending co-polarized photons in the BSM setup and measuring the second-order correlations, as described in Section 1.2.3. It follows that when a $|\phi^{\pm}\rangle$ state, which features co-polarized photons, enters the setup, the conditioned probability to get a double click at the output of the beamsplitter, mimicking a $|\psi^{-}\rangle$ state (we indicate such event with the short notation BSM_{ψ^-}), is linked to the HOM visibility by the relation:

$$p\left(BSM_{\psi^-}|\phi^{\pm}\right) = \frac{1-V}{2} \tag{3.4}$$

If we take into account the $|\psi^{+}\rangle$ state, which has the same spatial symmetry of the $|\phi^{\pm}\rangle$ states, we would expect the same behavior described in Eq. 3.4. This assumption is only valid in the limit of vanishing FSS. If the degeneracy of the X state is lifted, the photons emitted with orthogonal linear polarization along the anisotropy axes of the QD have a different energy. The small frequency detuning reduces the mode overlap of the two orthogonally polarized states from $M_{\parallel}$ to a lower value $M_{\perp}(S)$, which decreases with increasing FSS. This effect is taken into account by multiplying the visibility by the ratio $r_{\delta\omega}(S) = M_{\perp}(S)/M_{\parallel}$ in the probability of Eq. 3.4 so that the probability that a $|\psi^{+}\rangle$ state produces a false BSM_{ψ^-} reads as:

$$p(BSM_{\psi^-}|\psi^{+}) = \frac{1 - V \cdot r_{\delta\omega}(S)}{2} \tag{3.5}$$

The dependence of $r_{\delta\omega}$ on the FSS is ruled by the effect of frequency detuning on the two-photon interference [83], given that the oscillator strength for the two X transitions remains approximately equal. The specific expression of this dependence is affected by the other mechanisms which are present and reduce the HOM visibility [123]. For example, if we assume that the HOM visibility is mainly limited by pure dephasing and temporal delay or jittering, the following analytical form is obtained:

$$r_{\delta\omega}(S) = \frac{1}{1 + \left(\frac{S\tau_{\mathrm{X}}}{\hbar} g^{(1)}_{deph}\right)^2} \tag{3.6}$$

where

$$g^{(1)}_{deph} = \frac{1}{1 + \frac{2\tau_{\mathrm{X}}}{T_2^*}} \tag{3.7}$$

and T_2^* is the characteristic time of pure dephasing.

Finally, since no coincidences dip is recorded at zero time delay for an HOM experiment with randomly cross-polarized pairs, the probability of having a double click from the BSM detectors is 1/2 if a random mixture of $|\psi^-\rangle$ and $|\psi^+\rangle$ is sent in the BSM setup. From this information, it directly follows that the probability of joint measurement for $|\psi^-\rangle$ is:

$$p\left(BSM_{\psi^-}|\psi^-\right) = \frac{1 + V \cdot r_{\delta\omega}(S)}{2} \tag{3.8}$$

Since X_L and X_E are generated by two different emission cascades, they are uncorrelated in polarization. This, together with the fact that they are unpolarized, implies that we can describe their state as a mixed state of all the Bell states with equal probability:

$$p(\phi^\pm) = p(\psi^\pm) = \frac{1}{4} \tag{3.9}$$

The probability of having a BSM_{ψ^-} is the sum over over all the possible outcomes weighted with their probability:

$$\begin{aligned} p(BSM_{\psi^-}) = {} & p(BSM_{\psi^-}|\phi^+)p(\phi^+) + p(BSM_{\psi^-}|\phi^-)p(\phi^-) + \\ & + p(BSM_{\psi^-}|\psi^+)p(\psi^+) + p(BSM_{\psi^-}|\psi^-)p(\psi^-) = \qquad (3.10) \\ = {} & \frac{1 - V/2}{2} \qquad (3.11) \end{aligned}$$

Finally, the probability that a BSM_{ψ^-} is caused by a specific Bell state is then given by the Bayes' theorem, e.g.,

$$p(\psi^-|BSM_{\psi^-}) = \frac{p(BSM_{\psi^-}|\psi^-)}{p(BSM_{\psi^-})} p(\psi^-) \tag{3.12}$$

and the conditioned probabilities for all the possible Bell states are:

$$\begin{aligned} p(\psi^\pm|BSM_{\psi^-}) &= \frac{1 \mp V r_{\delta\omega}(S)}{4 - 2V} \\ p(\phi^\pm|BSM_{\psi^-}) &= \frac{1 - V}{4 - 2V} \end{aligned} \tag{3.13}$$

3.1.1 Entanglement teleportation

We can now extend the theory of entanglement teleportation for pure states to a more generic case using the density matrix formalism and taking into account real QDs. The matrix corresponding to the four-photon state written in Eq. 1.3 is described by the tensor product of matrices from Eq. 3.3, $\rho_{X,XX}(t_E) \otimes \rho_{X,XX}(t_L)$,

combining the E and L radiative cascades with their X recombination times t_E and t_L. The event of a $|\psi^-\rangle$ state triggering the BSM on the state of photons X_E and X_L is represented by the projection operator $\Pi^{\psi^-}_{\mathrm{X}_E,\mathrm{X}_L} = |\psi^-\rangle_{\mathrm{X}_E,\mathrm{X}_L}\langle\psi^-|_{\mathrm{X}_E,\mathrm{X}_L}$. The density matrix for the teleported two-photon state of XX_E and XX_L is then obtained by tracing out X_E and X_L from the four-photon density matrix [124]:

$$\rho^{\psi^-}_{\mathrm{XX}_E,\mathrm{XX}_L}(t_E,t_L) = \mathrm{Tr}_{\mathrm{X}_E,\mathrm{X}_L}\left[\frac{\Pi^{\psi^-}_{\mathrm{X}_E,\mathrm{X}_L}\left(\rho_{\mathrm{X,XX}}(t_E)\otimes\rho_{\mathrm{X,XX}}(t_L)\right)\Pi^{\psi^-}_{\mathrm{X}_E,\mathrm{X}_L}}{N^{\psi^-}}\right] \tag{3.14}$$

where N^{ψ^-} is a normalization factor.

To reconstruct the teleported state, we perform quantum state tomography that collects a large number of recombination events. The experimental density matrix is best simulated by integrating Eq. 3.14 over the possible X recombination times weighted by their probability

$$\rho^{\psi^-}_{\mathrm{XX}_E,\mathrm{XX}_L} = \int_0^\infty dt_L \int_0^\infty dt_E \cdot \frac{e^{-(t_L+t_E)/\tau_\mathrm{X}}}{\tau_\mathrm{X}^2} \cdot \rho^{\psi^-}_{\mathrm{XX}_E,\mathrm{XX}_L}(t_E,t_L) \tag{3.15}$$

where τ_X is the radiative lifetime of the X.

We can now obtain the final polarization of the state of the teleported XX photons by summing the density matrices obtained in Eq. 3.15 for each Bell state outcome by the probability that a specific Bell state induced a BSM described in Eq. 3.13. As a first approximation, we do not consider any explicit dependance of the interference visibility on the recombination times t_E and t_L. To simplify the expression, we contract the contribution of the different decoherence effects in the terms

$$g'^{(1)}_{H,V} = \frac{1}{1+\frac{\tau_\mathrm{X}}{\tau_{SS}}} \tag{3.16}$$

$$g^{(1)}_{H,V} = \frac{1}{1+\frac{\tau_\mathrm{X}}{\tau_{SS}}+\frac{\tau_\mathrm{X}}{\tau_{HV}}} \tag{3.17}$$

The final matrix has the form:

$$\rho^{swap}_{\mathrm{XX}_E,\mathrm{XX}_L} = \sum_{i=\phi^+,\phi^-,\psi^+,\psi^-} p(i|BSM_{\psi^-}) \cdot \rho^{i}_{\mathrm{XX}_E,\mathrm{XX}_L} = \tag{3.18}$$

$$= \frac{1}{4}\begin{pmatrix} 1-\frac{V}{2-V}\left(kg^{(1)}_{H,V}\right)^2 & 0 & 0 & 0 \\ 0 & 1+\frac{V}{2-V}\left(kg^{(1)}_{H,V}\right)^2 & -2\frac{V}{2-V}\frac{r_{\delta\omega}(S)\left(kg^{(1)}_{H,V}\right)^2}{1+\left(\frac{S\tau_{\mathrm{X}}}{\hbar}g^{(1)}_{H,V}\right)^2} & 0 \\ 0 & -2\frac{V}{2-V}\frac{r_{\delta\omega}(S)\left(kg^{(1)}_{H,V}\right)^2}{1+\left(\frac{S\tau_{\mathrm{X}}}{\hbar}g^{(1)}_{H,V}\right)^2} & 1+\frac{V}{2-V}\left(kg^{(1)}_{H,V}\right)^2 & 0 \\ 0 & 0 & 0 & 1-\frac{V}{2-V}\left(kg^{(1)}_{H,V}\right)^2 \end{pmatrix}$$

It is worth noticing that the density matrix has a very simple structure and the role of the various imperfections of the source is consistent with qualitative expectations.

The density matrix has no imaginary part, differently from the matrix of the starting EPSs. This is due to the fact that the phase evolution due to the FSS does not depend on the sole X recombination time, but rather on the difference between the X recombination time in the two cascades with a phase factor $e^{-\frac{iS(t_E-t_L)}{\hbar}}$. Averaging over several repetitions of the process as in the experimental quantum tomography, this term leaves no imaginary component. Consistently, the first eigenvector of the reconstructed density matrix after teleportation is always $|\psi^-\rangle$, even if the one relative to the EPSs rotates with respect to $|\phi^+\rangle$ when the ratio between the FSS and the radiative lifetime is increased [125]. Overall, the effect of the FSS, and similarly of any possible cross-dephasing mechanism, is to reduce the out-of-diagonal elements of the density matrix and induce a mixing of the $|\psi^-\rangle$ and $|\psi^+\rangle$ state. Such an effect still allows one to observe correlations in the HV basis, which can solely arise from classical correlations in the starting photon pairs and a successful BSM. Instead, low photon indistinguishability, decoherence mechanisms as spin scattering, and multiphoton emission, all modify the diagonal elements as well, which is a direct consequence of the fact that they cancel every correlation in polarization.

It should be noted that in other implementations of the BSM including polarizing elements, such as the 50% efficiency scheme implemented with linear optics [126], the Bell state is selected also relying on correlations in the HV basis, effectively removing false double-clicks from the $|\phi^{\pm}\rangle$ states which implies $p(BSM_{\psi^-}|\phi^{\pm}) = 0$. The density matrix in this case takes only the sum on the $|\psi^{\pm}\rangle$ states and the matrix

for a swapping to the $|\psi^-\rangle$ state becomes:

$$\rho^{swap}_{\mathrm{XX}_E,\mathrm{XX}_L} = \sum_{i=\phi^+,\phi^-,\psi^+,\psi^-} p(i|BSM_{\psi^-}) \cdot \rho^{i}_{\mathrm{XX}_E,\mathrm{XX}_L} = \tag{3.19}$$

$$= p(\psi^-|BSM_{\psi^-}) \cdot \rho^{\psi^-}_{\mathrm{XX}_E,\mathrm{XX}_L} + p(\psi^-|BSM_{\psi^+}) \cdot \rho^{\psi^+}_{\mathrm{XX}_E,\mathrm{XX}_L} =$$

$$= \frac{1}{4} \begin{pmatrix} 1 - \frac{V}{2-V}\left(kg^{,(1)}_{H,V}\right)^2 & 0 & 0 & 0 \\ 0 & 1 + \left(kg^{,(1)}_{H,V}\right)^2 & -2V\frac{r_{\delta\omega}(S)\left(kg^{(1)}_{H,V}\right)^2}{1+\left(\frac{S\tau_{\mathrm{X}}}{\hbar}g^{(1)}_{H,V}\right)^2} & 0 \\ 0 & -2V\frac{r_{\delta\omega}(S)\left(kg^{(1)}_{H,V}\right)^2}{1+\left(\frac{S\tau_{\mathrm{X}}}{\hbar}g^{(1)}_{H,V}\right)^2} & 1 + \left(kg^{,(1)}_{H,V}\right)^2 & 0 \\ 0 & 0 & 0 & 1 - \frac{V}{2-V}\left(kg^{,(1)}_{H,V}\right)^2 \end{pmatrix}$$

A similar matrix is obtained for the $|\psi^+\rangle$ Bell state detection.

3.1.2 State teleportation

An analogous description can be obtained for the state teleportation experiment. Assuming that the preparation of the state $|\phi\rangle_1$ to be teleported, see Eq. 1.5, is performed on the X photon excited by the later laser pulse, the density matrix for the three-photon state can be written as:

$$\rho^{|\Psi\rangle_{123}} = |\phi\rangle_{\mathrm{X}_L}\langle\phi|_{\mathrm{X}_L} \otimes \rho_{\mathrm{X}_E,\mathrm{XX}_E} \tag{3.20}$$

where the density matrix $\rho_{\mathrm{X}_E,\mathrm{XX}_E}$ that describes the EPS has already been integrated over the possible X recombination times and thus follows the expression also reported in Ref. [70].

The density matrix of the teleported state after a BSM of the $|\psi^-\rangle$ state with arbitrary accuracy can be constructed in a similar manner as Eq. 3.14 and Eq. 3.18, respectively

$$\rho^{\psi^-}_{\mathrm{XX}_E} = \mathrm{Tr}_{\mathrm{X}_E,\mathrm{X}_L}\left[\frac{\Pi^{\psi^-}_{\mathrm{X}_E,\mathrm{X}_L}\rho^{|\Psi\rangle_{123}}\Pi^{\psi^-}_{\mathrm{X}_E,\mathrm{X}_L}}{N^{\psi^-}}\right] \tag{3.21}$$

$$\rho^{telep}_{\mathrm{XX}_E} = \sum_{i=\phi^+,\phi^-,\psi^+,\psi^-} p(i|BSM_{\psi^-}) \cdot \rho^{i}_{\mathrm{XX}_E} \tag{3.22}$$

Also for the case of the quantum state teleportation, the implementation of a 50% BSM increases the accuracy of the measurement and has an important impact on the fidelity of the protocol, as we will see in Section 3.4.2.

3.2 Experimental implementation

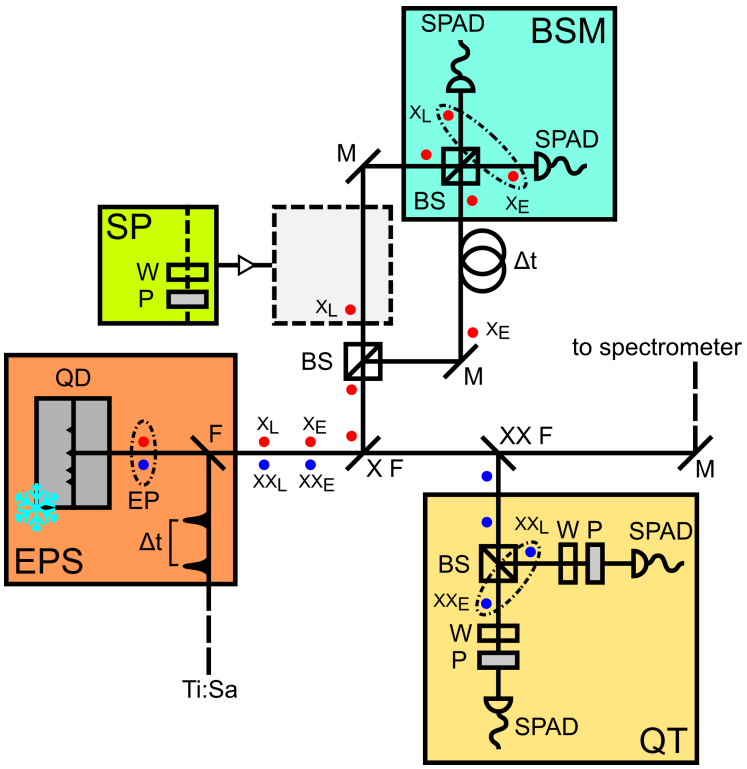

Figure 3.1. Setup scheme for the entanglement (state) teleportation experiments. A Ti:Sa laser emits two light pulses separated by a $\Delta t = 1.8\,\mathrm{ns}$ with a 160 MHz repetition rate. Laser light is directed to a cryostat hosting the QD sample. The sample is kept under a high vacuum at $T = 5\,\mathrm{K}$. The excited QD emits two entangled photon pairs (EPs) at an early (E) and late time (L), each represented by a blue and a red dot. Backscattered laser light is filtered out with volume Bragg grating (VBG) filters (F). X photons are reflected with a VBG notch filter (X F) tuned at the X emission energy and sent to an unbalanced Mach-Zehnder interferometer with the same delay Δt separating two subsequently excited EPs. The two X photons are sent to the setup for the Bell state measurement (BSM). The setup consists of a beamsplitter and two single-photon avalanche photodiode detectors (SPAD). The signal from the SPADs is sent to a time-to-digital converter for coincidences analysis. XX photons are separated with another VBG notch filter and sent to the setup for the quantum tomography (QT) to check the teleported entangled state. Here the signal is separated with a BS and polarization dependent cross-correlations of the photons are performed by placing a waveplate (W) and a linear polarizer (P) in front of each of the two SPADs. To perform the state teleportation experiment, a polarizer and a waveplate are placed on the short arm of the unbalanced MZ to prepare the state (SP) of the X_L photon. Only the teleported XX_E photon is then analyzed in the QT setup. From Ref. [77].

The two experimental setups for performing entanglement teleportation and state teleportation [127–129] are sketched in Fig. 3.1. For both the experiments, the GaAs QDs are kept at cryogenic temperature ($T < 10\,\mathrm{K}$).

For the entanglement teleportation experiment, the sample is placed in a closed-

cycle He cryostat buried inside an optical table with active-damping (AttoDry800 from Attocube). The chamber of the cryostat is kept in a high vacuum and the sample is cooled down to 5 K for the experiments. A vacuum- and cryogenic-compatible 0.81-NA microscope objective (LT-APO/NIR/0.81), optimized to work in the near infrared spectral region, is placed above the sample in the cryostat chamber and thermally connected to the cold finger of the cryostat. This ensures an almost perfect mechanical coupling between the objective and the sample with no drift of the QD position over time. The objective is used to focus the excitation laser and to collect the emission from the QDs. The sample can be moved below the objective using a three-axis piezo-actuator stack with sub-micrometer precision. The cryostat cold finger is mechanically decoupled from the cryostat compressor, and this, together with the active damping of the optical table ensures low vibrations of the sample when the cryostat is operating.

The state teleportation experiment is instead performed with a liquid He-flow cryostat from CryoVac. The collection and excitation is ensured by a long-working distance 0.42 NA microscope objective (Mitutoyo M Plan Apo NIR 50X), mounted on a linear piezoelectric actuator to focus on the sample from outside the cryostat. To move the sample, the whole cryostat is mounted on two linear stages.

The resonant excitation source is the pulsed emission from a Ti:Sa tunable femtosecond mode-locked laser (Chameleon Ultra II from Coherent) with a 80 MHz repetition rate. The repetition rate of the laser is first doubled with an unbalanced Mach-Zehnder with a delay line of ~ 6.25 ns. The doubled laser repetition rate is then doubled again with a delay between the two pulses of $\Delta t = 1.8$ ns, to doubly excite the QD every 6.25 ns and simulate two EPSs. The laser pulse is shaped with a custom-built $4f$ pulse-slicer equipped with two diffraction gratings and a variable slit placed in its Fourier plane. In this way, the laser bandwidth and position can be finely adjusted to obtain picosecond pulses (~ 200 µeV) of adjustable energy. This setup allows for the laser energy to be precisely tuned to half the energy of the XX level for the TPE scheme as explained in Section 1.3.3. The laser light is introduced in the beam path toward the cryostat with a 10:90 beamsplitter with low polarization sensitivity. Both the QD emission and the scattered laser coming back from the cryostat pass through the same 10:90 beamsplitter. The laser light is filtered out with a series of three notch filters based on volume Bragg gratings (VBGs) with a bandwidth of 0.4 nm each. The 10:90 beamsplitter and the VBG filters are represented as one element (F) in Fig. 3.1.

Since the XX and X photons have different energies they can be separated with a spectral filter. To do so we use another VBG notch filter tuned to the X energy (X F) to remove the Xs from the emission beam. The reflected light is collected by

a mirror and sent to the BSM setup. The whole system is mounted on a breadboard that can rotate around the center of the VBG filter in order to collect the reflection from the VBG at different wavelengths. The whole BSM setup is mounted on the same breadboard. In the BSM setup, an unbalanced Mach-Zehnder interferometer (MZ) with a delay between the arms matching the Δt of the laser pulse distance, can remove the time distance between E and L photons. In this way, we remove the which-path information between the two X photons so that we can induce the two-photon interference necessary to measure the Bell states. The second BS of the MZ interferometer is a single-mode fiber-coupled 50:50 beamsplitter. We measure the coincidences at the two output ports of the beamsplitter with a pair of Si single-photon avalanche photodiodes (SPADs). The SPADs (τ-SPAD from PicoQuant) have a time jitter of approximately 400 ps and a quantum efficiency of approximately 65% at 780 nm. As already explained previously, for the two experiments we implemented only the measurement of a single Bell state, namely $|\psi^-\rangle$ [130].

A second VBG notch filter (XX F) is tuned at the XX wavelength and sends photons to the setup for quantum state tomography (QT), mounted on a second breadboard coupled to a rotational mount. Here, we perform polarization-dependent cross-correlation measurements by dividing the signal with a non-polarizing BS and placing a polarization analyzer, i.e., a half-waveplate and a quarter-waveplate (W) followed by a linear polarizer (P), in front of each of other two SPADs (SPCM-NIR from Excelitas). When a $|\psi^-\rangle$ is detected at the BSM, the QT of the XX photons is measured.

For the state teleportation experiments, we modify the setup by placing a state preparation (SP) device consisting of a polarizer followed by a waveplate in the short arm of the MZ interferometer, specifically in the X_L path.

The signal coming from the (3)4 detectors is sent to a time-to-digital converter which converts the inputs in time tags with a 10 ps time jitter (Time Tagger Ultra from Swabian Instruments for the entanglement teleportation experiment or HydraHarp 400 from PicoQuant for the state teleportation). The data stream from the tagger is sent to a computer for acquisition and subsequently analyzed. The software that handles the data flow, builds the correlations, and analyzes the data is custom written in the laboratory.

To characterize the QD emission spectrum, the system is equipped with a He-Ne laser for above band excitation and a 0.75 m spectrometer equipped with an 1800 g/mm diffraction grating and a liquid-N_2 cooled Si-CCD camera. To measure the lifetime of the X and XX transitions we couple a SPAD with a much shorter time jitter (PDM from Micro Photon Devices with less than 50 ps time resolution) to a

second exit port of the spectrometer. By selecting the single XX or X lines with the spectrometer grating, time histograms of the arrival times of photons can be measured with the TTL signal from the pulsed laser as a time reference.

To measure the correct state at the BSM setup we need that both photons entering the setup experience the same effect in terms of rotations of the polarization state on the Poincaré sphere. As described above, the BSM is performed in a fiber-coupled beamsplitter, so that we can change the polarization state of light passing through the fibers by creating loops in a three-paddle polarization controller. Each paddle acts as a quarter-wave or half-wave plate depending on the number of fiber loops in it and the system is made up by a series of quarter/half/quarter-waveplate. By changing the orientation of the paddles we rotate the axis of the waveplate and we can, in principle, counteract any polarization rotation. The residual corrections, either in the QT setup or for compensating polarization effects after the X line is separated from the XX line (and avoid rotations between the two two-photon states), are corrected with the use of variable liquid crystal retarders.

3.3 Experimental results: photon-correlation analysis

The successful implementation of the entanglement(state) teleportation experiment relies on the detection of four(three)-fold coincidence events. In the entanglement teleportation, we need to measure the fidelity to $|\psi^-\rangle$ of the density matrix $\rho_{\mathrm{XX}_L,\mathrm{XX}_E}$ triggered by a BSM of $|\psi^-\rangle_{\mathrm{X}_E,\mathrm{X}_L}$ states, see Eq. 1.3. In the state teleportation instead, we prepare the polarization state of an X_L photon and measure the single-photon state of the XX_E photon triggered by the successful BSM of $|\psi^-\rangle_{\mathrm{X}_E,\mathrm{X}_L}$ to check if its polarization is teleported from the original one, except for a unitary transformation. By violating the classical limit in all the three unbiased polarization bases we can claim that the teleportation is non-classical.

3.3.1 State teleportation

The QD used in the state teleportation experiment belongs to the sample described in Section 2.1, featuring a FSS of 1.2(2) µeV and an entanglement fidelity to the $|\phi^+\rangle$ state $f = 0.925(3)$. The value of the raw indistinguishability, without considering imperfections from the setup and non-zero $g^{(2)}(0)$, is 0.65(2). In the experiment, all the time tags from the 3 detectors are registered. In the processing of the coincidences, we build an histogram of the arrival times of XX photons τ_2 with respect to the time distance $\Delta\tau_{10}$ of events in the two BSM detectors. The relative delays in the correlation electronics are tuned so that X photons that interfered at the BSM setup have $\Delta\tau_{10} \simeq 0$ and that the arrival times corresponding to the

teleported XX photon have $\tau_2 \simeq 0$. The double excitation of the QD every 1.8 ns will provide 12 possible time correlations peaks repeating every 12.5 ns, which is the repetition rate of the laser for this experiment.

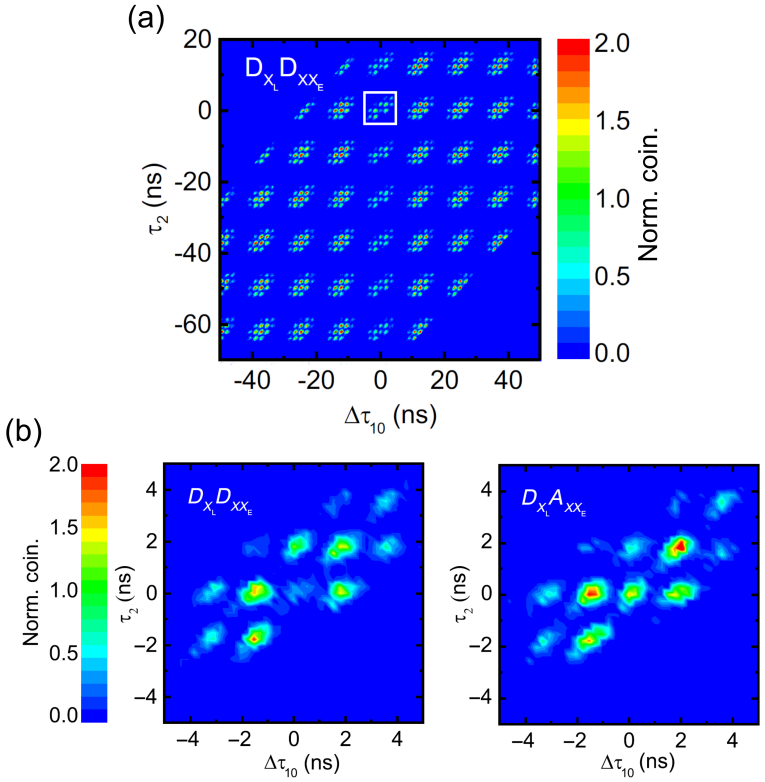

Figure 3.2. (a) Example of normalized third-order teleportation correlation between a teleported XX photon in the diagonal base (D_{XX_E}) triggered events at τ_2 and the BSM detectors relative delays $\Delta\tau_{10}$ relative to an input state in the same D basis (D_{X_L}), represented on large ($\tau > 40$ ns) time scales for an arbitrary QD measured. (b) Similar histograms as panel (a) but in a restricted time delay window ($\tau < 5$ ns) for a D-polarized X input state D_{X_L} and for co-polarized D_{XX_E} detection (left) and cross-polarized A_{XX_E} detection (right) of the XX photons. Adapted from Ref. [52].

In Fig. 3.2(a), we show the full histogram for a state preparation of $|\phi\rangle_{X_L} = |D\rangle$ and detection along the same D basis. The portion of the histograms for the QD of the experiment, centered around the peak corresponding to teleportation events, i.e., $\Delta\tau_{10} = \tau_2 = 0$ for co- and cross-polarized case, are shown in Fig. 3.2(b). We can calculate a second-order correlation histogram, see top graph of Fig. 3.3(a), by integrating the counts in the relevant peaks at $\Delta\tau_{10} = 0$ normalized to the counts of uncorrelated side peak coincidences, i.e., those corresponding to the equivalent peak at $|\Delta\tau_{10}| > 12.5$ ns. The fidelity of the teleportation, i.e., how similar is the teleported state to the original one, can be estimated from the normalized detection probabilities of the co- and cross-polarized (X_L, XX_E) third-order correlations in

each basis as

$$f_T = \frac{g_{\perp}^{(3)}}{g_{\perp}^{(3)} + g_{\parallel}^{(3)}} \tag{3.23}$$

The value for the fidelity is plotted for the diagonal polarization base in the bottom graph of Fig. 3.3(a). The resulting fidelity for the diagonal base yields a value as high as 78(3)%. We then performed the same calculations for the remaining two unbiased polarization bases, namely linear HV and circular RL. The results for all the three bases is above the classical limit set at 2/3 [131], corresponding to a classically polarization correlated photon cascade, showing non-classical correlations between the input photon and the teleported photon, see Fig. 3.3(b). The average fidelity is 75(2)%, which corresponds to the raw value obtained without temporal postselection on the relevant peaks, background subtraction, nor postprocessing of the measured data.

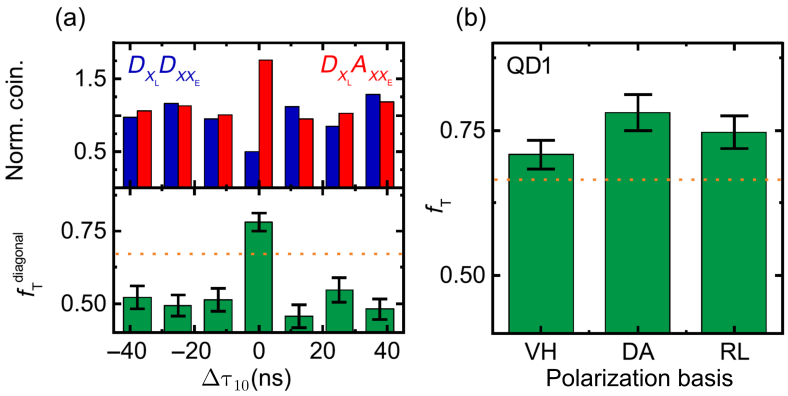

Figure 3.3. (a) Integrated coincidences for both detection bases around the $\Delta\tau_{10} = 0$, corresponding to a $|\psi^-\rangle$ in the BSM setup, normalized to the value of uncorrelated events at $|\Delta\tau_{10}| > 12.5\,\text{ns}$ (top) and the corresponding calculated teleportation fidelity, defined in Eq. 3.23 (bottom). (b) Teleportation fidelities for the full set of orthogonal input states. The classical limit of 2/3 is highlighted as a dashed orange line. Adapted from Ref. [52].

3.3.2 Entanglement teleportation

The QD used in the entanglement teleportation experiment features a low FSS of 0.6(5) µeV and a fidelity to the $|\phi^+\rangle$ Bell state of 0.88(2), for the light emitted. The indistinguishability of the photons is estimated from the HOM visibility, which is 0.63(2). To reduce the load of out-of-coincidence events from the data stream toward the computer, we combine the two channels of detection of X photons with an AND Boolean operator into a virtual single channel that clicks when a $|\psi^-\rangle$

BSM is detected, i.e., when both detectors click within a defined time window of 600 ps. The value assigned to the channel is that of the the latest time tag from two clicks. We tune the relative delay of the channels corresponding to the X detection so that the zero-time delay in their cross-correlation function corresponds to the simultaneous detection of X_E and X_L. The time window excludes coincidence events from photons that follow different optical paths and arrive at the BSM beam splitter with a larger delay. Due to the fast radiative lifetime of our sources (~ 250 ps), the BSM window does not perform any post-selection on the two-photon interference temporal pattern. This condition is of particular interest for real-life applications, where the efficiency of the protocol needs to be the highest possible to approach deterministic operation. All the four-fold coincidences detected at up to a 100 ns distance from a successful BSM are recorded.

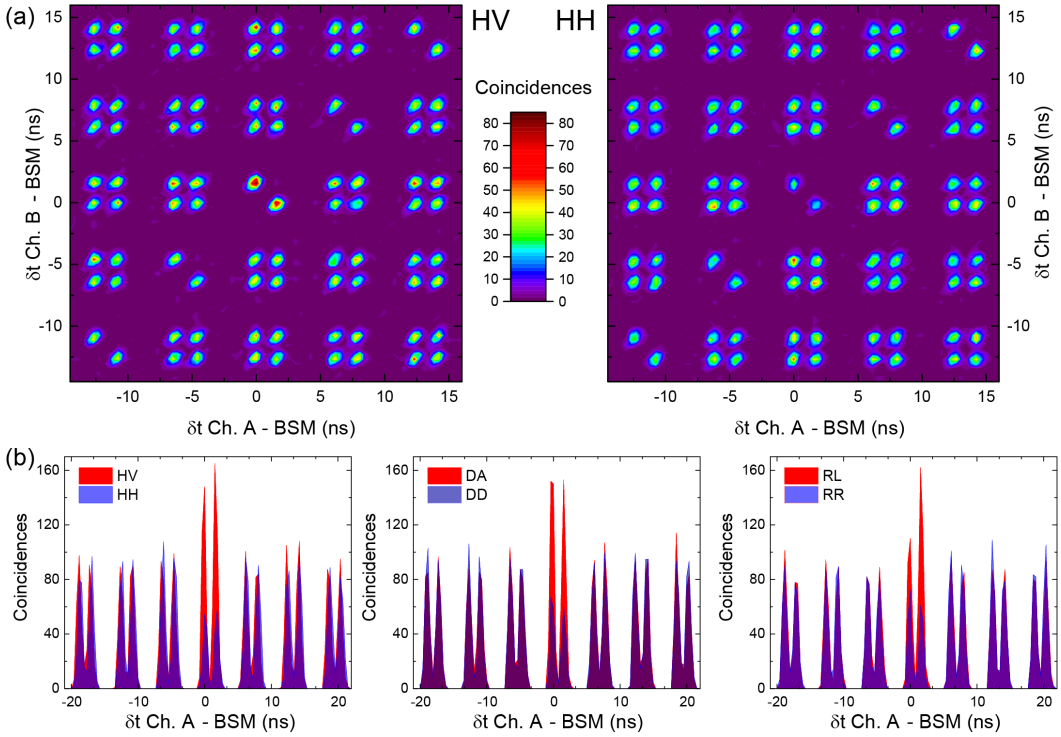

Figure 3.4. (a) Fourfold coincidences histograms as a function of the delays between the BSM and the XX detection events on the two tomography channels, recorded for cross- (left) and co-polarized (right) linear polarization. Peaks along the main diagonal would correspond to XX photons excited from the same laser pulse and are therefore absent due to the single photon purity of the QD. The two peaks at the center belong to events synchronized with a BSM and differ only on whether XX_E or XX_L is detected on channel A. Bunching for HV and antibunching for HH are observed, as expected for the $|\psi^-\rangle$ state. (b) Cross-correlation histograms between XX photons in linear, diagonal, and circular polarization bases. These data are reduced from the fourfold coincidences histograms as presented in panel (a) by binning over the time tags on channel B in the time window included between -1 and 2.8 ns. From Ref. [53].

The polarization optics in front of the detectors in the quantum tomography setup can perform different projective measurements on XX_E and XX_L in order to acquire coincidences in the set of polarization bases required for reconstructing the fidelity to the $|\psi^-\rangle$ state. The four-fold coincidences are recorded as a function of the delays between the BSM and the XX detection events in the two tomographic channels, as shown in Fig. 3.4(a) for a pair of co- and cross-polarized XX bases. The comparison between the two peaks near zero delay, which contains the fourfold coincidences of photons coming from two subsequent XX-X cascades, highlights the presence of polarization correlation.

In Fig. 3.4(b) the data are windowed and binned to obtain second-order intensity correlation histograms for the linear, diagonal, and circular polarization bases. The observed bunching and antibunching on orthogonal and parallel polarization bases respectively clearly show the presence of a swapping process with a projection to a state with a dominant $|\psi^-\rangle$ character.

To estimate the correlation visibility, the coincidence counts are normalized with respect to the side peaks stemming from XX photons uncorrelated with the BSM. Comparing the number of four-fold coincidences recorded for different polarization bases in the tomographic measurement requires to account for differences in the integration time or photon flux. The four-fold coincidence events that were triggered by XX photons that were not generated by the same cascade that generated the X photons that interfered in the BSM are used as a reference for normalization, since they are completely uncorrelated. We describe the normalization procedure in detail using a measurement in which the linear polarizers placed in front of the XX photon detectors are removed, and no correlation in the zero-time delay peaks is expected. Figure 3.5(a) shows the complete $g^{(3)}_{\delta A-BSM,\delta B-BSM}$ histogram relative to this measurement.

First, a time window of 1 ns is used to remove noise counts which arrive at unexpected time bins. Specifically, we only consider the peaks in the $g^{(3)}_{BSM,A,B}$ histogram at (0, 0), (0, 1.8), (1.8, 0), and (1.8, 1.8) ns, repeated with 6.25 ns periodicity, with a tolerance of ± 1 ns. Then a cross- correlation histogram $g^{(2)}_{A,B}(\delta_{A-BSM})$ is obtained by considering the two peaks centered at (0, 1.8) and (1.8, 0) ns, corresponding to the potential swapping events, and the uncorrelated ones described by the areas outside of the cross in Fig. 3.5(a). The coincidence counts are binned by summing all the events with a specific time tag δ_{A-BSM} from channel A and dividing the result by the number of peaks included in each bin. This procedure produces the $g^{(2)}_{A,B}$ histogram shown by the blue filled curve in Fig. 3.5(b). At this stage, the central and side peaks differ in intensity because of the value below unity of the fidelity of preparation of the XX-X cascade, which makes more likely to detect XX photons in

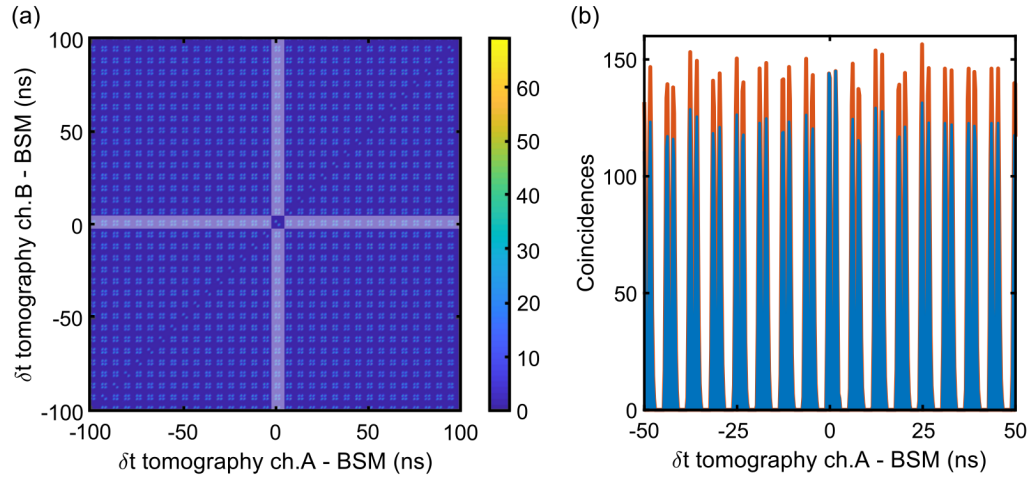

Figure 3.5. Four-fold coincidences histograms as a function of the delays between the BSM and the XX photons detected on channel A and B in absence of any polarizing optical element. The grayed-out areas correspond to events in which only one of the XX photons is synchronized with a BSM, excluded from the side peaks normalization. From Supporting Material of Ref. [53].

the central peak knowing that a linked pair of X photons has been generated.

In order to gain complete insight on the result of the swapping operation, we perform the full tomography of the two-photon state and collect XX_E-XX_L correlations in the 36 possible combinations of linear, diagonal, and circular polarization bases. A minimum of 16 separate measurements settings would be required for a two-qubit tomography but we preferred to employ a set of 36 measurements to have a higher precision at a fixed global acquisition time [132]. Note that XX_E and XX_L are defined by their time of arrival and not by the detector that registers them, therefore permuted pairs of bases are acquired at the same time, and the total number of measurements is reduced to 21. Once the coincidence counts are measured in all the polarization sets and normalized, a set of 16 measurement is used to analytically get an initial guess of the density matrix. Then a maximum likelihood estimation method, following the work of James *et al.* [61], is used to find the Hermitian density matrix which best complies with the complete set of 36 measurements, assuming that the statistics of the coincidence counts is described by independent normally distributed variables with a Poissonian standard deviation. The density matrix is presented in Fig. 3.6(a).

The raw value of fidelity to the expected Bell state $|\psi^-\rangle$ is calculated from the density matrix to be 0.58(4) using the standard formula:

$$f^{\psi^-}_{\mathrm{XX}_E,\mathrm{XX}_L} = \mathrm{Tr}\left[\rho_{\mathrm{XX}_E,\mathrm{XX}_L}\,|\psi^-\rangle\,\langle\psi^-|\right] \tag{3.24}$$

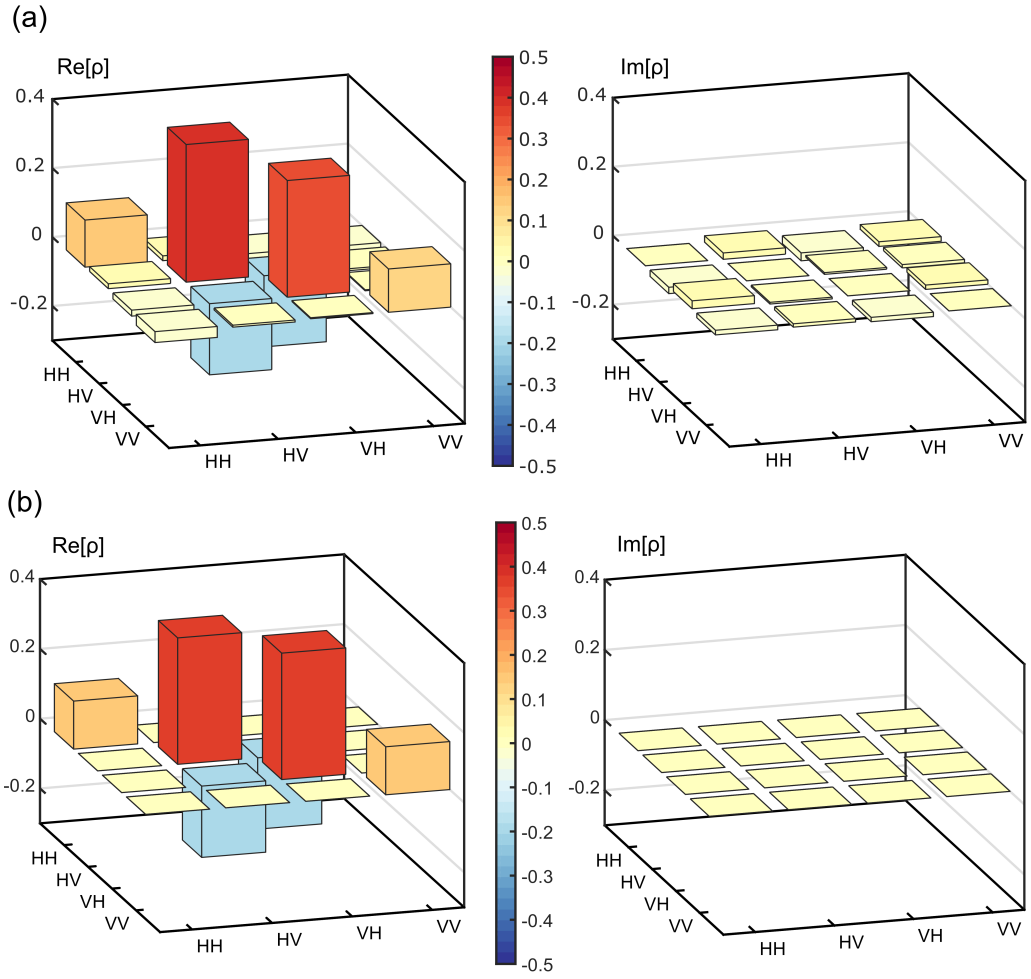

Figure 3.6. (a) Real and imaginary part of the two-photon density matrix reconstructed from measurements that probe the polarization state of the XX photons selected in conjunction with a BSM on their entangled partners. The matrix refers to a QD with FSS equal to 0.6(5) μeV and HOM visibility of 0.63(2). (b) Simulated real and imaginary part of the density matrix, calculated using Eq. 3.18 and the measured values of the QD properties of emission.

This value indicates a strong correlation between photons that are uncorrelated without the information from the BSM (0.25), surpassing the classical threshold of 0.5 [133] by 2 standard deviations. A consistent evidence of the presence of entanglement is offered by the above-zero raw value of the concurrence, 0.15(8), which measures the quantum coherence properties of a mixed quantum state [134] and is defined as:

$$C(\rho) = \max(0, \sqrt{\lambda_1} - \sqrt{\lambda_2} - \sqrt{\lambda_3} - \sqrt{\lambda_4}) \tag{3.25}$$

where λ_i are the eigenvalues of the following matrix numbered in decreasing order :

$$R = \rho\Sigma\rho^T\Sigma \tag{3.26}$$

and Σ is the spin flip matrix:

$$\Sigma = \begin{pmatrix} 0 & 0 & 0 & -1 \\ 0 & 0 & 1 & 0 \\ 0 & 1 & 0 & 0 \\ -1 & 0 & 0 & 0 \end{pmatrix} \tag{3.27}$$

To estimate the error of the physical quantities calculated from the density matrix we used a Monte Carlo approach. For each correlation measurement, possible data inputs are randomly generated from a Poissonian distribution whose average is the measured value of coincidence counts. This procedure is iterated 2000 times to obtain a large enough sampling for consistent results. The density matrix, together with the related physical quantities of interest, namely the Bell-state fidelity and the concurrence, is calculated for each set of simulated entries. The standard deviation of the obtained outcomes gives our error estimate.

The above result shows that the state of the two XX photons, which were previously uncorrelated, is now entangled in polarization, with the same Bell state as the measured X photons belonging the the respective entangled two-photon cascade. This result proves a successful teleportation of the entanglement onto an uncorrelated photon pair, the basic operation of a quantum repeater. The novelty of the results resides in the fact that the entangled light source comes from a quantum emitter with with sub-Poissonian statistics. The intrinsic difference from the SPDC sources opens the way to future implementations of real-life quantum repeaters for quantum networks, at least regarding the source of quantum entangled light. It is worth emphasizing that the measured level of entanglement between the swapped photons does not consider imperfections stemming from the experimental setup, such as background light and non-ideal beam splitters.

A value of 0.64 for the fidelity would be estimated by taking into account the imperfections in the BSM setup, namely the mode overlap of the BS ($1 - \epsilon = 0.96(1)$), its reflectance $R = 0.48(5)$ and transmittance $T = 0.52(5)$ and the residual multi-photon emission $g_{\mathrm{X}}^{(2)}(0) = 0.017(2)$.

3.4 Model and data comparison

We now make use of the theory we reported in Section 3.1, to first simulate the results of the entanglement teleportation experiment, and then to address the

magnitudes of the effects that the several characteristics of semiconductor QDs have on the outcome of the protocol. We reproduce the density matrix from the values of the QD used for the experiment with the use of Eq. 3.18. We collect the values of $g^{(2)}_{\mathrm{X}}(0)$, S, τ_X, and V by direct measurements. By considering the typical values of the decoherence times τ_{HV}, τ_{SS}, and T_2^*, whose effect is already almost completely empirically included in V we see that their contribution to the entanglement teleportation fidelity is negligible within the error bars. For the calculations we adopt the values from the literature and we consider negligible the value of the cross dephasing, and we take the value for the spin-scattering time $\tau_S = 14\,\mathrm{ns}$ [42] and a pure dephasing time twice the radiative lifetime [48]. The simulated density matrix is plotted in Fig. 3.6(b), below the experimental matrix, showing clearly how the main features of the density matrix are reproduced. To make the comparison more quantitative we can extract the analytic expression of the fidelity from the model matrix in Eq. 3.18:

$$f^{\psi^-}_{\mathrm{XX}_E,\mathrm{XX}_L} = \frac{1}{4}\left(1 + \frac{V}{2-V}k^2\left(g^{,(1)2}_{H,V} + 2\frac{g^{(1)2}_{H,V}}{1+\left(\frac{S\tau_{\mathrm{X}}}{\hbar}g^{(1)}_{H,V}\right)^2}\frac{1}{1+\left(\frac{S\tau_{\mathrm{X}}}{\hbar}g^{(1)}_{deph}\right)^2}\right)\right) \tag{3.28}$$

we can evaluate all the quantities appearing in Eq. 3.28 and give a numerical estimate for the fidelity $f^{\psi^-}_{\mathrm{XX}_E,\mathrm{XX}_L}$ without fitting any parameter. Our model returns a value of 0.56 which is in excellent agreement with the value of 0.58(4) obtained from the experiment. The model also indicates that the main limitations to the teleportation fidelity reside in the source and are due to HOM visibility and FSS, while also quantitatively describing the dependence on these parameters.

The results from the model are plotted in Fig. 3.7. Here the entanglement fidelity of the swapped state is reported in a contour plot versus the HOM visibility and the FSS of the QD. The y-axis is the FSS normalized to the value of the exciton lifetime τ_{X}. Indeed, a very short τ_{X} relaxes the requests for an ultra-small FSS, so that in the graph we can see the net effect of the time evolution introduced by the anisotropies in the QD, see Eq. 1.37. The model highlights how the reduced HOM visibility strongly affects the results: if $V < 0.5$ even at zero FSS the QD cannot surpass the classical limit of 0.5. From the model we can also see what are the requests for a test of non-locality with a Bell inequality violation. In particular, we can extract the amount of Bell violation from the matrix of the swapped photons and plot the limit of the Bell violation on the same graph [135]. This quantity is particularly important in the implementation of some entanglement-based quantum key distribution protocols, which rely on the consistent violation of the Bell inequality for the security of the

key exchange.

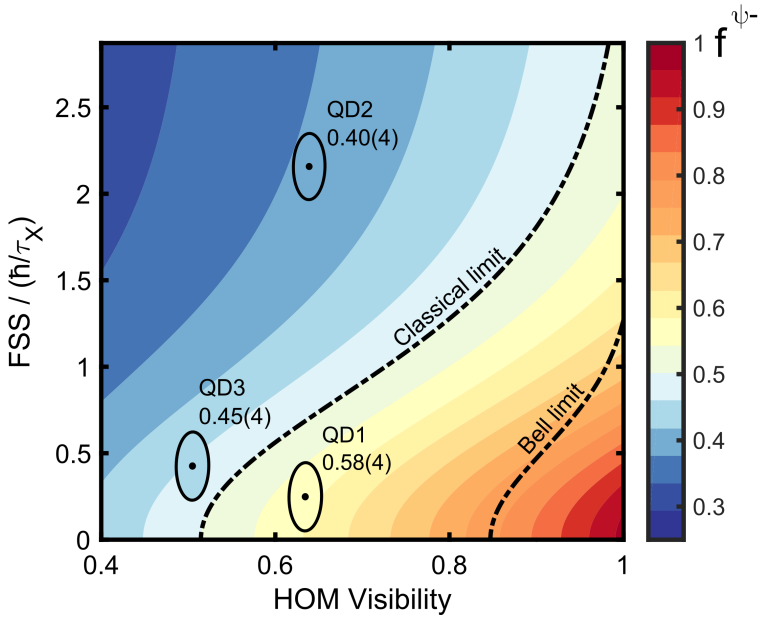

Figure 3.7. Contour plot of the fidelity of the entanglement teleportation as a function of HOM visibility and the ratio between FSS and X radiative lifetime τ_X as expected from the model reported in Eq. 3.18 for a 25% BSM. The classical limit, as well as the threshold for Bell's inequality, is indicated with a dash-dot line. Experimental values for the three QDs analyzed in the experiment are plotted together with the experimental value of fidelity, which shows excellent agreement with the theory. Adapted from Ref. [53].

To test the model further we decided to repeat the experiment with two more QDs that are selected to have either a larger FSS (QD2 of Fig. 3.7 with $S = 5.9(5)$ µeV) or a lower visibility (QD3 of Fig. 3.7 with $V = 0.51(2)$) with respect to their successful peer. We then simulate their results with the model. The two QDs do not overcome the classical limit, confirming again the stringent requirements for the success of this experiment. The experimental values for the fidelity are 0.40(4) for QD2 and 0.45(4) for QD3. The results from these two QDs are shown in the contour plot of Fig. 3.7. The value of the fidelity is given in the same color scale as the simulation and the chromatic agreement with the area in the graph suggests that the simulated results agree well with the experimental values.

We can confirm the predictions on how the different imperfections of the QD affect the final density matrix in Eq. 3.18 by comparing the experimental matrices of the three QDs investigated in the experiment. As we can see in Fig. 3.8(a), a QD with a lower visibility will produce BSMs with a reduced capability of telling apart the different Bell state going toward a random behavior, so that the matrix of the swapped photons will be more similar to a mixed, diagonal state. The effect of a

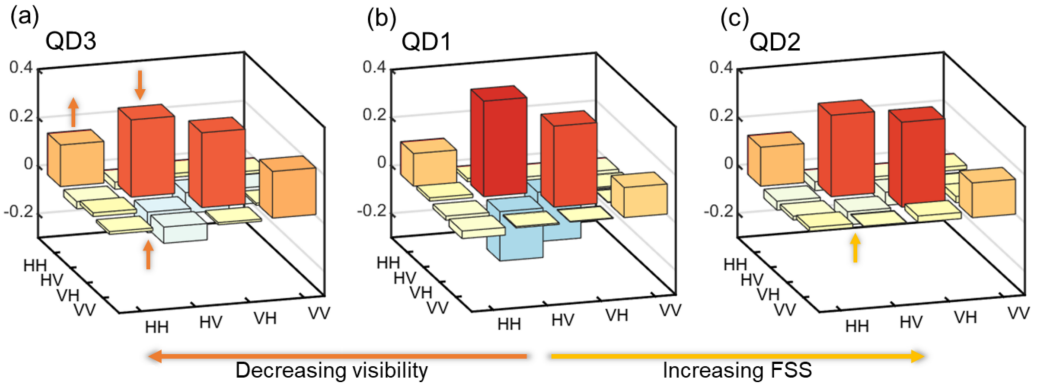

Figure 3.8. Real part of the matrices of the swapped entangled states for the three QDs tested in the experiment. The arrows highlights the main effects in the matrix elements due to the imperfections in the source. (a) QD with $S = 1.0\,\mu\text{eV}$ and $V = 0.51$ (b) QD which allowed the the successful entanglement teleportation with $S = 0.6\,\mu\text{eV}$ and $V = 0.63$ (c) QD with $S = 5.9\,\mu\text{eV}$ and $V = 0.64$

high FSS is to mix only $|\psi^-\rangle$ and $|\psi^+\rangle$, see Eq. 1.37. The result for a QD with a high FSS, see panel (c) of Fig. 3.8, will then be a state with the out of diagonal components strongly reduced in magnitude.

A simple way to alleviate the effects of the low HOM visibility, is to increase the number of Bell states which can be detected in the BSM setup. As explained in Section 1.2.3, by adding at every output port of the beamsplitter in the BSM a polarizing beamsplitter and two detectors, see Fig. 1.5, we can tell apart the $|\psi^+\rangle$ state, which has symmetric spatial wavefunction, but orthogonal linear polarization of the two photons of the state. By introducing the polarization discrimination we are removing accidental double-clicks coming from co-polarized Bell states, i.e., $|\phi^\pm\rangle$. The simulated matrix for this case was given in Eq. 3.19. The QD1, which performed a successful entanglement teleportation, would have been pushed above the Bell limit with a 50% BSM setup, with a simulated value of 0.76 for the swapped state, see Fig. 3.9.

As a last exercise, we can feed the model the best values we can find in literature in terms of indistinguishability and FSS. For the indistinguishability, we select the high value of 0.9 obtained recently in the CBR structures of Ref. [39]. The results from strain-tuned QD samples [42] leading to an entanglement fidelity of the X-XX pair of 0.98. The (theoretical) combination of the two separate results is highlighted as a star in the plots of Fig. 3.9 pushing the protocol fidelity to values above 0.9.

3.4.1 The importance of extraction efficiency

We now provide an estimation of the count rates in the entanglement teleportation experiment. The repetition rate of the double pulse ν_{laser} is reduced by the

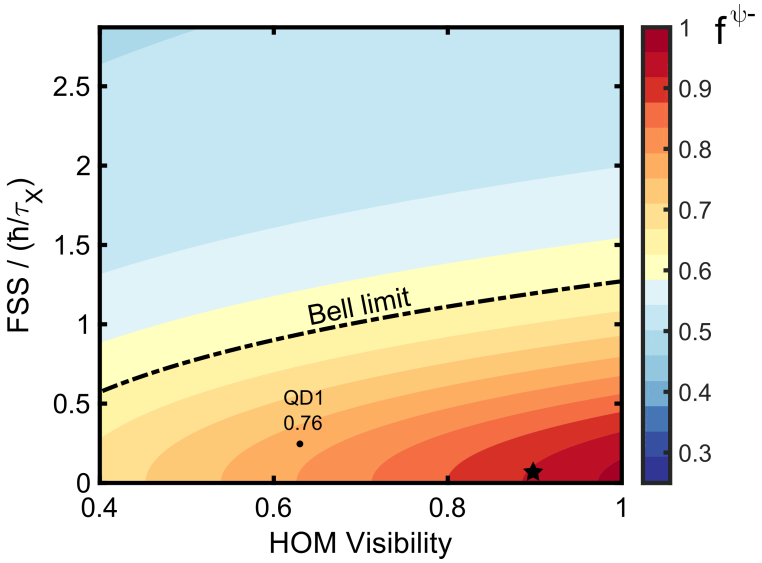

Figure 3.9. Contour plot of the fidelity of the entanglement teleportation as a function of HOM visibility and the ratio between FSS and X radiative lifetime as expected from the model reported in Eq. 3.19 for a 50% BSM. The dot indicates the simulated value of QD1 with the improved setup. The theoretical value obtained by using an ideal QD combining state-of-the-art features from Refs. [42] and [39] is indicated with a star. Courtesy of Dr. F. Basso Basset.

telegraphic blinking rate η_{blink}. Due to the below unity preparation fidelity, not all the laser pulses excite the XX even when the QD is optically active, this effect is taken into account in the excitation efficiency term η^2_{prep} (on both the photons pairs). We can combine the overall efficiency of the setup and the extraction efficiency from the QD sample, which we name η_{coll}, together with the photon detection probability of the avalanche photodiodes η_{det} to get the experimental efficiency $\eta_{exp} = \eta_{coll} \cdot \eta_{det}$, which enters the calculation with a fourth power. The last terms we need to add are the intrinsic losses due to the setup design, i.e., the three beamsplitters (1/8) and the two non-ideal polarizers ($\eta^2_{pol}/4$), and the efficiency of the single state BSM ($(1 - V/2)/2$). The entanglement teleportation coincidences rate is then:

$$\eta_{ET} = \nu_{laser} \cdot \eta_{blink} \cdot \eta^2_{prep} \cdot \eta^4_{exp} \cdot \frac{\eta^2_{pol}}{4} \cdot \frac{1}{8} \cdot \frac{1 - V/2}{2} \tag{3.29}$$

For the state teleportation experiment instead, the count rate using a single quantum emitter increases by a factor $(\frac{1}{2}\eta_{exp} \cdot \frac{\eta_{pol}}{2})^{-1}$. The experimental fourfold (threefold) coincidences rate is approximately $\nu_{ET} = 2.5\,\text{mHz}$ ($\nu_{ST} = 80\,\text{mHz}$) resulting in an integration time of roughly 18 h (40 min) for each base of the quantum tomography to gain a statistically relevant number of counts. A possible improvement in the efficiency of the setup would be to double the number of detectors and using

polarizing beamsplitters to erase the contribution of $\eta_{pol}^2/4$ and increasing the BSM efficiency from 1/4 to 1/2. When moving to an experiment with remote sources the term introduced by the beamsplitters will be erased but other issues may arise, like non-synchronized blinking.

3.4.2 State teleportation with imperfect quantum dots

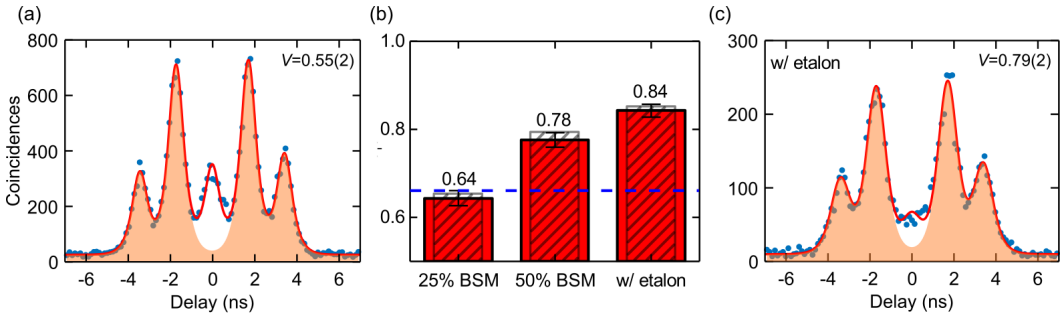

Figure 3.10. (a) Intensity correlation histogram (blue dots) for an HOM experiment for X photons from a QD with low interference visibility (0.55(2)). The value is obtained by fitting the data with the sum of five Gaussians convoluted to an exponential decay (red line), with a fixed FWHM. (b) Comparison of the average teleportation fidelity for a state teleportation experiment performed in a setup with a 25% BSM, a 50% BSM, and a 50% BSM and X photons transmitted through an etalon filter. The red filled bars represent the experimental values, including error bars, the gray striped bars are the values simulated based on the physical properties of the source. The blue dashed line represents the classical limit.(c) Intensity correlation histogram (blue dots) for an HOM experiment for X photons from the same QD as in (a) transmitted through a 1.28 GHz etalon filter. The interference visibility is improved by the spectral filtering up to a value of 0.79(2). Adapted from Ref. [93].

To follow up on the idea of improving the experimental setup to partially counteract source imperfections, we demonstrate a state teleportation experiment using light from a QD with sub-par values of entanglement and photon indistinguishability by introducing a polarization selective 50% BSM and spectral post-selection [93].

The HOM visibility of the QD selected for this experiment is $V = 0.55$, which is lower then the mean value of 0.65 commonly reported for this kind of source [48], see Fig. 3.10(a). The fidelity to the $|\phi^+\rangle$ state is 0.89(1), a value which is mainly limited by a finite FSS of the X states of 1.8(50) μeV.

The state teleportation experiment is first performed with the same experimental setup described in Section 3.2, i.e., by using a 25% BSM setup detecting only $|\psi^-\rangle$ states. The average teleportation fidelity for this experiment is 0.644(17), a value that does not surpass the classical limit of 2/3, see left bar of Fig. 3.10(b). The value of the teleportation fidelity is also simulated from the properties of the source using the theoretical model we introduced in Section 3.1.2 and is reported in the

same graph as a gray shaded area. The predicted value is within the error bar of the experimental value, confirming the power of the theory we developed.

The first optimization step is to introduce in the setup a 50% efficiency BSM, see Fig. 1.5. The introduction of polarizing beamsplitters in the BSM setup allows not only for this setup to distinguish the Bell state using photon indistinguishability but also relying on the polarization state of the photons by effectively removing spurious events from $|\phi^+\rangle$ and $|\phi^-\rangle$ states, as discussed in detail at the end of Section 3.1.1. The average value of the teleportation fidelity for this improved setup is pushed at 0.776(16), see central bar of Fig. 3.10(b), which is now above the classical limit.

The theory we developed for simulating the entanglement teleportation results pointed at the HOM visibility V as one of the main limiting factors of the fidelity of the entanglement protocols. It is then worth trying to push it up to higher values. For example, the photon indistinguishability can be improved by using spectral filtering at the expenses of source brightness. In the experiment we introduce an air-spaced etalon filter with a bandwidth of 1.28 GHz corresponding to 5.47 µeV before the BSM setup. The relatively large spectral diffusion of the chosen QD, with an X linewidth of 118 µeV, results in a reduction of a factor 10 of the X emission line photon counts. This strong reduction stems from the exceptionally large emission linewidth of this particular QD. Tests performed on Fourier-limited emission from other QDs showed a reduction of a factor 4 of the photon counts. The HOM visibility from photons emitted by two consecutive laser pulses is increased to 0.79(2), see Fig. 3.10(c), despite the modest selectivity of the filtering. This results in a value of the teleportation fidelity increased to 0.842(14), see right bar of Fig. 3.10(b). It is interesting to mention that this value would already allow to use this QD as a quantum-light source in an error resistant quantum key distribution scheme [136].

The results summarized in this Section shows how we can recover a high fidelity of the state teleportation protocol starting using a photon source with less-than-ideal figures of merit, providing us with another powerful tool toward the implementation of real life quantum networks.

Chapter 4

Toward an ideal source of entangled photons

The results we have shown in the previous Chapter represent an important milestone in the way toward the demonstration of a quantum network based on solid-state emitters. Still, we made clear what is still missing to upgrade quantum protocols with QDs from proof-of-principle demonstrations to real-life technologies. An entangled-light source based on QDs should excell in terms of brightness, indistinguishability, and degree of entanglement to be considered a serious alternative in commercial systems. In this Chapter we will describe our approach to improve the properties of our quantum light source.

4.1 Tackling current limitations

Quantum dots feature intrinsic properties which make them extremely promising candidates as future quantum light sources. Differently from SPDCs sources, QDs are truly sub-Poissonian sources of non-classical light. They can be modeled as two-level systems, with fast recombination times, emitting single and entangled photons with ultra low multi-photon emission. The high preparation fidelity of the states that can be achieved via properly designed excitation schemes tells us that they have the potential to be on-demand photon sources. Yet, entangled photon sources need to be improved for their employment in the construction of quantum networks. As mentioned before, placing the emitter in an optical cavity is one of the best and most pursued way to overcome current limitations for QDs. An ideal cavity for QDs would need to fulfill a list of characteristics to be suitable for the entangled light generation: i) We need a broadband resonance to accommodate both the photons of the entangled pair, which are emitted by the QD at different energies; ii) We need a Purcell enhancement of the transition rates in order to increase the

indistinguishability of the emitted photons; iii) We need a cavity which funnels most of the light emitted from the QD out of the semiconductor host material, in a near-Gaussian beam with low divergence; iv) Finally, we want the whole cavity design to be compatible with the well-developed strain tuning technology, which allows for adjustments of the emission wavelength, and independently, the erasure of FSS. Among the several and different solutions presented in literature, one in particular caught our attention. Circular Bragg resonators (CBRs) promise a relatively easy fabrication, a simulated high-extraction efficiency, a broadband cavity with modest Purcell enhancement, and a technology which, according to the authors, "is fully compatible with state-of-the-art piezoelectric-based tuning methods" [39].

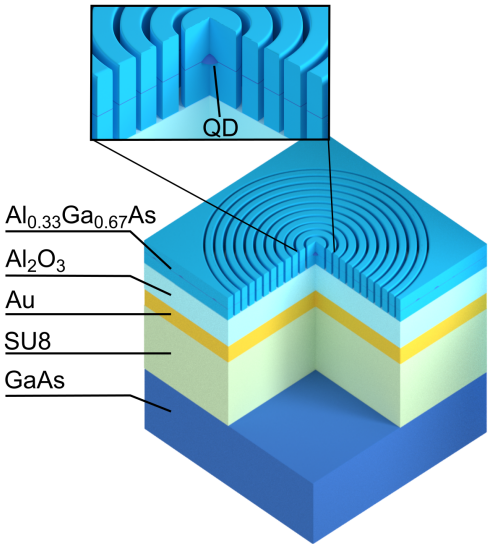

Figure 4.1. Sketch of the circular Bragg grating cavity (CBR), the z-axis is expanded to better distinguish the layers that constitutes the whole structure. The QD is sitting in the geometrical center of a cylindrical cavity (see magnification in the inset). A circular Bragg grating is etched around the cylindrical cavity. The period and duty cycle of the grating are tuned so that light traveling through the grating is reflected out of plane. Below the cavity, a broadband mirror constituted by a Au mirror separated by an oxide layer reflects the light leaking downwards back into the cavity.

In this Chapter we will describe our efforts toward the fabrication of strain-tunable QDs embedded in CBRs structures. The work is the result of a broad collaboration between three universities and a research center, coordinated and followed in first person by the author. The fabrication of the structures starts in the Institute of Semiconductor and Solid-State Physics of the Johannes Kepler University of Linz (AT) and continues in the clean rooms of the Institute of Photonics and Nanotechnologies of the National Research Council of Rome (IT) and the Technical Physics Institute of the Julius Maximilian Würzburg University (DE). The optical

characterization of the samples and the quantum optics experiments are performed in the laboratory of the Nanophotonics group at the Physics Department in Sapienza University of Rome (IT).

4.1.1 Circular Bragg resonators on piezoelectric actuators

As mentioned in Chapter 2, a CBR combines in its design three different elements, namely: a central cylindrical cavity, a circular Bragg grating, and a metallic mirror. It is not easy to separate the single contributions of the three parts, since the final result stems from the interplay between them. Still, we can distinguish the main role of every single part in the final outcome. Looking at Fig. 4.1, we can distinguish the three elements: i) The core of the cavity is a single QD sitting in the geometrical center of a cylindrical cavity, etched in the semiconductor membrane. ii) a circular Bragg grating surrounding the cavity constituted by 10 concentric rings etched in the same membrane. The periodicity of the grating matches the second order condition $\Lambda = \lambda/n_{eff}$ where n_{eff} is the mean n determined by the duty cycle of the grating and λ is the wavelength of the light traveling in the grating. The second order condition [117, 137] and the circular shape of the grating produces out-of-plane reflections of the light emitted by the QD in the center inside the semiconductor. By carefully tuning the grating periodicity the light can come out of the cavity in a nearly-Gaussian beam with a low-divergence; iii) below the structure is placed a highly efficient broadband reflector (HBR), consisting of a metal mirror separated from the semiconductor by an oxide layer to avoid plasmonic coupling, reflecting the light leaking downwards back into the cavity. The resonance wavelength, the quality factor, and the Purcell enhancement all depend, with different magnitudes, on the parameters of each of the three parts constituting the CBR.

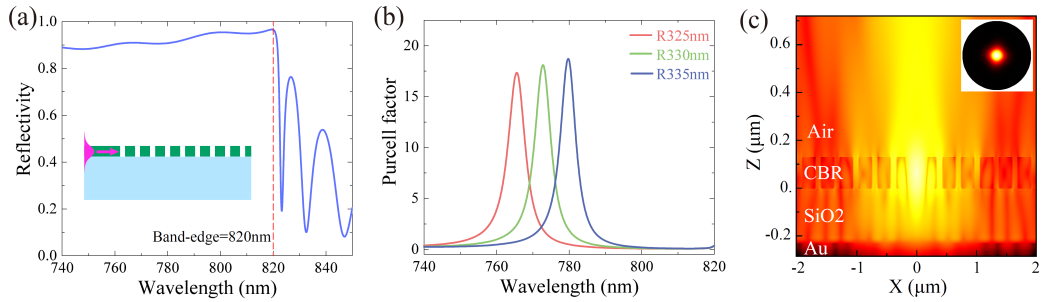

Figure 4.2. Simulation steps for the design of the circular Bragg resonator with an SiO_2 layer. (a) Simulated reflection band of the 1D Bragg grating structure. (b) Purcell factors for the CBRs with different cavity radii. (c) The XZ cross-section of the simulated electric field distribution in the CBR. Inset is the calculated far-field pattern. From Supplemental Materials of Ref. [39].

To simulate the photonic structure and optimize its design, Liu *et al.* [39] used finite difference time domain (FDTD) simulations to model the electric field distribution in the materials, see Fig. 4.2. First, the grating period and duty cycle is optimized by running a 2D simulation of the grating profile etched in the semiconductor slab (140 nm thick $Al_{0.33}Ga_{0.67}As$) and sitting on an infinite substrate of silica (SiO_2). The light emitted by the QD is simulated as a TE mode launched from one side of the grating, see inset of Fig. 4.2(a). The power reflected from the grating is plotted as a function of the wavelength. Here, the grating parameters are optimized so that the band-edge of the grating is above the QD typical emission wavelength. After having identified the band-edge with the 2D model, they ran a 3D simulation of the whole resonator, sitting on an infinitely thick oxide layer, varying the diameter of the central cavity, to tune the correct wavelength of the cavity resonance, see Fig 4.2(b). The last step was to add a Au layer underneath the oxide and tune the oxide thickness so that the photons leaking downwards are backreflected in phase into the CBR. The resulting emission is shown in Fig 4.2(c). Here we can see how most of the photons are guided upwards with a small divergence angle, as confirmed by the far field pattern in the inset of the same sub-figure.

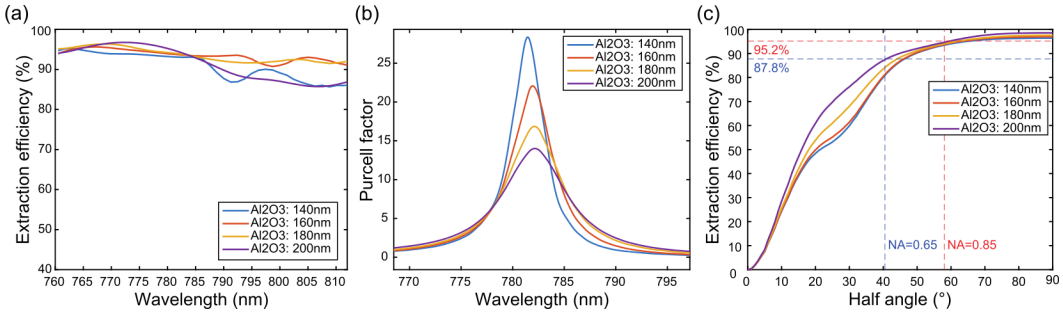

Figure 4.3. Simulation of the CBR design for different choices of Al_2O_3 layer thickness. (a) Extraction efficiency of the cavity versus wavelength for NA=1, varying the Al_2O_3 layer thickness. (b) Purcell factor vs wavelength, at various Al_2O_3 thicknesses. (c) Extraction efficiency vs acceptance angle of a microscope objective for the wavelength corresponding to the peak of the Purcell factor. The angles corresponding to a NA of 0.5 and 0.85 are sketched on the graph. The final choice for the Al_2O_3 thickness is 160 nm. Courtesy of Dr. S. Manna.

In our case, to adapt to a different choice of oxide, a similar set of simulations was performed by Dr. S. Manna at Linz University and confirmed by the author with similar parameters. Using the Lumerical software for the FDTD simulations, different thicknesses for aluminum oxide (Al_2O_3) were tested, see Fig. 4.3. The final choice of thickness for our structures was 160 nm, giving a good compromise between a flat extraction efficiency, see Fig. 4.3(a), and a relatively high Purcell factor (20 at the peak of the resonance), see Fig. 4.3(b). The simulated extraction efficiency for the central wavelength through a microscope objective with a NA of 0.85 is 95.2%,

Table 4.1. Design parameters for the CBR gratings with Al_2O_3 oxide.

Membrane height	Grating period	Trench width	Numbers of Rings	Oxide height
140 nm	330 nm	90 nm	10	160 nm

see Fig. 4.3(c). The final design for our structures is summarized in Table 4.1.

As mentioned above, a single QD must be sitting in the center of the cavity. Since QDs fabricated via droplet etching epitaxy are randomly placed on the surface of the sample, we need a way to map their position (and emission spectrum) within tens of nanometers precision and an equally precise method to deterministically fabricate the cavities around the selected QDs. The precision of the position of the QD in the cavity is extremely important to couple the emission in the right modes, as a deviation in the QD position from the center leads to a prominent enhancement of one polarization with respect to the other, resulting in a polarized emission [138]. Standard lithographic methods which uses accelerated electron beams fulfill this precision requirement, so we just need to build a system to acquire the position of single QDs with same or better precision. The proposed method is to use a PL imaging system working at cryogenics temperatures [139, 140], collecting high-resolution images of the QD emission and reference markers. The images are then analyzed with a computer program and the position with respect to markers is obtained, with a precision down to the tens of nanometers, see Section 4.2.2.

4.2 Fabrication of circular Bragg resonators

The fabrication of real cavities involves several steps starting from the as-grown QD sample to create semiconductor membranes, bond them on piezoelectric actuators, measure the positions of QDs and ending with the final etching of the cavities. Part of the fabrication procedure was inherited from the users and technicians of the cleanroom and then developed and optimized by the author to improve the sample quality and increase the fabrication throughput.

4.2.1 Semiconductor membrane preparation

The GaAs QD sample for the processing of CBR structures is grown by Dr. S. F. Covre Da Silva in the III-V MBE facility of the Linz University. The sample design is shown in detail in Fig. 4.4(a). The QDs are grown on a 70 nm thick slab of $Al_{0.33}Ga_{0.67}As$ with Al droplet etching. The QD layer is capped by another 69 nm layer of $Al_{0.33}Ga_{0.67}As$ for a total thickness of 140 nm. The slab is capped on both faces by a 4 nm layer of GaAs to prevent oxidation of the AlGaAs layer, and sits on

top of an Al-rich ($Al_{0.75}Ga_{0.25}As$) 400 nm sacrificial layer that separates it from the commercial GaAs wafer substrate (350 µm thickness).

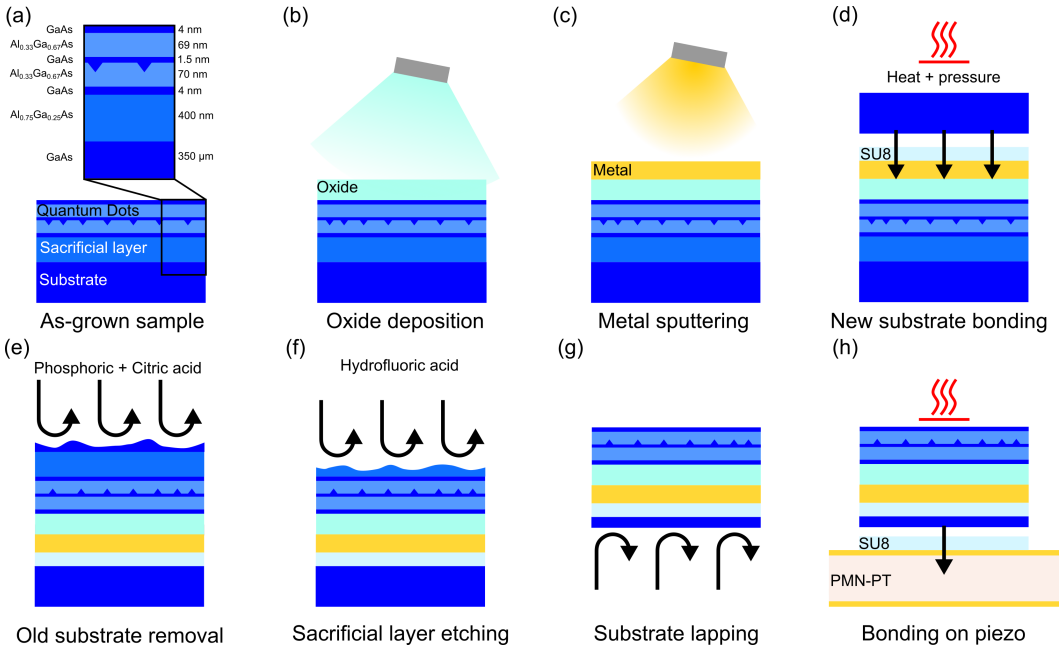

Figure 4.4. Scheme of the processing steps to fabricate a quantum dot membrane. (a) The QD sample wafer as grown from the molecular beam epitaxy machine. The substrate is a commercial GaAs wafer 350 µm thick, on top of it sits an Al-rich sacrificial AlGaAs layer. The AlGaAs membrane containing the GaAs QDs is capped by two thin layers of GaAs on both sides. (b) The sample receives an oxide layer by atomic layer deposition (ALD). (c) A metallic layer is grown on top of the oxide with thermal evaporation. (d) The sample is bonded to a new GaAs substrate using SU-8 photoresist. The bonding is made irreversible by applying both pressure and heat. (e) The sample is flipped and the original substrate is removed with a two-step wet etching using a non-selective orthophosphoric acid and hydrogen peroxide solution first and then a selective etching with a solution of citric acid and hydrogen peroxide (see text for proportions). (f) The Al-rich sacrificial layer is removed with hydrofluoric acid. (g) the new substrate is thinned down to ~ 50 µm with a lapping machine. (h) The micrometric thick stack is glued to the six-legged actuator with SU-8 photoresist and the application of heat.

Deposition of oxide and metal mirror

The design of the CBR-HBR needs the fabrication of a broadband reflector on one side of the semiconductor membrane. We then cut the sample from the MBE in 3 mm × 3 mm pieces ready to receive the oxide layer. Our first tests are run with SiO_2 deposited with electron beam evaporation. The membranes featuring SiO_2 grown with this technique are extremely prone to breaking due to degassing of the oxide when increasing the temperature of the sample. We then decided to switch to an atomic layer deposition (ALD) machine (Cambridge NanoTech Savannah 100) for the deposition of an Al_2O_3 layer. Here, subsequent pulses of gaseous precursors

(H_2O and $Al(CH_3)_3$ for the growth of Al_2O_3) react on the surface of the sample and create, in ideal conditions, an atomic-thick layer-by-layer growth of the oxide, see Fig 4.4(b). The oxide grown with the ALD features a high purity but the process is extremely slow and should be resorted only for the growth of thin oxides. With a growth rate of 1 Å per cycle, the desired 160 nm thick layer takes 1600 cycles, corresponding to a growth duration of 7.5 h.

The next step is the deposition of a Au reflective layer on top of the oxide, see Fig. 4.4(c). The metal layer is obtained by physical vapor deposition in the high vacuum of the deposition chamber of a Balzers-Pfeiffer PLS 570, by heating the metal in a crucible via the application of high voltages and sputtering it on the surface of the sample. The Au layer thickness is > 100 nm to ensure complete reflection of light. To aid the adhesion of the metal to the oxide, a 5 nm layer of Cr is grown between the oxide and the metal layer by electron-beam evaporation in the same machine.

After the mirror is completed, we need to flip the stack and free the QD membrane from the original substrate. To do so, we first bond it to a new GaAs substrate on the mirror side. The bonding, see Fig. 4.4(d), is performed in a Finetech Fineplacer bonder with the application of heat and pressure between the two samples. The presence of two cameras and a mechanical arm with a sucking plate allows for the precise alignment of the head and target pieces. As a glue for the bonding, we employ SU-8 2 photoresist, known in the field for the strong mechanical properties when cured above 250 °C. The photoresist is brushed instead of being spin-coated on the sample, due to its reduced dimensions, which prevent the formation of a uniform layer when spin-coating. After application of the glue, the new substrate is pressed on top of the sample while ramping up the temperature of the stack. The sample is then cooled down and is ready for the wet-etching steps.

Membrane wet etching

The stack is flipped and temporarily glued to a Si carrier with its sides protected with a photoresist, which is easily removable with an acetone bath but offers protection against acid etching. We then proceed to remove the original substrate and sacrificial layer with a three-step wet-etching. First, the 350 µm thick GaAs substrate is thinned down in a solution of orthophosphoric acid and hydrogen peroxide (3:7 ratio between 85% othophosphoric acid and 30% hydrogen peroxide). When roughly 50 µm of the GaAs substrate are left, we switch to a more selective acid solution, namely citric acid. By choosing the right ratio of citric acid and hydrogen peroxide (4:1 ratio between 50% monohydrate citric acid and 30% hydrogen peroxide) we can reach different etching speeds between the GaAs of the substrate and the

Al-rich sacrificial layer [141], using the latter as a stopping layer for the etching process, see Fig. 4.4(e).

The sacrificial layer is finally removed with hydrofluoric acid, at 10% concentration, see Fig. 4.4(f). This acid dissolves rapidly the Al-rich layer (order of seconds) and stops at the GaAs capping layer protecting the QDs membrane. The membrane at this stage appears of a bright pink color when illuminated under a white light, due to light interference in the stack, shifting to pale green when looked at an angle.

It is important to remark here that the quality of the starting sample is fundamental for the success of the etching steps. In particular, a defect free sacrificial layer is pivotal to avoid any rupture of the underlying membrane as well as a flat bonding between the membrane and the new GaAs substrate.

Transferring the membrane on a micromachined piezo device

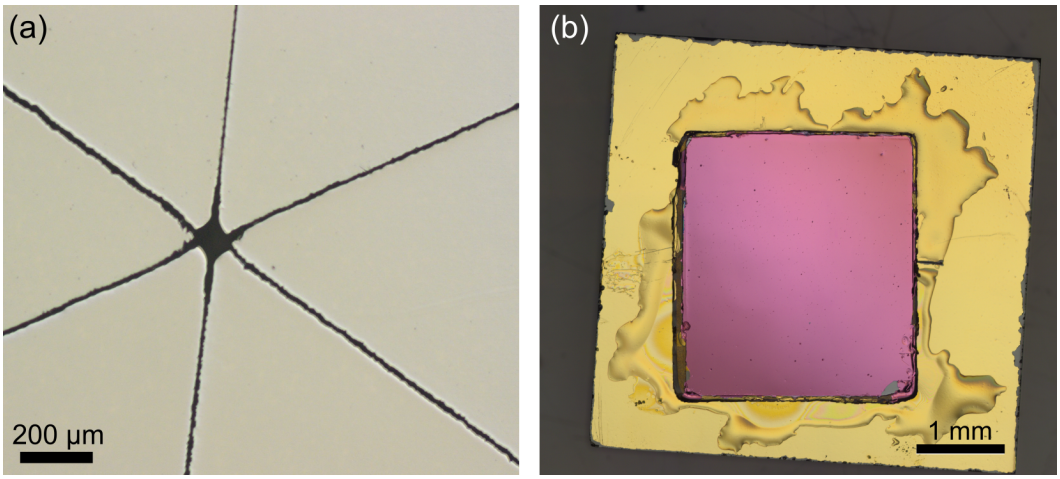

Figure 4.5. Microscope images of a micromachined piezo device. (a) Close-up of the central part of a piezoelectric device before it receives the gold contacts. (b) Microscope picture of a finished membrane on six-legged device. One of the cuts of the piezoelectric device is visible on the right side of the membrane.

To efficiently transfer stress to the QDs we would ideally want to apply the membrane directly to the six-legged piezoelectric device. In this way, huge amounts of strain can be reached in the membrane [64]. The nanometer-thick membrane is unfortunately extremely delicate and prone to breaking or wrinkling when manipulated in the subsequent processing steps. To avoid a process bottleneck, we resorted instead to reduce the thickness of the GaAs substrate to $\sim 50\,\mu m$ by mechanical lapping, see Fig. 4.4(g), reducing the amount of stress applied but increasing the stability of the membrane. This strategy is very effective for FSS as demonstrated by Huber *et al.* [42]. The sample is thinned down with the help of an abrasive mixture of water and powdered Al_2O_3 by making it slide between two glass plates

in a lapping machine (Logitech 1PM52) until the desired thickness is reached.

The six-legged micro-machined device is prepared from a commercial PMN-PT crystal. The three cuts are obtained with high-power laser ablation, with a femtosecond laser having central wavelength of 520 nm, repetition rate of 25 kHz and a 5 µm spot size [49], see Fig. 4.5(a) which shows the center of the device. A single device is roughly 5 mm × 5 mm in size with the cuts extending for 3 mm at 60° from each other. The electric contacts are fabricated by sputtering gold on the two sides of the piezo, patterning one side with optical-lithography to separate 6 contacts, one for each leg, see Fig. 1.16.

We resort again to SU-8 2 as a glue to bond the micro-metric membrane to the piezoelectric device. In this case, the photoresist is brushed on the single legs, trying to avoid it creeping between them. The lapped membrane is transferred by hand to the device and it is heat-bonded without using any applied pressure, not to damage the piezo-device, see Fig 4.4(h). An example of the final device, ready to have cavities processed on it, is shown in Fig. 4.5(b).

4.2.2 Quantum dot position acquisition

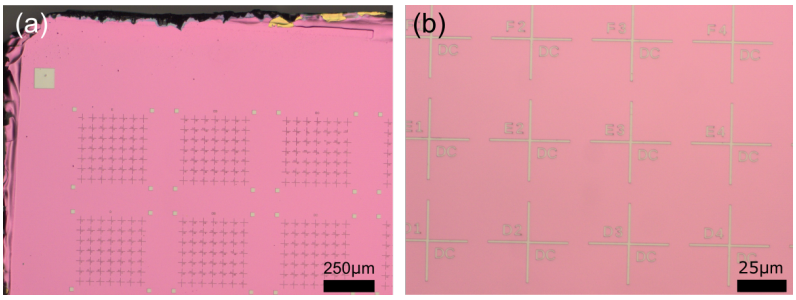

Figure 4.6. Metallic markers applied on the surface of a membrane. (a) The marker fields are arranged in square matrices with filled squares for alignment of the electron beam lithography machine. (b) Each marker field is represented by 4 crosses in a 50 µm × 50 µm square. Each marker field is identified by letters and numbers.

To establish a frame of reference for the position of the QDs, we need to deposit a marker grid on the membrane to be read again when etching the cavities. This is done by patterning a mask with electron beam lithography (EBL). The mask is obtained by spin coating a chemically enhanced positive e-beam resist (AR-P 6200.09 CSAR 62 from Allresist) on the surface of the sample. After patterning with the focused electron beam and developing the mask, the positive design is transferred on the surface. Then, a layer of metal is deposited on top of the sample surface with physical vapor deposition. The mask is then lifted with a specific solvent (anisole) so that only the patterned markers are left on the surface of the sample. In order to re-detect the markers under the EBL machine, a high atomic number metal (like

Au) has to be used, covered by a thick layer of Cr to block the light reflected from the HBR and increase the contrast.

The metallic markers consist in a series of crosses, of 1 µm width and 40 µm length, arranged in a square lattice with a 50 µm period, see Fig. 4.6. Four crosses enclose a single square that we call marker field, identified with a number and a letter for the row and column respectively. Depending on the EBL machine writing field of view we can group several marker fields together, with filled squares at fixed distances placed around the area as references for the EBL alignment.

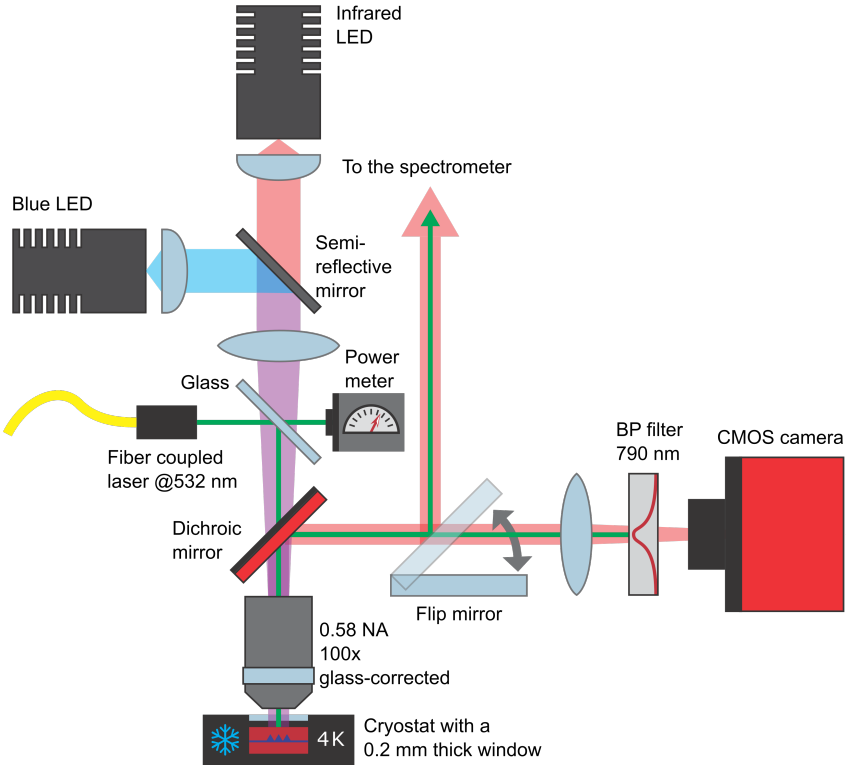

Figure 4.7. Scheme of the low-temperature imaging setup for nanoscale positioning. The two light emitting diodes (LEDs) sources are collimated with a condenser lens and combined with a semi-reflective mirror. The blue LED is used to excite above-band the QDs while the IR LED is used to contrast the metal markers on the sample surface. The light from the LED is roughly focused on the back focal plane of the microscope objective with a lens. A glass slide introduces in the optical path the light coming from a diode laser at 532 nm which is used to excite single QDs. The light is focused by a high-numerical aperture objective placed outside the cryostat, equipped with a tunable correction for aberrations due to the cryostat window. The sample is placed in the cryostat and kept at low temperature by a continuous flow of liquid He. The light coming from the sample is separated with a dichroic mirror and sent to a high-resolution CMOS camera. Here the image is focused by a lens and the light is filtered by a bandpass filter centered around the QD emission. The light spectrum from the QDs can be analyzed by placing a mirror in the optical path toward the camera and sending it to a spectrometer. Courtesy of T. Krieger.

The concept of the microscope imaging setup proposed by Liu *et al.* [140] to detect the position of the QDs is adopted in our laboratory with some modification. It works with an illumination system constituted by two light emitting diodes (LEDs), see Fig. 4.7. The high energy, blue LED is used to excite the QDs, while the infrared LED is used to reflect light from the sample and image the negative shape of the markers. The light from both the LEDs is focused in the back focal plane of a high numerical aperture objective, to obtain a complete and even illumination of the sample underneath. The objective sits outside the cryostat and has the possibility to correct for the aberrations introduced by the cryostat window. The sample is kept at low temperature (<10 K) inside the cryostat to observe the PL emission from the QDs. The light coming from the cryostat, both the reflection of the IR LED and the emission from the QDs, is reflected with a dichroic mirror toward a high resolution CMOS camera. Here, the unwanted light is rejected with a passband filter centered at the emission wavelength of the QDs and focused on the camera sensor with an achromatic doublet. The magnification of the objective and focusing lens system is chosen so that we fill the camera sensor with a single marker field reaching the best resolution while keeping the frame of reference in every single image. The total magnification is roughly 50X and each pixel of the camera corresponds to ∼50 nm on the sample. A typical image from the sample is shown in Fig. 4.8(a). The fiber-coupled light coming from a diode laser can be inserted in the optical path toward the sample to obtain PL from single QDs. The spectra can be collected by sending the emitted light toward a spectrometer with a flip mirror in the optical path. This information is essential to tailor the cavities around the emission of every single QD.

The collected images are processed with a Python script initially developed by C. Kohlberger and refined by T. Krieger and the author, to obtain the QD positions with respect to the marker field origin. The program is based on the *scikit-image* library of Python [142]. The script takes as an input the image from the camera and outputs the position of the QDs. It starts by detecting the markers with a Hough transform [143] and then optimizes the initial guess with Gaussian fits across the marker lines, see Fig. 4.8(a). Once a frame of reference is established, the program runs a local maxima detection and then performs a 2D Gaussian fit around each of the detected maxima, see Fig. 4.8(b). The center position coordinates of the Gaussian peaks are saved as a list in a text file.

To assess the precision of the procedure we ran two different test. First we take several images of the same marker field, while slightly changing the position of the sample below the objective to create a variation in the images. We then run the program over the whole set of images and re-detect the same QDs on every image.

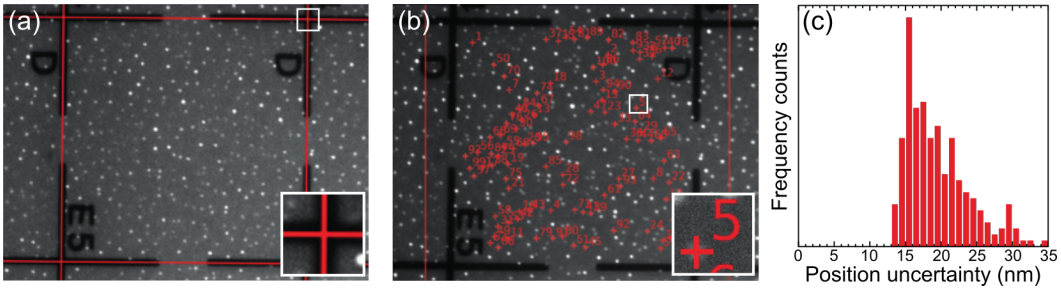

Figure 4.8. Description of the marker recognition procedure. (a) The Cr markers block the IR light reflected from the HBR below the membrane and result as dark areas on the image, the program runs a first guess of the position of the marker field lines with a Hough transformation. The guess is then refined by Gaussian fits and the results is shown as red lines superimposed on the original image. (b) The program then checks for local maxima of the PL intensity in the image and runs a 2D Gaussian fit around each peak. The center of the Gaussian is marked as a cross on the image and each peak is labeled with a number. (c) The deviation in position under re-detection of single QD positions is shown as an histogram, showing a peak at around 15.5 nm. Courtesy of T. Krieger.

We store the differences in the detected positions and plot the histogram of the variances $\sigma = \sqrt{\sigma_x^2 + \sigma_y^2}$, see Fig. 4.8(c). The mean error in the re-detection is less than 20 nm.

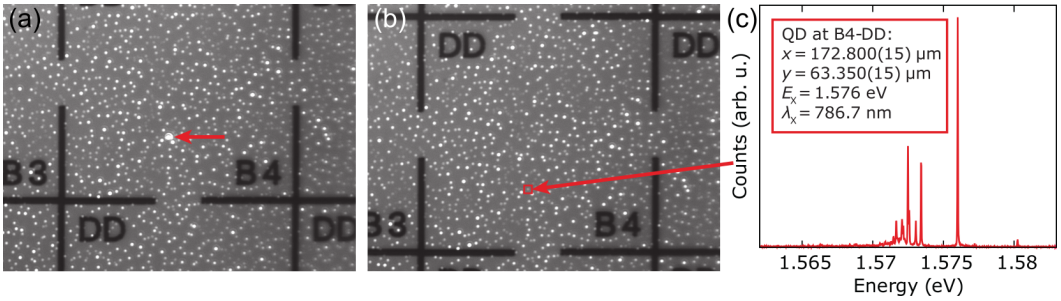

Figure 4.9. Visualization of the procedure to acquire a single QD position and spectrum. (a) The sample is scanned while looking at the spectra of QDs until a suitable QD is found, we then switch to imaging mode. The QD will be highlighted by the laser light, we mark its position with respect to the markers. (b) The program is run by reducing the scanning area to a region of interest around the wanted QD (red square), and the position of the QD is stored. (c) The spectrum of the QD is analyzed and the complete identikit for the QD is stored to be used to tailor a cavity around it. Courtesy of T. Krieger.

To link the position of a QD to its spectrum we scan the sample manually while looking at the output of the spectrometer. Once a suitable QD is found, we store its spectrum and switch back to the imaging mode. The QD will be highlighted with respect to the other QDs, see Fig. 4.9(a). A second picture containing all the crosses of the marker field is taken. It is compared to the one already processed by the program and the corresponding QD position is found by restricting the fit in

a region of interest around the QD, see Fig. 4.9(b). The whole set of information belonging to a single QD is stored in a text file to be read again when creating the resonators design, see Fig. 4.9(c).

4.2.3 Dry etching of cavities

The positions of the QDs with respect to the markers and their wavelengths need to be converted into a CBR design which will be then patterned on a resist mask on the sample surface with EBL. The design will then be permanently transferred to the membrane with chemical etching.

Electron beam lithography

An e-beam resist (AR-P 6200.09 CSAR 62 from AllResist) is deposited on the surface of the sample by spincoating, covering also the metal markers. The EBL machine, a Vistec EBPG 5HR, operating at an acceleration voltage of 100 kV, accelerates and focuses a beam of electrons on the surface of the sample. In the case of positive tone resist, as the AR-P 6200.09, the exposure with the correct dose of high-energetic electrons weakens the cross-linked structure of the resist which is then removed only in the exposed areas during the development. The resist is spincoated at 4000 rpm (resulting in a thickness of ∼200 nm) and baked at 150 °C to evaporate the solvents and enhance its sensitivity. After exposure, the mask is developed in isoamyl acetate to remove the exposed areas.

The EBL machine can also read the metal markers below the resist and reconstruct the same frame of reference used to find the QDs positions. In this way the pattern will be aligned with the existing marker field. Preliminary tests of the patterning precision were performed on a 30 kV Raith eLine Plus EBL machine in Linz by patterning Au discs on QD positions and re-detecting the position of the discs in the imaging setup. The procedure was repeated on more than 20'000 different QDs showing a Poissonian distribution of position errors peaked around 35 nm.

The EBL design for the positioned CBRs is automatically built with a custom script in the Python environment of the open-source program KLayout [144]. The script reads the list of QDs positions and wavelengths in a text file and creates a set of CBRs with the target central cavity centered on each QD. An example of the resulting design is shown in Fig. 4.10.

After the mask is exposed and developed, a second baking step at 130 °C hardens the resist and makes it more resistant against etching. The sample at this stage is ready to be processed in the dry-etching machine.

Dry etching, as opposed to a wet-etching procedure, in which the sample is submerged in liquid chemicals, exploits reactants in the form of accelerated ionized

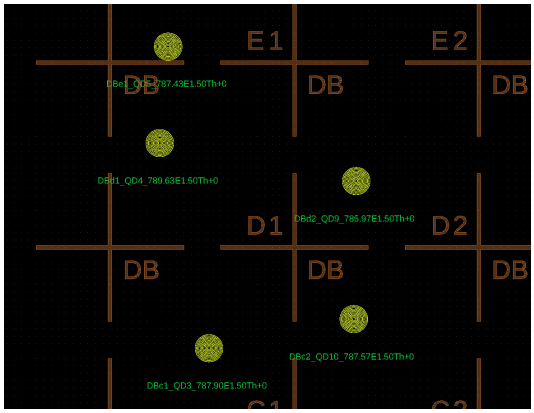

Figure 4.10. Electron beam lithography design for positioned CBRs. Each cavity is placed around a QD whose position was previously measured in the PL imaging setup. The diameter of the cavity is tailored so that the cavity resonance matches the emission energy of the QD.

gas to etch a material. The gas is ionized by a a radiofrequency (RF) field and accelerated toward the surface of the sample by a self-generated DC bias [145].

For the etching of GaAs/AlGaAs structures a combination of Cl_2, BCl_3 and Ar is routinely used [146]. Each chemical has a different role in the final result: Chlorine ions and radicals are the responsible for the chemical etching of GaAs/AlGaAs, reacting on the surface of the sample to form several compounds of different volatility [147]. To get rid of the products of the reactions, argon is introduced, acting as a mill to physically remove etching products from the bottom of the etched pattern. To enhance the anisotropy of the etching, and hence obtaining vertical sidewalls, boron trichloride is introduced. The reaction products of the BCl_3 are easily sputtered, protecting the sidewall surface from the isotropic etching of chlorine [148].

The sample with the patterned mask on top is placed in the chamber of an Oxford Plasmalab 80 Ion Etching machine, where vacuum is established. The whole machine is enclosed in a Nitrogen-purged box to remove detrimental effects of atmospheric water. Then, a $Cl_2/BCl_3/Ar$ (2.6/39/6 sccm) mixture is introduced in the chamber. The pressure inside the chamber is regulated to 10 mTorr with a throttle valve placed in front of the pumping unit. The gas mixture is ionized by a 100 W RF field driven at 13.56 MHz, the accumulation of charges on one of the electrodes of the chamber is blocked by a capacitor which establishes a DC bias accelerating the plasma toward the sample surface. In a RIE the DC voltage depends on the geometry of the chamber and can vary with the conditions of pressure and gas composition in the chamber in a range of 10 V to 100 V. A schematic of the procedure is shown in Fig. 4.11(a). With the conditions described above we reach an etching rate of the membrane of $\sim$150 nm min^{-1} and a resist etching rate of $\sim$30 nm min^{-1}. The significantly slower

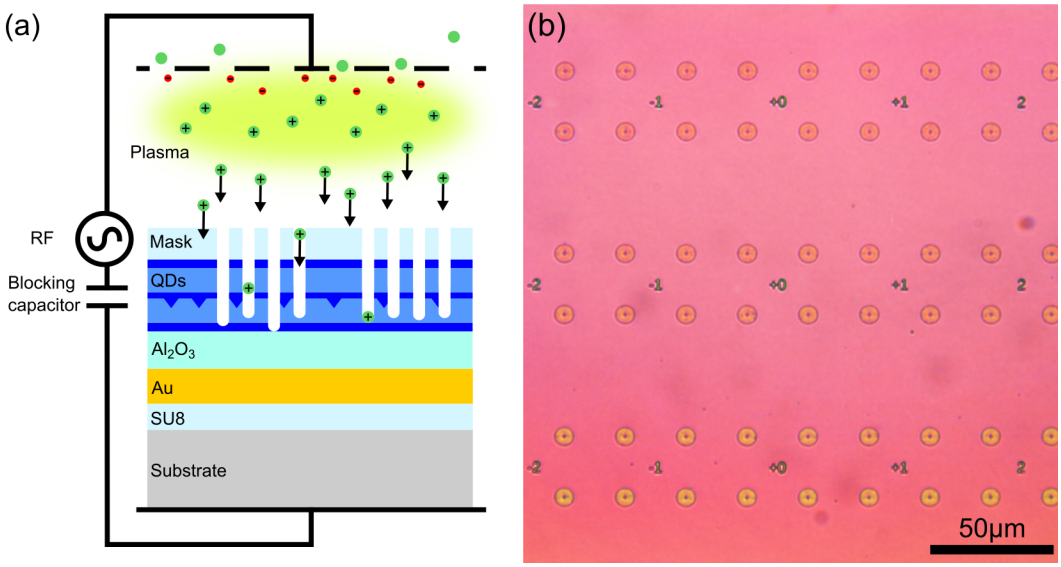

Figure 4.11. (a) Schematic drawing of a reactive ion etching machine. The gas mixture of etching chemicals is ionized by a radiofrequency field and accelerated toward the sample by a DC self-bias established by an accumulation of charges in the blocking capacitor. The surface of the sample is covered with an e-beam mask. Holes in the mask were patterned with electron beam lithography to expose the surface of the sample to reactants. (b) Microscope image of the surface of an etched membrane. Each circular feature is a single CBR. The individual rings of the circular Bragg grating are not resolved with visible light but produce interference patterns around the central cavity.

etching rate of the oxide (more than one order of magnitude slower [149]) below the membrane acts as a stopping layer, preventing over-etching of the sample.

The residual resist is removed from the surface by placing the sample in hot anisole (60 °C). An example of the result of the etching is shown in the microscope picture in Fig. 4.11(b). The single rings of the structure are not resolved by an optical image, resulting in interfering patterns visible around the center of the cavity.

We also resorted to a different etching technique called inductive coupled plasma etching (ICP). In an ICP machine two RFs are employed so that it is also possible to tune the DC bias and obtain a more controlled etching speed. The ICP etching was performed in the Technical Physics Institute of the Julius Maximilian Würzburg University. Here the mask was patterned with a Jeol JBX-9300FS 100 kV EBL. The ICP machine is a PlasmaPro 100 from Oxford Instruments, operating with a Cl_2/Ar mixture (1.7/18 sccm) at 10 mTorr pressure. The gas mixture is ionized by a 125 W RF field and accelerated by a 214 V static voltage. The membrane etching speed is estimated as $\sim$70 nm min^{-1}.

4.3 Morphological and optical analysis

In this Section we will discuss the characterization of the morphological and optical properties of cavities obtained with the two different etching techniques described above. The samples morphology is first studied in a scanning electron microscope (SEM). Recognizing the limitations in precision of the microscopy techniques we resort to a more precise method to assess the microscopic properties of our cavities and study their response to light in reflectivity measurements. In the last part of this Section we will show the final result of all the processing steps described in the previous Section with a characterization of the low temperature PL emission of single QDs embedded inside a CBR and preliminary results for the strain tuning.

4.3.1 Reactive ion etching results

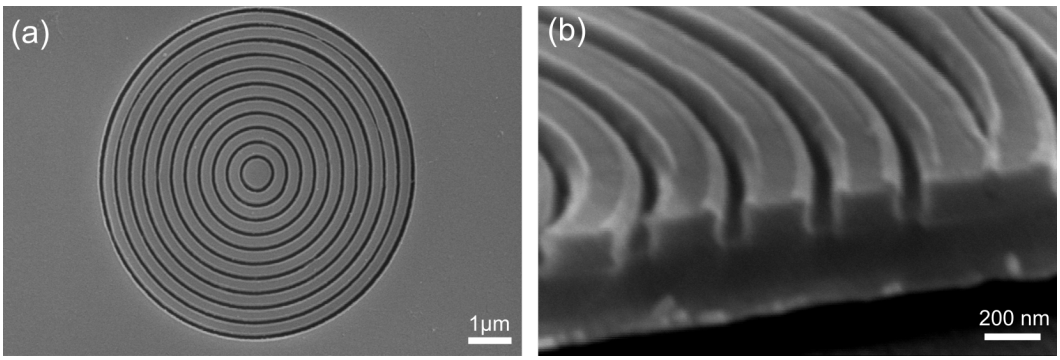

Figure 4.12. Scanning electron microscope (SEM) images of circular Bragg resonators. (a) Top view and (b) lateral cut SEM images of a sample from the first etching tests in a reactive ion etching machine. The sample, featuring a SiO_2 oxide layer, was etched for 6 min with a 30 s O_2 plasma cleaning step every 2 min. The droplet shape of the etching profile and the sputtered material visible on the ridge suggests an overetching has occurred. Courtesy of G. Pettinari.

The first step before etching the cavities is to optimize the charge dose in the EBL machine to correctly expose and develop the mask. Regarding the RIE etching, we used the recipe described above, used with success in the etching of GaAs photonic crystal [146], which is also compatible with our AlGaAs membrane. The etching times are optimized in several tests by analyzing the morphology of the cavities at the SEM and by observing the optical properties of the cavity with reflectivity measurements.

The SEM images for one of the first samples are shown in Fig. 4.12. Here the etching is performed in 2 min steps followed by a 30 s O_2 plasma cleaning to get rid of etching products. The procedure was repeated 3 times for a total etching time of 6 min. By looking at the SEM images we can see hints of overetching. The trenches

profile is droplet-shaped, indicating an increased etching at the bottom. This is due to the oxide layer below the membrane (SiO_2 for this sample) acting as a stopping layer. Once the SiO_2 is reached, the reactants cannot proceed any further and are left to carve the lateral sides at the bottom of the trench. This hypothesis is also supported by the evidence of sputtered materials on the edge of the trench, forming a lip which is clearly visible in Fig. 4.12(b).

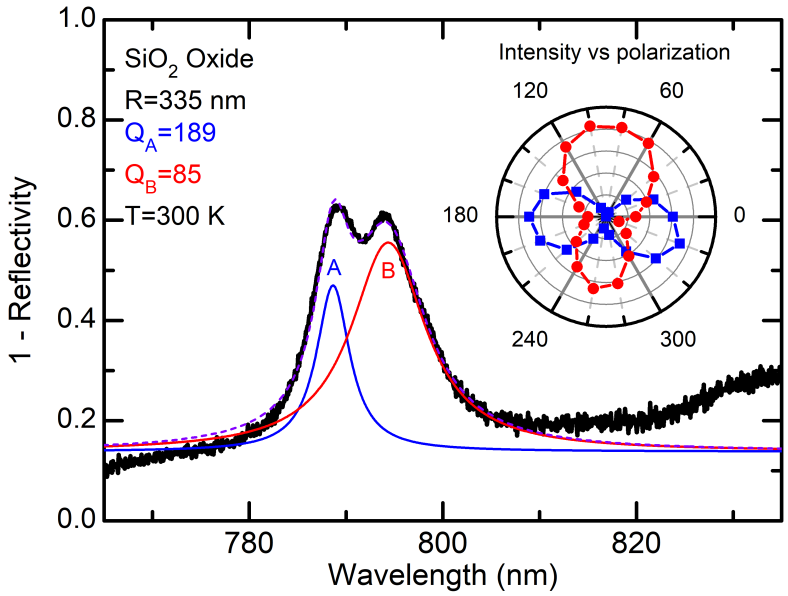

Figure 4.13. Room temperature reflectivity spectrum of a single CBR cavity on SiO_2 oxide. The cavity mode is split in two contributions which are orthogonally polarized, see polar plot in the inset.

Considering the reduced dimensions of the single features of the cavity, a quantitative analysis of anisotropies is extremely difficult with direct morphological investigation tools, namely atomic force microscopy (AFM) and SEM. The most powerful method to investigate the geometrical features of a photonic cavity is the study of its optical properties. To analyze the spectral response of the cavity, we acquired its reflectivity spectrum using the same setup we use for the PL, see Section 3.2, with the only difference of the excitation method. The source of the impinging light is, in this case, a broadband emitter, specifically a white halogen lamp. When we collect the light reflected by the cavity, we observe a dip in the (almost) flat spectrum of the lamp. This is because the cavity, when illuminated with a broadboand source, absorbs selectively the light which is in resonance with its cavity mode, thus telling us the properties of its photonic modes. The polarization properties of the reflectivity spectrum are studied by placing a halfwave plate mounted on a rotational stage and a linear polarizer in the optical path toward the spectrometer, in this way we can assess the linear polarization of the optical mode induced by asymmetries in

the cavity [150].

The first tests with the RIE produced a cavity featuring a double mode, with cross-polarized features, see Fig. 4.13. A tentative fit with the sum of two Lorentzian peaks, purple dashed curve, returns the two quality factors $Q_A = 189$ and $Q_B = 85$ for the lower and higher wavelength peak respectively. We attribute this result to an elongation of the cavity, which acquires an elliptical profile. The elongation removes the degeneracy between the two perpendicular modes of the cylindrical cavity. Additional simulations estimated a difference between the length of two axes of the ellipse of the central cavity of ∼15 nm from the 6 nm spectral splitting of the modes. This difference was not clearly confirmed by the morphological measurement of the cavity axes lengths using both SEM and AFM due to limitations in the experimental accuracy. Possible reasons for an elliptical cavity are proximity effects during the exposition of the mask, anisotropic etching along different crystal axes of the membrane, or even a strain release after etching. Following these hypothesis, we developed CBRs with elliptic designs to counteract the removal of the degeneracy, as discussed below.

Dealing with elliptical cavities

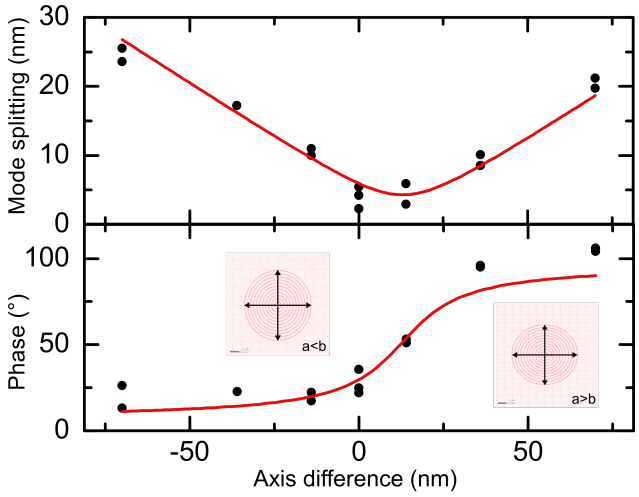

Figure 4.14. Wavelength splitting (top graph) and phase (bottom graph) of the two modes of the CBR cavities with different induced ellipticity in their design. The ellipticity is given as difference between the horizontal axis length (parallel to the EBL writing direction) a and the vertical axis length b, so that negative differences mean a vertically stretched cavity while positive differences a horizontally stretched cavity. The data is fitted with the model described in Eq. 4.2 and Eq. 4.3.

By investigating the reflectivity spectra of several cavities featuring a mode splitting, we see that the higher energy mode is always polarized perpendicular to the horizontal axis of the cavity (identified with the writing direction of the EBL

machine in a reading-order raster pattern), see polar plot in Fig. 4.13, and that all the cavities have roughly parallel axes. Following this information, we prepare a sample with elliptical cavities, with both vertical and horizontal elongation, with main axes aligned with the EBL writing axes. The procedure to erase the splitting of an elliptical cavity is similar to the one already described to erase the FSS of a QD, see Section 1.4. In the same manner as a QD with lowered symmetry removes the degeneracy of the X states, an elliptical cavity creates two modes, featuring a spectral splitting and orthogonal polarization. We model our cavity as an ellipse with the two axes as two vectors in the xy-plane defined by the EBL writing axes, as

$$\rho_{\pm} = k\hat{x} + (-\eta \pm \sqrt{\eta^2 + k^2})\hat{y} \tag{4.1}$$

Paralleling the notation used in Section 1.4, η and k here are the parameters determining the anisotropy of the cavity. The two axes of the elliptic design of the cavity a and b are used in analogy with the two stress direction S_1 and S_2, so that their difference $e = a - b$ is the parameter we change to reduce the mode spectral splitting.

The data obtained for cavities with values of e ranging from $-70\,\text{nm}$ to $70\,\text{nm}$ is summarized in Fig. 4.14. The spectral splitting s of the cavity with respect to the axes lengths difference e is plotted in the top graph. Here we see that a minimum in the spectral splitting is reached at the same time when there is a $\pi/2$ shift in the angle of the polarization of the higher wavelength mode, as observed when strain tuning QDs [151]. Following the analogy with the stress-induced changes in the electronic structure of the QD we can model it with the same Hamiltonian. The two sets of data can be fitted with the formulas from Ref. [49] which describe the effect on the FSS of the application of two stresses. By solving the Hamiltonian we derive the following equations for the splitting s of the cavity modes and the angle θ of the main axis of the ellipse:

$$s = \left[(\eta + \alpha e)^2 + (k + \gamma e)^2\right]^{\frac{1}{2}} \tag{4.2}$$

$$\theta = \arctan \frac{k + \gamma e}{\eta + \alpha e + s} \tag{4.3}$$

where γ and α gives the response of the cavity to an elliptical design.

From the fit parameters we can obtain the values of the spectral splitting and angle of the unbiased cavity, i.e., a cavity with a circular design but an elliptical

outcome:

$$\Delta = \sqrt{\eta^2 + k^2} \tag{4.4}$$

$$\theta^* = \arctan \frac{-\eta + \Delta}{k} \tag{4.5}$$

which results in $\Delta = 6(2)\,\text{nm}$ and $\theta^* = 29.4(5)°$. The result for the splitting of the cavities matches well with the values obtained for the previous samples.

To tune the the spectral splitting to zero we would need to align the angle of the ellipse to θ^* and create several elliptical designs with different ellipticities. We then prepare a sample where the axes lengths difference is changed in smaller steps and the ellipse is tilted around different angles. The analysis of the data suffers from the limited reproducibility of the etching process, with typical standard deviations of $>1\,\text{nm}$ for the splitting and $>10°$ for the angle and it was not possible to reduce the splitting consistently below values of 2 nm.

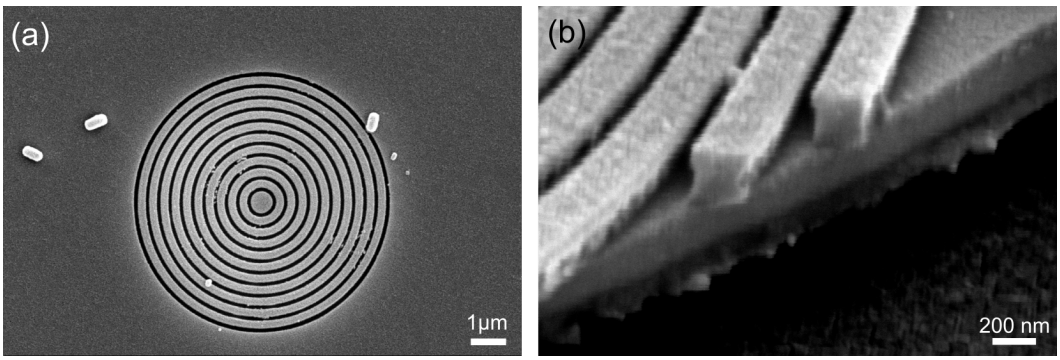

Figure 4.15. (a) Top view and (b) lateral cut SEM images of a sample with optimized etching. This sample, featuring a Al_2O_3 oxide layer, was etched in a single 90 s etching step. We can observe how the walls of the trenches appear more vertical. The sample was covered in a Au layer to reduce the charging in the SEM. Courtesy of G. Pettinari.

The poor reproducibility we observed could be ascribed to a non-optimized etching, in particular to an overetching, as observed by SEM, see Fig. 4.12. The etching time was then turned down to 90 s and the O_2 plasma cleaning step removed. Moreover, we switched to a more reliable Al_2O_3 deposition with ALD, to improve the membrane stability. The morphology of the sample improved, as we can observe in Fig. 4.15. Here the walls of the trenches appear more vertical, with no material sputtering visible. A new series of tests with the new optimized etching is underway.

4.3.2 Inductive coupled plasma etching results

In parallel to the RIE etching optimization, we have decided to also test ICP etching at the Würzburg University facility. Here cavities are obtained with the

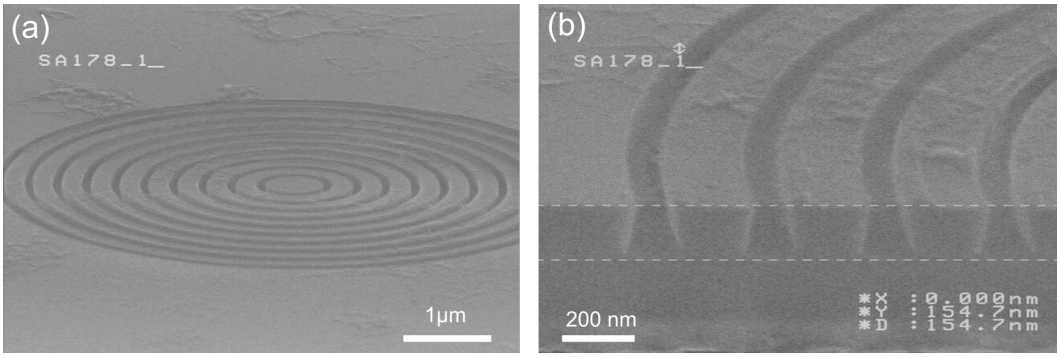

Figure 4.16. (a) Tilted and (b) cross section views of a typical CBR cavity obtained with ICP etching in the Würzburg University facility. The non perfectly vertical walls indicate a non optimized, partially isotropic etching. Courtesy of Dr. M. Moczała-Dusanowska.

process described in Section 4.2.3. The results of the first test performed on a membrane sitting on a GaAs substrate and with a Al_2O_3 oxide layer are shown in the SEM images in Fig. 4.16. The etched cavities exhibit a regular shape with still room for improvement, as the walls of the trenches are not perfectly vertical, see Fig. 4.16(b). The slanted walls suggests a partially isotropic etching, carving the membrane also horizontally while proceeding vertically. This imperfection, which is most probably caused by the absence of the passivation effect of the BCl_3 ions on the exposed vertical walls, is not degrading the optical quality of the cavity as confirmed by the reflectivity measurement shown in Fig. 4.17. The Figure shows a narrow cavity mode with a quality factor $Q = 125$ and no evident splitting. We also prepared another sample with several cavities designed in a set of evenly spaced radii and measured their optical response at room temperature to check the dependance of the cavity mode to the radius of the cavity. The results are summarized in the inset of Fig. 4.17, showing the expected linear dependance of the cavity mode wavelength to the central cavity radius [40] with a slope of 1.31(4) and an offset of 377(16) nm.

Low temperature measurements

The etched sample is mounted in the closed-cycle cryostat for low temperature measurements (5 K) to characterize the shift of the cavity mode with temperature and to observe any degradation of the quality of the QD emission due to the etching process. Here we observed several QDs/cavities both in reflectivity and in PL with above band excitation. Despite the cavities are fabricated randomly, i.e., without knowing the QD positions, almost every cavity we observed features one or more QDs whose emission is enhanced with respect to the QDs outside a cavity in the same membrane. This fact comes as no surprise because the enhanced extraction efficiency of the CBR is flat for a very wide range of wavelengths. It is sufficient for

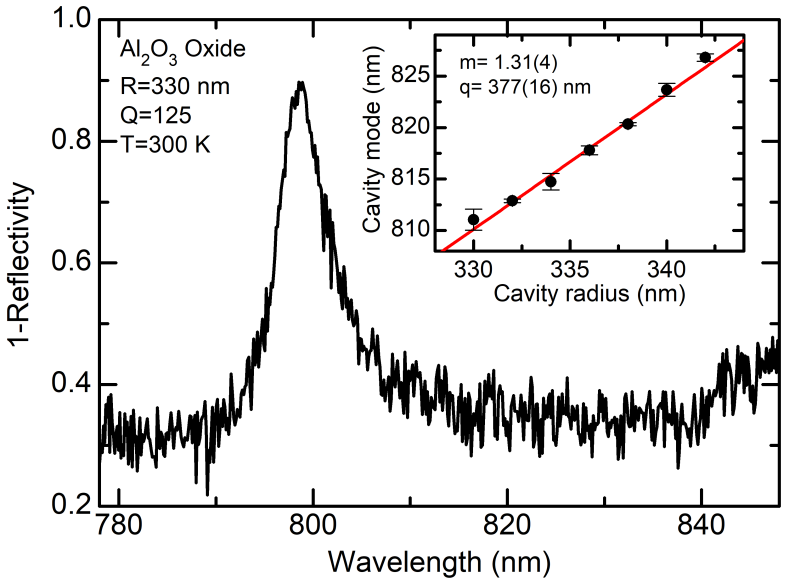

Figure 4.17. Room temperature reflectivity spectrum of a single CBR cavity on Al_2O_3 obtained with ICP etching in the Würzburg University facility. In the inset: room temperature study of the cavity mode shift dependance versus the cavity radius for another calibration sample. The result from the linear fit is used to calibrate the design to match the QD emission energy.

the QD to sit anywhere inside the photonic structure to increase the collection of the emitted light.

In Fig. 4.18 we report the reflectivity spectrum of a cavity which is also mode-matched to the *s*-shell of a QD inside it. We observe the appearance of the QD emission already when illuminating the cavity with a broadband light source, namely a halogen lamp. The fact that the QD is already excited at the very low power density reached by a broadband source confirms the high efficiency of the QD excitation and collection of signal. We characterize the PL emission of the QD, see Fig. 4.19(a). The QD shows a PL spectrum with a clearly distinguishable X line at high energy. The FWHM of the line is 85 µeV, close to the resolution limit of our spectrometer. This suggests that the effect of surface states and oxidation of the walls are not significantly detrimental to the emission properties of the QD [152].

The light coming from the QD is fiber coupled and sent to the spectrometer. The integrated counts at the CCD are, for this QD, 680 kcps. To get a comparison, these are roughly 5 times the counts obtained for the QD used for the experiments of Chapter 3, which had an estimated 10% extraction efficiency and 0.33 on-time fraction due to blinking. The correct estimation of the extraction efficiency will require a deeper investigation of the emission characteristics, a task that we leave for future studies in optimized cavities. What we compared here is the brightness

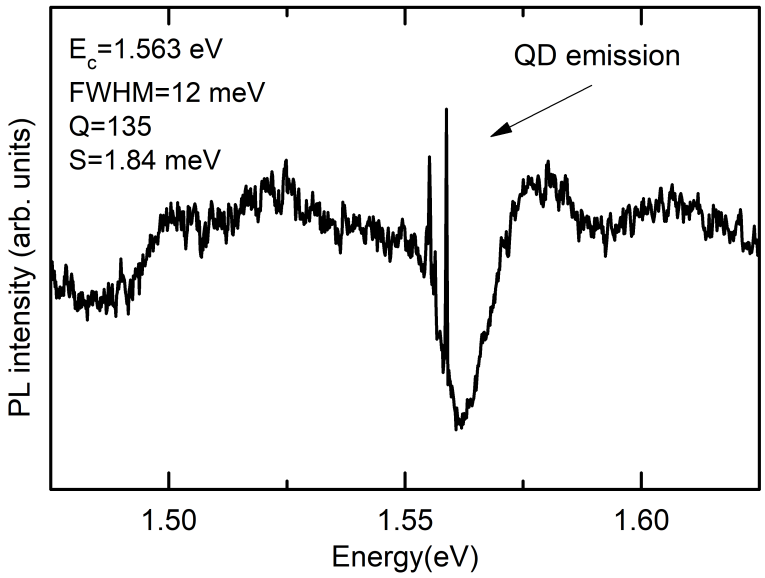

Figure 4.18. Low temperature photoluminescence spectrum of a single CBR cavity with no designed positioning nor mode-matching excited with a halogen light. The narrow line inside the cavity mode is a single QD inside the cavity that has its emission energy matching that of the cavity.

measured at the CCD detector of the spectrometer, which takes into account the amount of photons entering into the setup from the cryostat. The brightness measured in continuous wave excitation depends on the extraction efficiency but also on other parameters such as the blinking of the source, an effect that strongly depends on the sample characteristics, on the efficiency of the excitation, which can be precisely estimated for pulsed resonant excitation, and on the lifetime of the excitation, which depends on the Purcell enhancement experienced by the emitter.

We study the polarization dependance of the intensity and the position of the X line by placing a halfwave plate and a polarizer in the optical path, see Fig. 4.19(b). The emission of the QD is heavily polarized, with a calculated degree of polarization of 0.85, suggesting a deviation of the QD position from the geometrical center of the cavity [138]. The study of the FSS of the emission gives a very low value of 1.2 µeV but one of the two components of the X state is strongly suppressed by the cavity, which makes our estimation much less accurate. The limited energy range of operation of the setup used for resonant excitation, in particular related to the use of notch filters, that can be tuned only a few nanometers away from 785 nm, made impossible to study this QD emission under pulsed excitation, which is planned for optimized samples with positioned cavities.

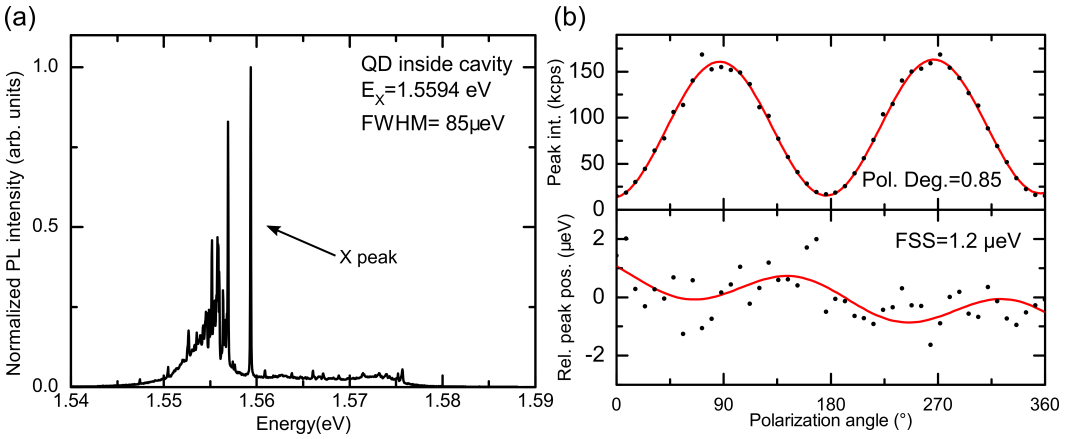

Figure 4.19. (a) Low temperature PL spectrum of the same QD of Fig. 4.18 excited above band with a He-Ne laser. The QD was found inside a CBR cavity but the mode matching of the QD to the cavity was not planned. (b) Polarization study of the X peak intensity (top) and position (bottom). The high degree of polarization of the emission intensity indicates that the QD is not in the exact center of the cavity. The low value of the fitted FSS is most likely due to the suppression of one of the two components of the X emission.

4.3.3 Positioned circular Bragg resonators on piezoelectric actuators

To reach the highest extraction efficiency possible with no induced polarization on the emission, the cavities must be positioned around single QDs and mode-matched to their emission wavelength. The positioned cavities need also to be combined with the micromachined piezo devices described in Section 1.4 if we want to exploit the three-axial strain-tuning to erase the FSS and tune the emission wavelength.

The membrane bonded on the micromachined piezo received a marker field pattern that was carefully placed in the center of the six cuts of the piezo, where the three-axes strain transfer is bigger. Only 4 marker fields are suspended on the central gap (∼100 µm) left between the six legs of the device, see Fig. 4.5(a).

The sample is placed in the cryostat and the position of the QDs are measured with the imaging setup described in Section 4.2.2. We select around 60 QDs by their wavelength, limiting the search to no more than one QD per marker field. Each marker field picture is collected and later analyzed with the Python script. On free marker fields, where no QD spectrum is analyzed or the image analysis fails to retrieve its position, a test cavity is placed on a random QD selected from the image. The list of the QD positions and emission wavelengths is then used to pattern the mask.

We observed that the cavity resonance has a strong dependance on the starting membrane characteristics, such as the membrane thickness. This phenomenon is

confirmed by theoretical predictions performed by the group in Würzburg [153]. Small variations (∼nm) of the membrane thickness within the same sample are possible even with a precise method such as MBE and their effect on the cavity mode is not negligible. To take this effect into account, we perform an etching calibration test on the same sample before the positioned cavities are etched, sacrificing a small part of the membrane. We pattern the sample with CBR with different designed radii, etch it and then measure the mode dependance on the radius. Using this curve, corrected for the temperature shift, we can get a precise calibration of the mode versus radius dependance, and obtain cavities which are tailored on the QDs emission wavelengths independently from the starting sample.

The sample is again patterned with EBL and etched. This time, the EBL machine is programmed to read the metal lines of the markers to reconstruct the frame of reference of each marker field and place the cavity with the correct radius on the correct position around the QD.

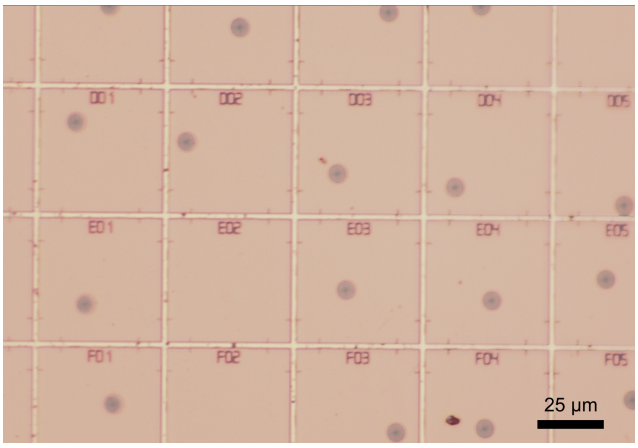

Figure 4.20. Microscope image of a positioned sample on a micromachined piezo-device. Each cavity is etched around the coordinates of a single QD with respect to the metal markers patterned on the sample surface.

Figure 4.20 shows a microscope image of the first processed sample with positioned CBR cavities on a six-legged device. Here we can see that almost each marker field contains a CBR. The thin perpendicular lines across the marker field lines are due to the reading process of the EBL machine. Since the machine uses the same electron beam to measure the position of the lines, it exposes the resist in those areas and leaves the surface of the sample without protection from the mask against the reactant of the ICP.

The sample is glued face down with silver paint inside a custom made Cu dome to improve the thermal contact with the cryostat cold-finger while leaving the back of the sample free for placing electric contacts for the high voltage application, see

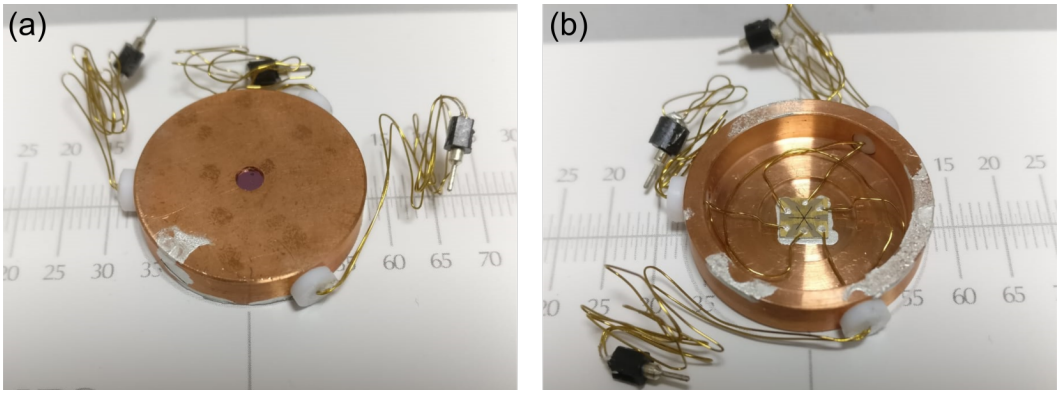

Figure 4.21. Top (a) and bottom (b) view of the positioned CBR sample on a sixlegs micromachined device in the Cu dome sample mount with connected electrical contacts. Electrical ground and thermal contact are established by bonding the sample face-down inside the Cu dome. A hole in the center of the dome allows for optical access of the sample. Each opposing leg is contacted on the same pin with Manganin wires. The scale below the sample is in mm.

Fig. 4.21. A hole in the top of the dome leaves the sample surface accessible of optical measurements. Six insulated Manganin ($Cu_{0.86}Mn_{0.12}Ni_{0.02}$, an electrically conductive material known for its low heat transfer) wires are attached with conductive silver paint to each of the contacts on the back of the piezo device, see Fig. 4.21(b). The wires from opposite legs of the device are then connected together in the same pin and to the positive contact of each of the three coaxial cables feeds of the cryostat. The common ground is connected to the top contact of the sample through the dome. The whole device is secured to the sample mounting plate of the cryostat with silver paint to ensure thermal coupling and electrical grounding.

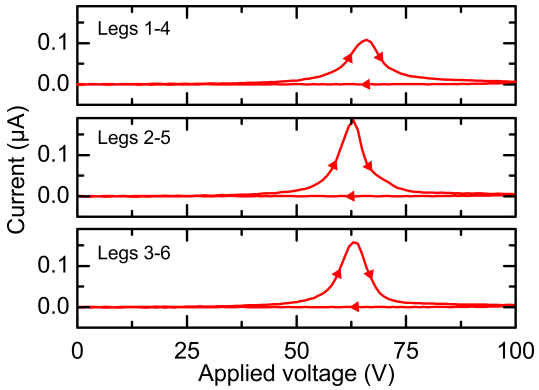

Figure 4.22. Current versus applied voltage plots recorded during the poling process of the micromachined piezo device showing the expected hysteresis behavior for the domain alignment and onset of a macroscopic polarization for all the three couples of legs.

The process of bonding the membrane to the piezo device is performed at a temperature that exceeds the critical temperature of the piezoelectric material,

which then loses its electro-mechanical properties. It is then necessary to realign the dipoles domains to regain the piezoelectric properties of the material and to do so we gradually apply a high voltage (100 V) on each couple of legs before cooling down the sample. As the voltage increases there is a net current flow between the contacts on the opposite faces of the material and a reorientation of the dipoles, resulting in a peak in the I-V response of each leg, see Fig. 4.22. The same peak is absent when sweeping the voltage down, confirming the non-reversibility of the process. After this procedure, the device is ready to transfer deformations onto the membrane containing the QDs and the cavities with the application of voltage.

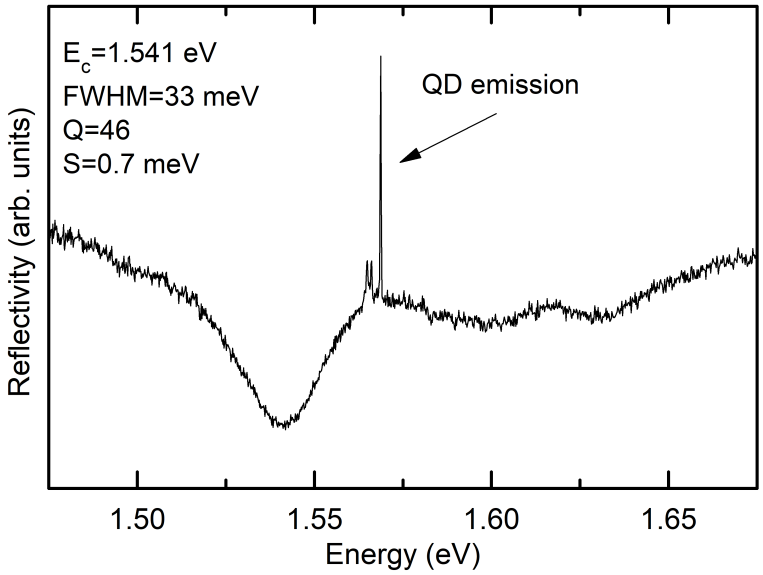

Figure 4.23. Low temperature photoluminescence spectrum of a single CBR cavity positioned around a single QD excited with a halogen lamp light. The planned cavity mode shifted due to an error in the design of the device and the QD is not perfectly mode matched. It is still possible to obtain an enhancement of the extraction efficiency.

Low temperature measurements

The sample is then characterized at 5 K. An error in the design files of the cavities produced larger than planned cavities with non-optimized Bragg grating duty cycle. This error produced a redshift of ∼15 nm of all the cavity modes and a strong reduction of the quality factor of the cavity down to $Q = 40$.

Despite the energy detuning, we were still able to find several QDs with an enhanced light extraction, and we focused our attention to one in particular, in the zone above the central gap of the six legs, showing an exceptional brightness. The reflectivity spectrum of the cavity in Fig. 4.23 shows again, together with the cavity mode dip, the QD emission, in this case at a higher energy with respect

to the cavity resonance. The horizontal scale of this graph is the same as for the reflectivity spectrum of Fig. 4.18, so that we can appreciate the lower Q of this cavity from the shape of the resonance with respect to the sample processed on the GaAs substrate. The Lorentzian fit gives a Q factor equal to 46, which is the result of the superposition of the two orthogonally polarized modes with $Q = 33$ and $Q = 59$ and an energy splitting of 0.7 meV. Here, the cavity mode match is much worse than in the previous sample, with an energy difference between the X emission line and the center of the cavity of about 30 meV, comparable to the FWHM of the resonance.

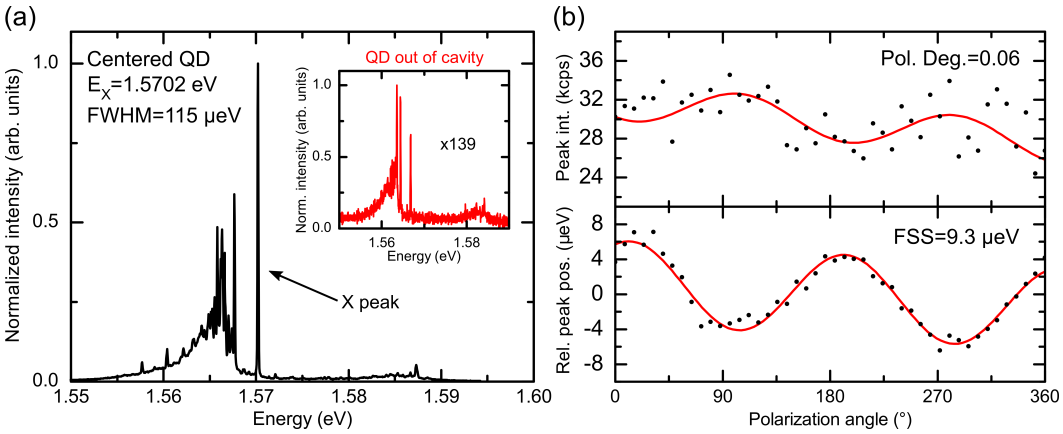

Figure 4.24. (a) Low temperature PL spectrum of the same QD of Fig. 4.23 excited above band with a He-Ne laser. The comparison with the spectrum of a single QD from the membrane of the sample is given in the inset multiplied by a factor 139. (b) Polarization study of the X peak intensity (top) and position (bottom). The very low polarization degree of the X line intensity indicates a good centering of the QD inside the cavity. The $\cos^2$ fit of the X emission energy returns a value of the FSS of 9.3 µeV.

The resulting PL spectrum from the embedded QD is shown in Fig. 4.24(a). Here the QD is excited with a He-Ne laser whose excitation power is controlled to reach saturation of the X peak. The FWHM of the X line is 110 µeV, comparable to the one measured for a QD outside a cavity. This might tell us that the broad linewidth is a feature of the as-grown sample and not a degradation induced by the cavity processing and by the proximity of the QDs to etched surfaces. The graph in the inset of Fig. 4.24(a) shows the spectrum of a single QD outside the cavity, excited at X peak saturation with the same He-Ne laser. The spectrum has to be multiplied by a factor 139 to reach comparable peak intensity with respect to the QD inside the cavity. The polarization study of the X peak is shown in panel (b) of the same figure. The small polarization of the peak (the degree of polarization is 0.06) suggests a nearly perfect placement of the cavity around the QD. The 9 µeV FSS is larger than the usual values found in this kind of QDs but on the same order of magnitude, suggesting that an eventual pre-stress exerted on the sample (a feature that we usually observe in semiconductor-piezoelectric devices) is not dramatic and

can be in principle compensated with external strain tuning.

The mode mismatch reduced the enhancement of the emission properties in terms of brightness. With an integrated peak intensity of 144'000 cps, this QD is near the average values found with the DBR sample in combination with a SIL. The results shown suggest that with a better alignment of the cavity exceptional values of brightness could be reached. The estimated value of the extraction efficiency of the QD in the bulk membrane ($\sim 0.05\%$) is exceptionally low. This observation cast some doubts to the real extraction efficiency of the QD inside the cavity and a precise calculation of the extraction efficiency of optimized cavities is in order.

Strain tuning

After characterizing the optical emission of the QD in the cavities we switch to the strain tuning. Each pair of facing legs is addressed separately, in this initial characterization, performing a $\Delta V = 600\,\mathrm{V}$ sweep from $-200\,\mathrm{V}$ to $400\,\mathrm{V}$. The sweep is performed while acquiring the PL spectrum of the QD in steps of $1\,\mathrm{V}$. The energy of the X emission peak in a cycled voltage sweep versus the applied voltage is shown in Fig. 4.25, for each pair of legs. The vertical scale of the three graphs is the same, to better appreciate the different magnitudes of the shift along the three different directions.

The three graphs show a clear and reproducible shift of the X line with voltage, with the peak going back and forth as the voltage is increased and decreased. The magnitude of the shift is $-18\,\mu\mathrm{eV}$ for the pair of legs 1-4 and 2-5 while a higher shift of $59\,\mu\mathrm{eV}$ in the opposite direction is measured for legs 3-6. Similar results hold for another QD in a cavity in the first neighbor marker field with measured shifts of $-23\,\mu\mathrm{eV}$, $-8\,\mu\mathrm{eV}$ and $54\,\mu\mathrm{eV}$ for legs 1-4, 2-5, and 3-6 respectively. If we repeat the same measurement in a cavity which is $180\,\mu\mathrm{m}$ far from the center of the six legs, and outside the central gap, the amount of tuning decreases, with measured shifts of $-13\,\mu\mathrm{eV}$, $-3\,\mu\mathrm{eV}$ and $9\,\mu\mathrm{eV}$ for legs 1-4, 2-5, and 3-6 respectively.

We also performed polarization-resolved measurements and observed that the FSS of the QD does not show a clear trend with the voltage as the observed variations are comparable with the measurement error.

While these are very preliminary measurements on one of the very first fabricated devices, several important points can be noticed. We start out considering that the piezoelectric actuator is poled in such a way that a positive voltage should lead to a contraction of the piezo legs and, as a consequence, a tensile quasi-uniaxial stress on the overlying membrane. In turn this should produce a redshift of the QD emission lines. The fact that different legs produce shift in opposite directions strongly suggest that, despite its thickness, the membrane at center of the device

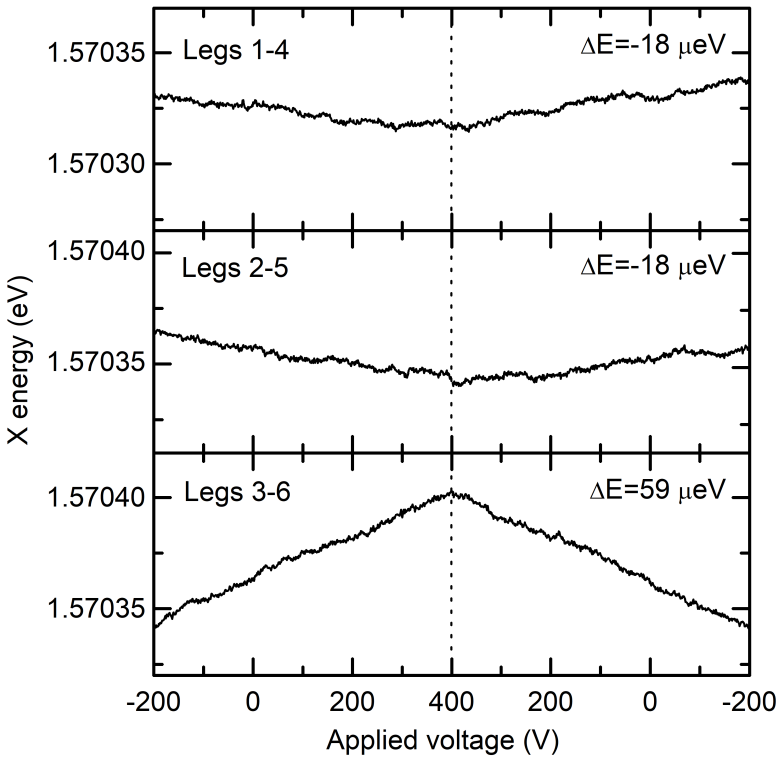

Figure 4.25. Energy shift of the X emission line of a QD in the center of a positioned CBR when applying high voltages to the three pair of legs of the micromachined piezo-device.

could be bent and/or could be in a strongly anisotropic strain status. This behavior was indeed observed in the past when wrinkles were occurring in very thin membrane (thickness of the order of 100 nm) bonded onto micro-machined piezos (see Ref. [49]). We also notice that the magnitude of the energy shift is very modest as compared to previous devices [49, 151]. This information (related to the induced hydrostatic stress) combined with almost absent tuning of the FSS with voltage (related to the induced anisotropic stress), strongly suggests an inefficient strain transfer from the piezoelectric actuator to the membrane. This is probably related to the thickness of the membrane and to related strain relaxation and/or a non-perfect adhesion of the membrane to the piezo actuator [154].

A possible approach to address this issue is to reduce the thickness of the membrane down to 30 µm when lapping the sample, or even bonding the thin sample directly to a micromachined device before the wet-etching steps. While the latter approach is very suggestive, membrane curling could occur, thus creating issues in the processing of the photonic cavities. We leave these points to future studies.

Chapter 5

Conclusions and outlook

In this thesis we have reported our efforts in the experimental demonstration of the suitability of QDs as non-classical light sources in future quantum networks. This thesis summarizes the work of the three years of my Ph.D. in the Nanophotonics group of the Physics Department of Sapienza University of Rome. My doctorate experience started in 2017 with Prof. Trotta and an empty room, soon to be turned into a laboratory, see Fig. 5.1. Together with the whole group (which grew with the addition of Dr. D. Tedeschi and Dr. F. Basso Basset) the first nine months of my Ph.D. were devoted to planning the new lab, installing all the equipment, testing it, and building the setup for the first experiments.

Figure 5.1. Pictures of the main room of the Nanophotonics laboratories at the Physics Department of Sapienza right after the beginning of the renovation in December of 2017 (left) and at the beginning of the experiments in May of 2018 (right). Courtesy of Prof. R. Trotta.

In the first two Chapters of this thesis we have described the theory of the two teleportation protocols for ideal photon sources and described the main features of the light emission from QDs. In the third Chapter we developed a model of the teleportation protocols that takes into account the figures of merit of the source and the characteristics of the experimental setup. We described the experimental framework used to both characterize the source and perform the experiments in

the lab and presented the demonstration of successful teleportation protocols. By simulating the results with the theoretical model we developed, we highlighted the improvements in the light source needed to reach efficiency and fidelity of the protocols to make QDs competitive with other well established technologies.

With these information at hand we shifted our attention on tackling the current limitations of QD entangled photon sources. We decided to follow the path of optical cavities, choosing one that best matched the characteristics we were looking for, i.e., the circular Bragg resonator. In the fourth Chapter, we described the fabrication of the cavities following all the steps from the QD sample design, to the membrane etching and bonding to the piezoelectric actuator, the design of the QD position imaging system, until the etching of the cavities and the optical characterization of the very first samples.

We achieved encouraging results in terms of source brightness and energy tunability, with much room for improvement. Optimistically, this suggests that soon we will have in our hands a source capable of unlocking a series of experiments and technological breakthroughs in the field of semiconductor QDs. Among the list of foreseeable applications, we decided to briefly describe two of them in this last Chapter, namely quantum protocols with remote emitters and quantum key distribution.

5.1 Quantum protocols with remote emitters

There is still much work to do to transfer the state and entanglement teleportation protocols outside the walls of a scientific laboratory, but the first step toward this goal is to demonstrate the same protocols using two remote sources instead of a single doubly-excited QD, as required to build up a QD-based quantum network. In the particular case of entanglement distribution in a quantum repeater described in Section 1.1, we would need several entangled-light emitters distributed along the distance between the two receiving end nodes. Each node will have to interface with other nodes and various elements in the network, setting strict requirements on the quality of the photon source.

The core of the entanglement distribution is the measurement of a two-photon Bell state and to achieve a high teleportation fidelity, photons must be indistinguishable in all degrees of freedom. When dealing with remote emitters, we introduce additional independent sources of dephasing, which ruin the indistinguishability of photons. Moreover, the two QDs must emit photons at the exact same energy so that the possibility to tune the emission of the QD while keeping the FSS at zero will be essential. Indeed, the striking features of photons emitted by self-assembled QDs

come with the drawback of being statistically distributed in an energy band which is usually three orders of magnitude larger then the natural linewidth of the emission line, so that there is almost no QD with an identical peer. This drawback can be efficiently addressed with the tuning of the optical properties of single QDs [47, 48, 155–160]. Strain-tuning, in particular, allowed for the highest two-photon interference visibility between photons emitted by a two-photon cascade in two remote QDs [48] without any temporal and spectral post-selection. The HOM visibility reported in the work of Reindl *et al.* [48] peaks at a $51 \pm 5\%$, a value mostly limited by a non perfect indistinguishability of the starting two sources as confirmed by a simulated maximum value of 56% using the measured parameters from the two QDs [156].

Strain tuning also allows for the control of the QD energy while maintaining the FSS to zero [64], enabling for high entanglement fidelity and high indistinguishability from remote sources at the same time. While two-photons interference from remote entangled photons sources still has to be demonstrated, strain tuning was used to interface the emission of a single QD with narrow-band atomic vapors [49].

As we explained in Chapter 2, the enhancement of the spontaneous emission in a QD can help reducing the detrimental effect on the indistinguishability of the emitted photons. Resorting to cavity-induced Purcell enhancement to alleviate the low indistinguishability of remote sources was already demonstrated for micropillars cavities [156]. Here, a value of 40(4) % was obtained for single-photons emitted from two remote QDs with a starting visibility of 75(5) % and 19(15) % while the matching of the energy of the QDs was obtained via temperature tuning. The high Purcell enhancement on only one of the two sources already increases the value of remote indistinguishability by relaxing the energy and mode matching requests on the second source, featuring a lower indistinguishability.

In the case of entangled-photon emission from QDs, the situation of the indistinguishability of photons gets more complicated as we need to combine the detrimental effect of the two-photon cascade time jittering with the dephasing effects affecting the single photons. As we explained earlier, the intrinsic time jittering of the two-photon cascade at the base of the entangled photon pair generation induces a degradation of the indistinguishability of both the X and XX photons. This can be predicted from the lifetimes of the transitions to be [85]:

$$M_{casc} = \frac{1}{1 + T_{1,XX}/T_{1,X}} \tag{5.1}$$

For droplet etched GaAs QDs, a ratio of the lifetimes $T_{1,XX}/T_{1,X} = 1/2$ is usually observed due to homogeneous density of states and an oscillator strength which depends weakly on the binding energy. The maximum reachable value of indistin-

guishability is thus 66.7%, in good agreement with experimental observations. If we resort to Purcell enhancement, we can further decrease the ratio $T_{1,XX}/T_{1,X}$ by giving different Purcell factors to the XX and X lines. This can be done by tuning the cavity at the optimal wavelength with respect to the QD emission. For Al_2O_3 oxide backed CBRs, simulated Fig. 4.3(b), with 140 nm oxide thickness, the maximum achievable ratio in Purcell enhancements between the XX and X transitions is ~ 3, which would lead to a value of the indistinguishability from the same source of 85.7%. The indistinguishability value of 90% reported for GaAs QDs in CBRs [39] agree quite well with this calculation, even thought the measured lifetimes of the transitions (36 ps for the XX and 60 ps for the X) would return an indistinguishability of only 62.5%. This discrepancy is not yet explained, leaving new ground for future research.

The detrimental effect of the cascade has to be summed to the single photon decoherence effects mentioned before. If we imagine of combining two QDs in CBRs with the exact same characteristics we can make use of a very simple formula, taking into account only the lifetime of the transition T_1 and the pure dephasing time T_2^* [120]:

$$M^* = \frac{1}{1 + 2T_1/T_2^*} \tag{5.2}$$

By taking a pure dephasing time of 500 ps as obtained for this same type of QDs [48] and the measured value of the lifetime of the X transition as 36 ps, we obtain a value for the indistinguishability of 87.4%. In a first approximation, we can estimate the value of the combined indistinguishability as the product of the two indistinguishabilities M_{casc} and M^*, which returns a value for remote CBR QDs of 74.9%. This value, combined with a close to one entanglement fidelity of the two-photon state would push the fidelity of the entanglement teleportation protocol to values above 0.8, when using a 50% BSM.

Other secondary issues remain to be tackled to optimize the two-photon interference from remote sources. Independent blinking of the sources introduces a detrimental effect by reducing the number of coincidences and unbalancing the counts from the two channels [74, 161]. Regarding the simultaneous excitation of the QDs with the same laser, a phonon-assisted excitation scheme can be used to circumvent possible issues due to a different XX binding energy and consequently a different excitation energy for the TPE excitation scheme if using the same excitation laser [48].

5.2 Quantum key distribution with quantum dots

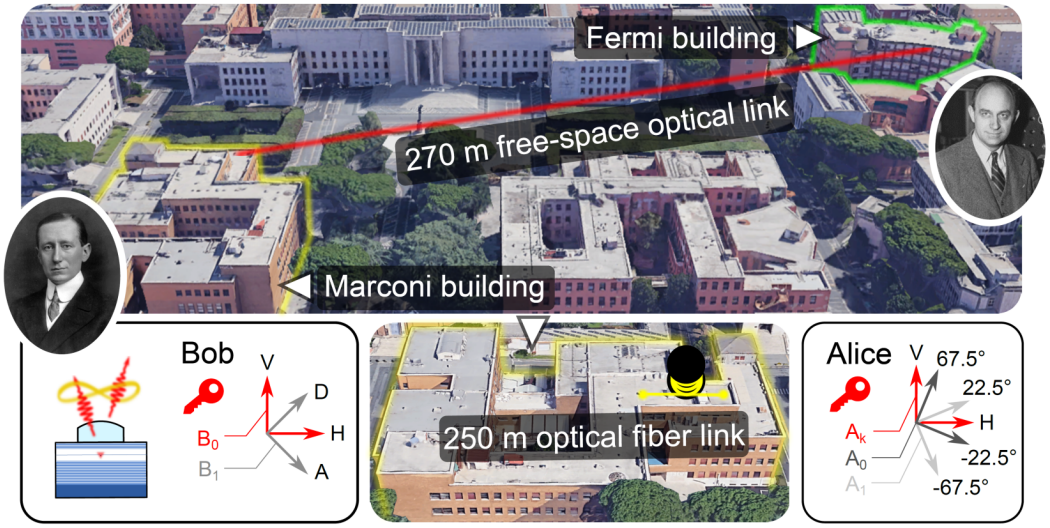

Figure 5.2. Principles of the quantum key distribution protocol performed with entangled light from a single GaAs QD and overview of the optical links used in the experiment. Entangled photon pairs are shared across the Sapienza University campus in Rome over a 270 m free-space distance and, in addition, between two laboratories in the same building via a 250 m single mode fiber. The entangled-light source is at the location of Bob which generates an entangled pair. He performs a measurement on one of the two photons of the pair on a random choice of two polarization bases $\{B_0, B_1\}$ and sends the other to Alice. She measures the polarization state of the photons she receives on a random choice of three polarization bases $\{A_k, A_0, A_1\}$. The joint measurement on the bases $\{B_0, A_k\}$ is used to share the key, while the results on some combinations of the remaining bases verify the entanglement quality by measuring the Bell parameter of the two-photon state. Aerial pictures from Google Earth. From. Ref. [162].

To better evaluate the real potential of QD sources it is interesting to start to see how they behave outside the optical laboratory. In parallel with the improvement of the quantum light source, we decided to exploit the same QD source that successfully demonstrated the entanglement teleportation to perform a QKD with a modified Ekert91 protocol [4, 163]. The experiment was performed via two different communication channels: a free-space 270 m long channel across the University campus and a 250 m long single mode fiber between two laboratories in the same building [162], see Fig. 5.2.

The experiment exploits the entangled pairs of photons emitted by a single QD to perform joint measurements of polarization on two sets of randomly chosen polarization bases. The result of the measurements is used to share a secret key between two locations that we indicate with the usual names of Alice and Bob. The QD stays at Bob location, who generates an entangled pair, keeps one of the

two photons and sends the other to Alice. He measures the polarization of the photon in one of the bases in the set $\{B_0, B_1\}$ choosing randomly, see Fig. 5.2. Alice measures the polarization of the received photon in a randomly chosen base in the set $\{A_k, A_0, A_1\}$. Later on, they share in a public channel the choice of bases they made. The results of the measurement in the parallel bases $\{A_k, B_0\}$ (statistically a quarter of the cases) are used to share the key, while the other pairs are used to measure the Bell parameter and ensure the entanglement quality throughout the experiment and thus the security of the communication. The resulting raw key exchange rate was $486\,\mathrm{bit\,s^{-1}}$ and the quantum bit error rate (QBER) $3.37(2)\,\%$ for the fiber channel. The free-space channel resulted in a raw key exchange rate $60\,\mathrm{bit\,s^{-1}}$ with a QBER of $4.0(2)\,\%$. The QBER values is consistently below the critical value of 11% [163] and the measured Bell parameter is above the classical threshold for both the channels.

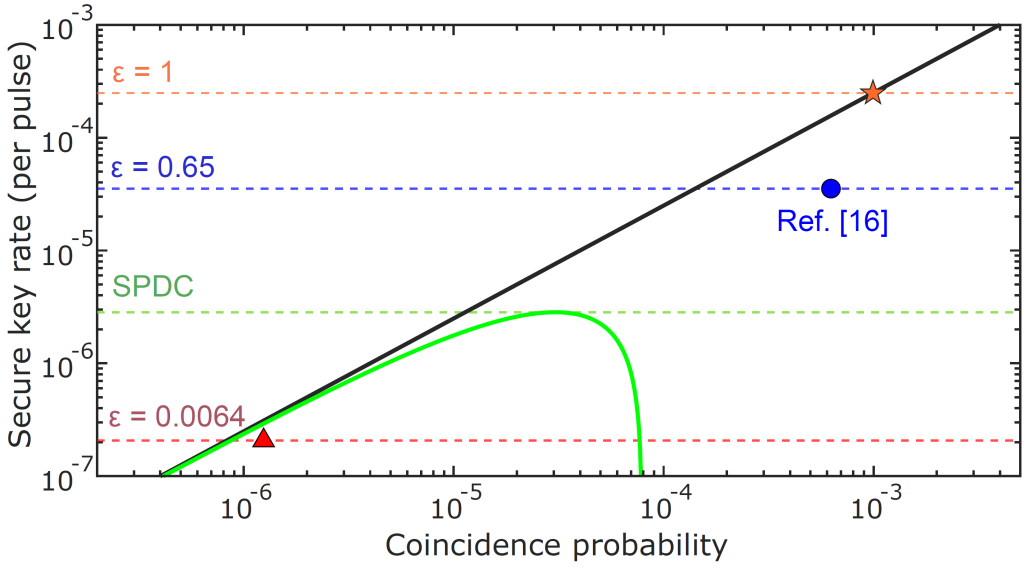

Figure 5.3. Secure key rate versus the total coincidence probability per pump pulse. The secure key rates are simulated for different entangled photon sources in a realistic implementation with the same losses as our free space optical link demonstration. The solid lines correspond to an ideal QD (black) and a realistic high-efficiency SPDC (green line) [164]. The dashed lines mark the respective maximum achievable secure key rate. In addition to the perfect emitter with a photon-pair collection rate ϵ at the first lens equal to 1 (orange star), we report the QD we use in the free-space experiment with $\epsilon = 0.0064$ (red triangle) and a CBR QD source with $\epsilon = 0.65$ [39] (blue circle). From. Ref. [162].

The successful demonstration of a QKD protocol with our GaAs QDs represented also the occasion to compare our result with the standard source of entangled photon pairs, i.e., SPDCs. By using an accepted model [165] of the key rate versus the coincidence probability of different sources of entangled light in a realistic lossy

channel (like the one we used), we can set the threshold where an improved QD source could surpass SPDCs in terms of efficiency of exchange of data. By looking at Fig. 5.3, we can see how a realistic SPDC source [164] (green line) reaches a maximum key exchange rate after which the multiphoton emission starts to play a major detrimental role in the error rate of the protocol. QDs instead, thanks to their intrinsically low multiphoton emission which is independent from the coincidence probability, are expected to show a linear behavior (black line). The value reached in our the experiment (red triangle) is currently below the SPDC performance but, by using the parameters from the CBR in literature (blue circle), with a pair extraction efficiency of 0.65 [39] we would surpass the performances of non-linear crystals for the realistic conditions (namely the overall signal attenuation) of our experimental realization. It is interesting to remark that the difference in performances is the heavier, the bigger are the losses in the channel [165, 166], raising QDs as potentially best sources in long distance communication, where losses are unavoidable.

For this reason, this application would be ideal to demonstrate the advantages of the device described in Chapter 4 and we expect that this goal could be reached in the near future.

Bibliography

[1] E. Rescorla and T. Dierks, *The transport layer security (tls) protocol version 1.3*, tech. rep. (RFC Editor, 2018).

[2] P. Shor, "Algorithms for quantum computation: discrete logarithms and factoring", in Proceedings 35th Annual Symposium on Foundations of Computer Science (1994), pp. 124–134.

[3] C. H. Bennett and G. Brassard, "Quantum cryptography: Public key distribution and coin tossing", Proceedings of the International Conference on Computers, Systems and Signal Processing (1984).

[4] A. K. Ekert, "Quantum cryptography based on Bell's theorem", Physical Review Letters **67**, 661–663 (1991).

[5] F. Flamini, N. Spagnolo, and F. Sciarrino, "Photonic quantum information processing: a review", Reports on Progress in Physics **82**, 016001 (2019).

[6] E. Systems, *Free space optics 10 gigabits el-10g*, `http://www.ecsystem.cz/en/products/free-space-optic-equipment/free-space-optics-10-gbps` (visited on 01/30/2021).

[7] Y. Kawaguchi, Y. Tamura, T. Haruna, Y. Yamamoto, and M. Hirano, "Ultra low-loss pure silica core fiber", SEI Technical review **80**, 50–55 (2015).

[8] K. Nagayama, M. Kakui, M. Matsui, T. Saitoh, and Y. Chigusa, "Ultra-low-loss (0.1484 dB/km) pure silica core fibre and extension of transmission distance", Electronics Letters **38**, 1168 (2002).

[9] W. K. Wootters and W. H. Zurek, "A single quantum cannot be cloned", Nature **299**, 802–803 (1982).

[10] N. Sangouard, C. Simon, H. de Riedmatten, and N. Gisin, "Quantum repeaters based on atomic ensembles and linear optics", Reviews of Modern Physics **83**, 33–80 (2011).

[11] N. Gisin and R. Thew, "Quantum communication", Nature Photonics **1**, 165–171 (2007).

[12] C. Simon, M. Afzelius, J. Appel, A. Boyer de la Giroday, S. J. Dewhurst, N. Gisin, C. Y. Hu, F. Jelezko, S. Kröll, J. H. Müller, J. Nunn, E. S. Polzik, J. G. Rarity, H. De Riedmatten, W. Rosenfeld, A. J. Shields, N. Sköld, R. M. Stevenson, R. Thew, I. A. Walmsley, M. C. Weber, H. Weinfurter, J. Wrachtrup, and R. J. Young, "Quantum memories: A review based on the European integrated project "Qubit Applications (QAP)"", The European Physical Journal D **58**, 1–22 (2010).

[13] K. Azuma, K. Tamaki, and H.-K. Lo, "All-photonic quantum repeaters", Nature Communications **6**, 6787 (2015).

[14] Z.-D. Li, R. Zhang, X.-F. Yin, L.-Z. Liu, Y. Hu, Y.-Q. Fang, Y.-Y. Fei, X. Jiang, J. Zhang, L. Li, N.-L. Liu, F. Xu, Y.-A. Chen, and J.-W. Pan, "Experimental quantum repeater without quantum memory", Nature Photonics **13**, 644–648 (2019).

[15] J. S. Bell, *Speakable and unspeakable in quantum mechanics: collected papers on quantum philosophy* (Cambridge University Press, Cambridge [Cambridgeshire] ; New York, 1987).

[16] A. Einstein, B. Podolsky, and N. Rosen, "Can Quantum-Mechanical Description of Physical Reality Be Considered Complete?", Physical Review **47**, 777–780 (1935).

[17] D. Bohm, *Quantum theory*, 16. print, Prentice-Hall physics series, OCLC: 256663000 (Prentice-Hall, Englewood Cliffs, N. J, 1951).

[18] J. S. Bell, "On the Einstein Podolsky Rosen paradox", Physics Physique Fizika **1**, 195–200 (1964).

[19] A. Aspect, P. Grangier, and G. Roger, "Experimental Tests of Realistic Local Theories via Bell's Theorem", Physical Review Letters **47**, 460–463 (1981).

[20] A. Aspect, P. Grangier, and G. Roger, "Experimental Realization of Einstein-Podolsky-Rosen-Bohm *Gedankenexperiment* : A New Violation of Bell's Inequalities", Physical Review Letters **49**, 91–94 (1982).

[21] A. Aspect, J. Dalibard, and G. Roger, "Experimental Test of Bell's Inequalities Using Time- Varying Analyzers", Physical Review Letters **49**, 1804–1807 (1982).

[22] B. Hensen, H. Bernien, A. E. Dréau, A. Reiserer, N. Kalb, M. S. Blok, J. Ruitenberg, R. F. L. Vermeulen, R. N. Schouten, C. Abellán, W. Amaya, V. Pruneri, M. W. Mitchell, M. Markham, D. J. Twitchen, D. Elkouss, S. Wehner, T. H. Taminiau, and R. Hanson, "Loophole-free Bell inequality violation using electron spins separated by 1.3 kilometres", Nature **526**, 682–686 (2015).

[23] M. Giustina, M. A. M. Versteegh, S. Wengerowsky, J. Handsteiner, A. Hochrainer, K. Phelan, F. Steinlechner, J. Kofler, J.-Å. Larsson, C. Abellán, W. Amaya, V. Pruneri, M. W. Mitchell, J. Beyer, T. Gerrits, A. E. Lita, L. K. Shalm, S. W. Nam, T. Scheidl, R. Ursin, B. Wittmann, and A. Zeilinger, "Significant-Loophole-Free Test of Bell's Theorem with Entangled Photons", Physical Review Letters **115** (2015).

[24] H.-J. Briegel, W. Dür, J. I. Cirac, and P. Zoller, "Quantum Repeaters: The Role of Imperfect Local Operations in Quantum Communication", Physical Review Letters **81**, 5932–5935 (1998).

[25] M. Żukowski, A. Zeilinger, M. A. Horne, and A. K. Ekert, "'Event-ready-detectors'' Bell experiment via entanglement swapping", Physical Review Letters **71**, 4287–4290 (1993).

[26] C. H. Bennett, G. Brassard, C. Crépeau, R. Jozsa, A. Peres, and W. K. Wootters, "Teleporting an unknown quantum state via dual classical and Einstein-Podolsky-Rosen channels", Physical Review Letters **70**, 1895–1899 (1993).

[27] C. K. Hong, Z. Y. Ou, and L. Mandel, "Measurement of subpicosecond time intervals between two photons by interference", Physical Review Letters **59**, 2044–2046 (1987).

[28] T. B. Pittman, D. V. Strekalov, A. Migdall, M. H. Rubin, A. V. Sergienko, and Y. H. Shih, "Can Two-Photon Interference be Considered the Interference of Two Photons?", Physical Review Letters **77**, 1917–1920 (1996).

[29] G. Weihs and A. Zeilinger, in *Coherence and statistics of photons and atoms*, edited by J. Peřina, Wiley series in lasers and applications (Wiley, New York, 2001), pp. 262–288.

[30] Y.-H. Kim, S. P. Kulik, and Y. Shih, "Quantum Teleportation of a Polarization State with a Complete Bell State Measurement", Physical Review Letters **86**, 1370–1373 (2001).

[31] V. Scarani, H. de Riedmatten, I. Marcikic, H. Zbinden, and N. Gisin, "Four-photon correction in two-photon Bell experiments", The European Physical Journal D **32**, 129–138 (2005).

[32] X.-L. Wang, L.-K. Chen, W. Li, H.-L. Huang, C. Liu, C. Chen, Y.-H. Luo, Z.-E. Su, D. Wu, Z.-D. Li, H. Lu, Y. Hu, X. Jiang, C.-Z. Peng, L. Li, N.-L. Liu, Y.-A. Chen, C.-Y. Lu, and J.-W. Pan, "Experimental Ten-Photon Entanglement", Physical Review Letters **117** (2016).

[33] I. Aharonovich, D. Englund, and M. Toth, "Solid-state single-photon emitters", Nature Photonics **10**, 631–641 (2016).

[34] P. Senellart, G. Solomon, and A. White, "High-performance semiconductor quantum-dot single-photon sources", Nature Nanotechnology **12**, 1026–1039 (2017).

[35] O. Benson, C. Santori, M. Pelton, and Y. Yamamoto, "Regulated and Entangled Photons from a Single Quantum Dot", Physical Review Letters **84**, 2513–2516 (2000).

[36] D. Huber, M. Reindl, J. Aberl, A. Rastelli, and R. Trotta, "Semiconductor quantum dots as an ideal source of polarization-entangled photon pairs on-demand: a review", Journal of Optics **20**, 073002 (2018).

[37] M. Müller, S. Bounouar, K. D. Jöns, M. Glässl, and P. Michler, "On-demand generation of indistinguishable polarization-entangled photon pairs", Nature Photonics **8**, 224–228 (2014).

[38] L. Schweickert, K. D. Jöns, K. D. Zeuner, S. F. Covre da Silva, H. Huang, T. Lettner, M. Reindl, J. Zichi, R. Trotta, A. Rastelli, and V. Zwiller, "On-demand generation of background-free single photons from a solid-state source", Applied Physics Letters **112**, 093106 (2018).

[39] J. Liu, R. Su, Y. Wei, B. Yao, S. F. C. d. Silva, Y. Yu, J. Iles-Smith, K. Srinivasan, A. Rastelli, J. Li, and X. Wang, "A solid-state source of strongly entangled photon pairs with high brightness and indistinguishability", Nature Nanotechnology **14**, 586–593 (2019).

[40] H. Wang, H. Hu, T.-H. Chung, J. Qin, X. Yang, J.-P. Li, R.-Z. Liu, H.-S. Zhong, Y.-M. He, X. Ding, Y.-H. Deng, Q. Dai, Y.-H. Huo, S. Höfling, C.-Y. Lu, and J.-W. Pan, "On-Demand Semiconductor Source of Entangled Photons Which Simultaneously Has High Fidelity, Efficiency, and Indistinguishability", Physical Review Letters **122**, 113602 (2019).

[41] D. Huber, M. Reindl, Y. Huo, H. Huang, J. S. Wildmann, O. G. Schmidt, A. Rastelli, and R. Trotta, "Highly indistinguishable and strongly entangled photons from symmetric GaAs quantum dots", Nature Communications **8**, 15506 (2017).

[42] D. Huber, M. Reindl, S. F. Covre da Silva, C. Schimpf, J. Martín-Sánchez, H. Huang, G. Piredda, J. Edlinger, A. Rastelli, and R. Trotta, "Strain-Tunable GaAs Quantum Dot: A Nearly Dephasing-Free Source of Entangled Photon Pairs on Demand", Physical Review Letters **121**, 033902 (2018).

[43] C. L. Salter, R. M. Stevenson, I. Farrer, C. A. Nicoll, D. A. Ritchie, and A. J. Shields, "An entangled-light-emitting diode", Nature **465**, 594–597 (2010).

[44] J. Zhang, J. S. Wildmann, F. Ding, R. Trotta, Y. Huo, E. Zallo, D. Huber, A. Rastelli, and O. G. Schmidt, "High yield and ultrafast sources of electrically triggered entangled-photon pairs based on strain-tunable quantum dots", Nature Communications **6**, 10067 (2015).

[45] T. H. Chung, G. Juska, S. T. Moroni, A. Pescaglini, A. Gocalinska, and E. Pelucchi, "Selective carrier injection into patterned arrays of pyramidal quantum dots for entangled photon light-emitting diodes", Nature Photonics **10**, 782–787 (2016).

[46] R. Trotta, P. Atkinson, J. D. Plumhof, E. Zallo, R. O. Rezaev, S. Kumar, S. Baunack, J. R. Schröter, A. Rastelli, and O. G. Schmidt, "Nanomembrane Quantum-Light-Emitting Diodes Integrated onto Piezoelectric Actuators", Advanced Materials **24**, 2668–2672 (2012).

[47] E. Flagg, A. Muller, S. Polyakov, A. Ling, A. Migdall, and G. Solomon, "Interference of Single Photons from Two Separate Semiconductor Quantum Dots", Physical Review Letters **104**, 137401 (2010).

[48] M. Reindl, K. D. Jöns, D. Huber, C. Schimpf, Y. Huo, V. Zwiller, A. Rastelli, and R. Trotta, "Phonon-Assisted Two-Photon Interference from Remote Quantum Emitters", Nano Letters **17**, 4090–4095 (2017).

[49] R. Trotta, J. Martín-Sánchez, J. S. Wildmann, G. Piredda, M. Reindl, C. Schimpf, E. Zallo, S. Stroj, J. Edlinger, and A. Rastelli, "Wavelength-tunable sources of entangled photons interfaced with atomic vapours", Nature Communications **7**, 10375 (2016).

[50] J. Nilsson, R. M. Stevenson, K. H. A. Chan, J. Skiba-Szymanska, M. Lucamarini, M. B. Ward, A. J. Bennett, C. L. Salter, I. Farrer, D. A. Ritchie, and A. J. Shields, "Quantum teleportation using a light-emitting diode", Nature Photonics **7**, 311–315 (2013).

[51] J. Huwer, R. M. Stevenson, J. Skiba-Szymanska, M. B. Ward, A. J. Shields, M. Felle, I. Farrer, D. A. Ritchie, and R. V. Penty, "Quantum-Dot-Based Telecommunication-Wavelength Quantum Relay", Physical Review Applied **8**, 024007 (2017).

[52] M. Reindl, D. Huber, C. Schimpf, S. F. C. da Silva, M. B. Rota, H. Huang, V. Zwiller, K. D. Jöns, A. Rastelli, and R. Trotta, "All-photonic quantum teleportation using on-demand solid-state quantum emitters", Science Advances **4**, eaau1255 (2018).

[53] F. Basso Basset, M. B. Rota, C. Schimpf, D. Tedeschi, K. D. Zeuner, S. F. Covre da Silva, M. Reindl, V. Zwiller, K. D. Jöns, A. Rastelli, and R. Trotta, "Entanglement Swapping with Photons Generated on Demand by a Quantum Dot", Physical Review Letters **123**, 160501 (2019).

[54] M. Zopf, R. Keil, Y. Chen, J. Yang, D. Chen, F. Ding, and O. G. Schmidt, "Entanglement Swapping with Semiconductor-Generated Photons Violates Bell's Inequality", Physical Review Letters **123**, 160502 (2019).

[55] I. Vurgaftman, J. R. Meyer, and L. R. Ram-Mohan, "Band parameters for III–V compound semiconductors and their alloys", Journal of Applied Physics **89**, 5815–5875 (2001).

[56] G. Dresselhaus, "Effective mass approximation for excitons", Journal of Physics and Chemistry of Solids **1**, 14–22 (1956).

[57] J. H. Davies, *The Physics of Low-dimensional Semiconductors: An Introduction*, 1st ed. (Cambridge University Press, Dec. 1997).

[58] A. Schliwa, M. Winkelnkemper, and D. Bimberg, "Few-particle energies versus geometry and composition of $In_xGa_{1-x}As/GaAs$ self-organized quantum dots", Physical Review B **79**, 075443 (2009).

[59] J.-W. Luo and A. Zunger, "Geometry of epitaxial GaAs/(Al,Ga)As quantum dots as seen by excitonic spectroscopy", Physical Review B **84**, 235317 (2011).

[60] R. Trotta, E. Zallo, E. Magerl, O. G. Schmidt, and A. Rastelli, "Independent control of exciton and biexciton energies in single quantum dots via electroelastic fields", Physical Review B **88**, 155312 (2013).

[61] D. F. V. James, P. G. Kwiat, W. J. Munro, and A. G. White, "Measurement of qubits", Physical Review A **64**, 052312 (2001).

[62] R. Trotta, J. S. Wildmann, E. Zallo, O. G. Schmidt, and A. Rastelli, "Highly Entangled Photons from Hybrid Piezoelectric-Semiconductor Quantum Dot Devices", Nano Letters **14**, 3439–3444 (2014).

[63] M. Bayer, G. Ortner, O. Stern, A. Kuther, A. A. Gorbunov, A. Forchel, P. Hawrylak, S. Fafard, K. Hinzer, T. L. Reinecke, S. N. Walck, J. P. Reithmaier, F. Klopf, and F. Schäfer, "Fine structure of neutral and charged excitons in self-assembled In(Ga)As/(Al)GaAs quantum dots", Physical Review B **65**, 195315 (2002).

[64] R. Trotta, J. Martín-Sánchez, I. Daruka, C. Ortix, and A. Rastelli, "Energy-Tunable Sources of Entangled Photons: A Viable Concept for Solid-State-Based Quantum Relays", Physical Review Letters **114**, 150502 (2015).

[65] A. Fognini, A. Ahmadi, M. Zeeshan, J. T. Fokkens, S. J. Gibson, N. Sherlekar, S. J. Daley, D. Dalacu, P. J. Poole, K. D. Jöns, V. Zwiller, and M. E. Reimer, "Dephasing Free Photon Entanglement with a Quantum Dot", ACS Photonics **6**, 1656–1663 (2019).

[66] M. Gong, B. Hofer, E. Zallo, R. Trotta, J.-W. Luo, O. G. Schmidt, and C. Zhang, "Statistical properties of exciton fine structure splitting and polarization angles in quantum dot ensembles", Physical Review B **89**, 205312 (2014).

[67] B. D. Gerardot, S. Seidl, P. A. Dalgarno, R. J. Warburton, D. Granados, J. M. Garcia, K. Kowalik, O. Krebs, K. Karrai, A. Badolato, and P. M. Petroff, "Manipulating exciton fine structure in quantum dots with a lateral electric field", Applied Physics Letters **90**, 041101 (2007).

[68] M. M. Vogel, S. M. Ulrich, R. Hafenbrak, P. Michler, L. Wang, A. Rastelli, and O. G. Schmidt, "Influence of lateral electric fields on multiexcitonic transitions and fine structure of single quantum dots", Applied Physics Letters **91**, 051904 (2007).

[69] A. J. Bennett, M. A. Pooley, R. M. Stevenson, M. B. Ward, R. B. Patel, A. B. de la Giroday, N. Sköld, I. Farrer, C. A. Nicoll, D. A. Ritchie, and A. J. Shields, "Electric-field-induced coherent coupling of the exciton states in a single quantum dot", Nature Physics **6**, 947–950 (2010).

[70] A. J. Hudson, R. M. Stevenson, A. J. Bennett, R. J. Young, C. A. Nicoll, P. Atkinson, K. Cooper, D. A. Ritchie, and A. J. Shields, "Coherence of an Entangled Exciton-Photon State", Physical Review Letters **99**, 266802 (2007).

[71] A. Dousse, J. Suffczyński, A. Beveratos, O. Krebs, A. Lemaître, I. Sagnes, J. Bloch, P. Voisin, and P. Senellart, "Ultrabright source of entangled photon pairs", Nature **466**, 217–220 (2010).

[72] M. M. Weston, H. M. Chrzanowski, S. Wollmann, A. Boston, J. Ho, L. K. Shalm, V. B. Verma, M. S. Allman, S. W. Nam, R. B. Patel, S. Slussarenko, and G. J. Pryde, "Efficient and pure femtosecond-pulse-length source of polarization-entangled photons", Opt. Express **24**, 10869–10879 (2016).

[73] L. K. Shalm, E. Meyer-Scott, B. G. Christensen, P. Bierhorst, M. A. Wayne, M. J. Stevens, T. Gerrits, S. Glancy, D. R. Hamel, M. S. Allman, K. J. Coakley, S. D. Dyer, C. Hodge, A. E. Lita, V. B. Verma, C. Lambrocco, E. Tortorici, A. L. Migdall, Y. Zhang, D. R. Kumor, W. H. Farr, F. Marsili, M. D. Shaw, J. A. Stern, C. Abellán, W. Amaya, V. Pruneri, T. Jennewein, M. W. Mitchell, P. G. Kwiat, J. C. Bienfang, R. P. Mirin, E. Knill, and S. W.

Nam, "Strong loophole-free test of local realism", Physical Review Letters **115**, 250402 (2015).

[74] K. D. Jöns, K. Stensson, M. Reindl, M. Swillo, Y. Huo, V. Zwiller, A. Rastelli, R. Trotta, and G. Björk, "Two-photon interference from two blinking quantum emitters", Physical Review B **96**, 075430 (2017).

[75] C. Heyn, A. Stemmann, T. Köppen, C. Strelow, T. Kipp, M. Grave, S. Mendach, and W. Hansen, "Highly uniform and strain-free GaAs quantum dots fabricated by filling of self-assembled nanoholes", Applied Physics Letters **94**, 183113 (2009).

[76] Y. H. Huo, A. Rastelli, and O. G. Schmidt, "Ultra-small excitonic fine structure splitting in highly symmetric quantum dots on GaAs (001) substrate", Applied Physics Letters **102**, 152105 (2013).

[77] M. B. Rota, F. B. Basset, D. Tedeschi, and R. Trotta, "Entanglement Teleportation With Photons From Quantum Dots: Toward a Solid-State Based Quantum Network", IEEE Journal of Selected Topics in Quantum Electronics **26**, 1–16 (2020).

[78] H. Jayakumar, A. Predojević, T. Huber, T. Kauten, G. S. Solomon, and G. Weihs, "Deterministic Photon Pairs and Coherent Optical Control of a Single Quantum Dot", Physical Review Letters **110**, 135505 (2013).

[79] X. Ding, Y. He, Z.-C. Duan, N. Gregersen, M.-C. Chen, S. Unsleber, S. Maier, C. Schneider, M. Kamp, S. Höfling, C.-Y. Lu, and J.-W. Pan, "On-Demand Single Photons with High Extraction Efficiency and Near-Unity Indistinguishability from a Resonantly Driven Quantum Dot in a Micropillar", Physical Review Letters **116**, 020401 (2016).

[80] R. Hanbury Brown and R. Q. Twiss, "A Test of a New Type of Stellar Interferometer on Sirius", Nature **178**, 1046–1048 (1956).

[81] J.-P. Jahn, M. Munsch, L. Béguin, A. V. Kuhlmann, M. Renggli, Y. Huo, F. Ding, R. Trotta, M. Reindl, O. G. Schmidt, A. Rastelli, P. Treutlein, and R. J. Warburton, "An artificial Rb atom in a semiconductor with lifetime-limited linewidth", Physical Review B **92**, 245439 (2015).

[82] N. Somaschi, V. Giesz, L. De Santis, J. C. Loredo, M. P. Almeida, G. Hornecker, S. L. Portalupi, T. Grange, C. Antón, J. Demory, C. Gómez, I. Sagnes, N. D. Lanzillotti-Kimura, A. Lemaítre, A. Auffeves, A. G. White, L. Lanco, and P. Senellart, "Near-optimal single-photon sources in the solid state", Nature Photonics **10**, 340–345 (2016).

[83] T. Legero, T. Wilk, A. Kuhn, and G. Rempe, "Time-resolved two-photon quantum interference", Applied Physics B **77**, 797–802 (2003).

[84] E. Schöll, L. Hanschke, L. Schweickert, K. D. Zeuner, M. Reindl, S. F. Covre da Silva, T. Lettner, R. Trotta, J. J. Finley, K. Müller, A. Rastelli, V. Zwiller, and K. D. Jöns, "Resonance Fluorescence of GaAs Quantum Dots with Near-Unity Photon Indistinguishability", Nano Letters **19**, 2404–2410 (2019).

[85] C. Simon and J.-P. Poizat, "Creating Single Time-Bin-Entangled Photon Pairs", Physical Review Letters **94**, 030502 (2005).

[86] E. B. Flagg, S. V. Polyakov, T. Thomay, and G. S. Solomon, "Dynamics of Nonclassical Light from a Single Solid-State Quantum Emitter", Physical Review Letters **109** (2012).

[87] T. Huber, A. Predojević, H. Zoubi, H. Jayakumar, G. S. Solomon, and G. Weihs, "Measurement and modification of biexciton-exciton time correlations", Optics Express **21**, 9890 (2013).

[88] E. Schöll, L. Schweickert, L. Hanschke, K. D. Zeuner, F. Sbresny, T. Lettner, R. Trivedi, M. Reindl, S. F. Covre da Silva, R. Trotta, J. J. Finley, J. Vučković, K. Müller, A. Rastelli, V. Zwiller, and K. D. Jöns, "Crux of Using the Cascaded Emission of a Three-Level Quantum Ladder System to Generate Indistinguishable Photons", Physical Review Letters **125**, 233605 (2020).

[89] A. V. Kuhlmann, J. Houel, A. Ludwig, L. Greuter, D. Reuter, A. D. Wieck, M. Poggio, and R. J. Warburton, "Charge noise and spin noise in a semiconductor quantum device", Nature Phys **9**, 570–575 (2013).

[90] A. Thoma, P. Schnauber, M. Gschrey, M. Seifried, J. Wolters, J.-H. Schulze, A. Strittmatter, S. Rodt, A. Carmele, A. Knorr, T. Heindel, and S. Reitzenstein, "Exploring Dephasing of a Solid-State Quantum Emitter via Time- and Temperature-Dependent Hong-Ou-Mandel Experiments", Physical Review Letters **116** (2016).

[91] A. Reigue, J. Iles-Smith, F. Lux, L. Monniello, M. Bernard, F. Margaillan, A. Lemaitre, A. Martinez, D. P. S. McCutcheon, J. Mørk, R. Hostein, and V. Voliotis, "Probing Electron-Phonon Interaction through Two-Photon Interference in Resonantly Driven Semiconductor Quantum Dots", Physical Review Letters **118**, 233602 (2017).

[92] C. Schimpf, M. Reindl, P. Klenovský, T. Fromherz, S. F. Covre Da Silva, J. Hofer, C. Schneider, S. Höfling, R. Trotta, and A. Rastelli, "Resolving the temporal evolution of line broadening in single quantum emitters", Optics Express **27**, 35290 (2019).

[93] F. Basso Basset, F. Salusti, L. Schweickert, M. B. Rota, D. Tedeschi, S. F. Covre da Silva, E. Roccia, V. Zwiller, K. D. Jöns, A. Rastelli, and R. Trotta, "Quantum teleportation with imperfect quantum dots", npj Quantum Information **7**, 7 (2021).

[94] D. E. Aspnes, S. M. Kelso, R. A. Logan, and R. Bhat, "Optical properties of Al $_x$ Ga $_{1-x}$ As", Journal of Applied Physics **60**, 754–767 (1986).

[95] W. Barnes, G. Björk, J. Gérard, P. Jonsson, J. Wasey, P. Worthing, and V. Zwiller, "Solid-state single photon sources: light collection strategies", The European Physical Journal D - Atomic, Molecular and Optical Physics **18**, 197–210 (2002).

[96] H. Benisty, H. De Neve, and C. Weisbuch, "Impact of planar microcavity effects on light extraction-Part I: basic concepts and analytical trends", IEEE Journal of Quantum Electronics **34**, 1612–1631 (1998).

[97] Y. Ma, P. E. Kremer, and B. D. Gerardot, "Efficient photon extraction from a quantum dot in a broad-band planar cavity antenna", Journal of Applied Physics **115**, 023106 (2014).

[98] Y. Chen, M. Zopf, R. Keil, F. Ding, and O. G. Schmidt, "Highly-efficient extraction of entangled photons from quantum dots using a broadband optical antenna", Nature Communications **9** (2018).

[99] M. Gschrey, A. Thoma, P. Schnauber, M. Seifried, R. Schmidt, B. Wohlfeil, L. Krüger, J. .-H. Schulze, T. Heindel, S. Burger, F. Schmidt, A. Strittmatter, S. Rodt, and S. Reitzenstein, "Highly indistinguishable photons from deterministic quantum-dot microlenses utilizing three-dimensional in situ electron-beam lithography", Nature Communications **6**, 7662 (2015).

[100] O. Gazzano, S. Michaelis de Vasconcellos, C. Arnold, A. Nowak, E. Galopin, I. Sagnes, L. Lanco, A. Lemaître, and P. Senellart, "Bright solid-state sources of indistinguishable single photons", Nature Communications **4** (2013).

[101] M. Davanço, M. T. Rakher, D. Schuh, A. Badolato, and K. Srinivasan, "A circular dielectric grating for vertical extraction of single quantum dot emission", Applied Physics Letters **99**, 041102 (2011).

[102] J. Claudon, J. Bleuse, N. S. Malik, M. Bazin, P. Jaffrennou, N. Gregersen, C. Sauvan, P. Lalanne, and J.-M. Gérard, "A highly efficient single-photon source based on a quantum dot in a photonic nanowire", Nature Photonics **4**, 174–177 (2010).

[103] G. Bulgarini, M. E. Reimer, M. Bouwes Bavinck, K. D. Jöns, D. Dalacu, P. J. Poole, E. P. A. M. Bakkers, and V. Zwiller, "Nanowire Waveguides Launching Single Photons in a Gaussian Mode for Ideal Fiber Coupling", Nano Letters **14**, 4102–4106 (2014).

[104] P. Michler, A. Kiraz, L. Zhang, C. Becher, E. Hu, and A. Imamoglu, "Laser emission from quantum dots in microdisk structures", Applied Physics Letters **77**, 184–186 (2000).

[105] A. Badolato, "Deterministic Coupling of Single Quantum Dots to Single Nanocavity Modes", Science **308**, 1158–1161 (2005).

[106] E. M. Purcell, H. C. Torrey, and R. V. Pound, "Resonance Absorption by Nuclear Magnetic Moments in a Solid", Physical Review **69**, 37–38 (1946).

[107] S. Reitzenstein, "Semiconductor Quantum Dot–Microcavities for Quantum Optics in Solid State", IEEE Journal of Selected Topics in Quantum Electronics **18**, 1733–1746 (2012).

[108] J. P. Reithmaier, G. Sęk, A. Löffler, C. Hofmann, S. Kuhn, S. Reitzenstein, L. V. Keldysh, V. D. Kulakovskii, T. L. Reinecke, and A. Forchel, "Strong coupling in a single quantum dot–semiconductor microcavity system", Nature **432**, 197–200 (2004).

[109] S. M. Thon, M. T. Rakher, H. Kim, J. Gudat, W. T. M. Irvine, P. M. Petroff, and D. Bouwmeester, "Strong coupling through optical positioning of a quantum dot in a photonic crystal cavity", Applied Physics Letters **94**, 111115 (2009).

[110] J. Gérard, B. Sermage, B. Gayral, B. Legrand, E. Costard, and V. Thierry-Mieg, "Enhanced Spontaneous Emission by Quantum Boxes in a Monolithic Optical Microcavity", Physical Review Letters **81**, 1110–1113 (1998).

[111] D. Najer, I. Söllner, P. Sekatski, V. Dolique, M. C. Löbl, D. Riedel, R. Schott, S. Starosielec, S. R. Valentin, A. D. Wieck, N. Sangouard, A. Ludwig, and R. J. Warburton, "A gated quantum dot strongly coupled to an optical microcavity", Nature **575**, 622–627 (2019).

[112] J. Iles-Smith, D. P. S. McCutcheon, A. Nazir, and J. Mørk, "Phonon scattering inhibits simultaneous near-unity efficiency and indistinguishability in semiconductor single-photon sources", Nature Photonics **11**, 521–526 (2017).

[113] C. Gustin and S. Hughes, "Pulsed excitation dynamics in quantum-dot–cavity systems: Limits to optimizing the fidelity of on-demand single-photon sources", Physical Review B **98**, 045309 (2018).

[114] M. A. M. Versteegh, M. E. Reimer, K. D. Jöns, D. Dalacu, P. J. Poole, A. Gulinatti, A. Giudice, and V. Zwiller, "Observation of strongly entangled photon pairs from a nanowire quantum dot", Nature Communications **5**, 5298 (2014).

[115] T. Huber, A. Predojević, M. Khoshnegar, D. Dalacu, P. J. Poole, H. Majedi, and G. Weihs, "Polarization Entangled Photons from Quantum Dots Embedded in Nanowires", Nano Letters **14**, 7107–7114 (2014).

[116] N. Eriksson, M. Hagberg, and A. Larsson, "Highly directional grating outcouplers with tailorable radiation characteristics", IEEE Journal of Quantum Electronics **32**, 1038–1047 (1996).

[117] D. Taillaert, W. Bogaerts, P. Bienstman, T. F. Krauss, P. V. Daele, I. Moerman, S. Verstuyft, K. D. Mesel, and R. Baets, "An out-of-plane grating coupler for efficient butt-coupling between compact planar waveguides and single-mode fibers", IEEE Journal of Quantum Electronics **38**, 949–955 (2002).

[118] P. Tighineanu, C. L. Dreeßen, C. Flindt, P. Lodahl, and A. S. Sørensen, "Phonon Decoherence of Quantum Dots in Photonic Structures: Broadening of the Zero-Phonon Line and the Role of Dimensionality", Physical Review Letters **120**, 257401 (2018).

[119] C. Kammerer, G. Cassabois, C. Voisin, M. Perrin, C. Delalande, P. Roussignol, and J. M. Gérard, "Interferometric correlation spectroscopy in single quantum dots", Applied Physics Letters **81**, 2737–2739 (2002).

[120] J. Bylander, I. Robert-Philip, and I. Abram, "Interference and correlation of two independent photons", The European Physical Journal D **22**, 295–301 (2003).

[121] F. Troiani, "Entanglement swapping with energy-polarization-entangled photons from quantum dot cascade decay", Physical Review B **90**, 245419 (2014).

[122] C. Santori, D. Fattal, J. Vučković, G. S. Solomon, and Y. Yamamoto, "Indistinguishable photons from a single-photon device", Nature **419**, 594–597 (2002).

[123] B. Kambs and C. Becher, "Limitations on the indistinguishability of photons from remote solid state sources", New Journal of Physics **20**, 115003 (2018).

[124] B. T. Kirby, S. Santra, V. S. Malinovsky, and M. Brodsky, "Entanglement swapping of two arbitrarily degraded entangled states", Physical Review A **94**, 012336 (2016).

[125] R. M. Stevenson, A. J. Hudson, A. J. Bennett, R. J. Young, C. A. Nicoll, D. A. Ritchie, and A. J. Shields, "Evolution of Entanglement Between Distinguishable Light States", Physical Review Letters **101**, 170501 (2008).

[126] N. Lütkenhaus, J. Calsamiglia, and K.-A. Suominen, "Bell measurements for teleportation", Physical Review A **59**, 3295–3300 (1999).

[127] D. Boschi, S. Branca, F. De Martini, L. Hardy, and S. Popescu, "Experimental Realization of Teleporting an Unknown Pure Quantum State via Dual Classical and Einstein-Podolsky-Rosen Channels", Physical Review Letters **80**, 1121–1125 (1998).

[128] D. Bouwmeester, J.-W. Pan, K. Mattle, M. Eibl, H. Weinfurter, and A. Zeilinger, "Experimental quantum teleportation", Nature **390**, 575–579 (1997).

[129] J.-W. Pan, D. Bouwmeester, H. Weinfurter, and A. Zeilinger, "Experimental Entanglement Swapping: Entangling Photons That Never Interacted", Physical Review Letters **80**, 3891–3894 (1998).

[130] S. L. Braunstein and A. Mann, "Measurement of the Bell operator and quantum teleportation", Physical Review A **51**, R1727–R1730 (1995).

[131] S. Massar and S. Popescu, "Optimal Extraction of Information from Finite Quantum Ensembles", Physical Review Letters **74**, 1259–1263 (1995).

[132] J. B. Altepeter, E. R. Jeffrey, P. G. Kwiat, S. Tanzilli, N. Gisin, and A. Acín, "Experimental Methods for Detecting Entanglement", Physical Review Letters **95**, 033601 (2005).

[133] A. G. White, A. Gilchrist, G. J. Pryde, J. L. O'Brien, M. J. Bremner, and N. K. Langford, "Measuring two-qubit gates", Journal of the Optical Society of America B **24**, 172 (2007).

[134] W. K. Wootters, "Entanglement of Formation of an Arbitrary State of Two Qubits", Physical Review Letters **80**, 2245–2248 (1998).

[135] S. Ghosh, G. Kar, A. Sen(De), and U. Sen, "Mixedness in the Bell violation versus entanglement of formation", Physical Review A **64**, 044301 (2001).

[136] H. F. Chau, "Practical scheme to share a secret key through a quantum channel with a 27.6% bit error rate", Physical Review A **66**, 060302 (2002).

[137] A. Hardy, D. Welch, and W. Streifer, "Analysis of second-order gratings", IEEE Journal of Quantum Electronics **25**, 2096–2105 (1989).

[138] L. Rickert, T. Kupko, S. Rodt, S. Reitzenstein, and T. Heindel, "Optimized designs for telecom-wavelength quantum light sources based on hybrid circular Bragg gratings", Optics Express **27**, 36824 (2019).

[139] L. Sapienza, M. Davanço, A. Badolato, and K. Srinivasan, "Nanoscale optical positioning of single quantum dots for bright and pure single-photon emission", Nature Communications **6** (2015).

[140] J. Liu, M. I. Davanço, L. Sapienza, K. Konthasinghe, J. V. De Miranda Cardoso, J. D. Song, A. Badolato, and K. Srinivasan, "Cryogenic photoluminescence imaging system for nanoscale positioning of single quantum emitters", Review of Scientific Instruments **88**, 023116 (2017).

[141] M. Tong, D. G. Ballegeer, A. Ketterson, E. J. Roan, K. Y. Cheng, and I. Adesida, "A comparative study of wet and dry selective etching processes for GaAs/AIGaAs/lnGaAs pseudomorphic MODFETs", Journal of Electronic Materials **21**, 9–15 (1992).

[142] S. van der Walt, J. L. Schönberger, J. Nunez-Iglesias, F. Boulogne, J. D. Warner, N. Yager, E. Gouillart, and T. Yu, "Scikit-image: image processing in Python", PeerJ **2**, e453 (2014).

[143] P. V. Hough, "Machine analysis of bubble chamber pictures", in Proc. of the international conference on high energy accelerators and instrumentation, sept. 1959 (1959), pp. 554–556.

[144] M. Köfferlein, *Klayout - your mask layout friend*, `https://www.klayout.de/` (visited on 12/21/2020).

[145] K. Nojiri, *Dry etching technology for semiconductors* (Springer, New York, 2014).

[146] G. Pettinari, A. Gerardino, L. Businaro, A. Polimeni, M. Capizzi, M. Hopkinson, S. Rubini, F. Biccari, F. Intonti, A. Vinattieri, M. Gurioli, and M. Felici, "A lithographic approach for quantum dot-photonic crystal nanocavity coupling in dilute nitrides", Microelectronic Engineering **174**, 16–19 (2017).

[147] E. L. Hu and R. E. Howard, "Reactive ion etching of GaAs in a chlorine plasma", Journal of Vacuum Science & Technology B: Microelectronics and Nanometer Structures **2**, 85 (1984).

[148] Y. Su, Y. Juang, S. Shei, and B. Fang, "A study of selective and nonselective reactive ion etching of GaAs/AlGaAs materials", Solid-State Electronics **36**, 1779–1785 (1993).

[149] D. A. Danner, M. Dalvie, and D. W. Hess, "Plasma Etching of Aluminum: A Comparison of Chlorinated Etchants", Journal of The Electrochemical Society **134**, 669–673 (1987).

[150] H. Wang, Y.-M. He, T.-H. Chung, H. Hu, Y. Yu, S. Chen, X. Ding, M.-C. Chen, J. Qin, X. Yang, R.-Z. Liu, Z.-C. Duan, J.-P. Li, S. Gerhardt, K. Winkler, J. Jurkat, L.-J. Wang, N. Gregersen, Y.-H. Huo, Q. Dai, S. Yu, S. Höfling, C.-Y. Lu, and J.-W. Pan, "Towards optimal single-photon sources from polarized microcavities", Nature Photonics **13**, 770–775 (2019).

[151] R. Trotta, E. Zallo, C. Ortix, P. Atkinson, J. D. Plumhof, J. van den Brink, A. Rastelli, and O. G. Schmidt, "Universal Recovery of the Energy-Level Degeneracy of Bright Excitons in InGaAs Quantum Dots without a Structure Symmetry", Physical Review Letters **109**, 147401 (2012).

[152] S. Manna, H. Huang, S. F. C. da Silva, C. Schimpf, M. B. Rota, B. Lehner, M. Reindl, R. Trotta, and A. Rastelli, "Surface passivation and oxide encapsulation to improve optical properties of a single GaAs quantum dot close to the surface", Applied Surface Science **532**, 147360 (2020).

[153] M. Moczała-Dusanowska, Ł. Dusanowski, O. Iff, T. Huber, S. Kuhn, T. Czyszanowski, C. Schneider, and S. Höfling, "Strain-Tunable Single-Photon Source Based on a Circular Bragg Grating Cavity with Embedded Quantum Dots", ACS Photonics **7**, 3474–3480 (2020).

[154] D. Ziss, J. Martín-Sánchez, T. Lettner, A. Halilovic, G. Trevisi, R. Trotta, A. Rastelli, and J. Stangl, "Comparison of different bonding techniques for efficient strain transfer using piezoelectric actuators", Journal of Applied Physics **121**, 135303 (2017).

[155] P. Gold, A. Thoma, S. Maier, S. Reitzenstein, C. Schneider, S. Höfling, and M. Kamp, "Two-photon interference from remote quantum dots with inhomogeneously broadened linewidths", Physical Review B **89**, 035313 (2014).

[156] V. Giesz, S. L. Portalupi, T. Grange, C. Antón, L. De Santis, J. Demory, N. Somaschi, I. Sagnes, A. Lemaître, L. Lanco, A. Auffèves, and P. Senellart, "Cavity-enhanced two-photon interference using remote quantum dot sources", Physical Review B **92**, 161302 (2015).

[157] R. Stockill, M. J. Stanley, L. Huthmacher, E. Clarke, M. Hugues, A. J. Miller, C. Matthiesen, C. Le Gall, and M. Atatüre, "Phase-Tuned Entangled State Generation between Distant Spin Qubits", Physical Review Letters **119**, 010503 (2017).

[158] A. Thoma, P. Schnauber, J. Böhm, M. Gschrey, J.-H. Schulze, A. Strittmatter, S. Rodt, T. Heindel, and S. Reitzenstein, "Two-photon interference from remote deterministic quantum dot microlenses", Applied Physics Letters **110**, 011104 (2017).

[159] M. Zopf, T. Macha, R. Keil, E. Uruñuela, Y. Chen, W. Alt, L. Ratschbacher, F. Ding, D. Meschede, and O. G. Schmidt, "Frequency feedback for two-photon interference from separate quantum dots", Physical Review B **98**, 161302 (2018).

[160] J. H. Weber, B. Kambs, J. Kettler, S. Kern, J. Maisch, H. Vural, M. Jetter, S. L. Portalupi, C. Becher, and P. Michler, "Two-photon interference in the telecom C-band after frequency conversion of photons from remote quantum emitters", Nature Nanotechnology **14**, 23–26 (2019).

[161] J. H. Weber, J. Kettler, H. Vural, M. Müller, J. Maisch, M. Jetter, S. L. Portalupi, and P. Michler, "Overcoming correlation fluctuations in two-photon interference experiments with differently bright and independently blinking remote quantum emitters", Physical Review B **97**, 195414 (2018).

[162] F. Basso Basset, M. Valeri, E. Roccia, V. Muredda, D. Poderini, J. Neuwirth, N. Spagnolo, M. B. Rota, G. Carvacho, F. Sciarrino, and R. Trotta, "Quantum key distribution with entangled photons generated on demand by a quantum dot", Science Advances **7**, eabe6379 (2021).

[163] A. Acín, S. Massar, and S. Pironio, "Efficient quantum key distribution secure against no-signalling eavesdroppers", New Journal of Physics **8**, 126–126 (2006).

[164] M. Bock, A. Lenhard, C. Chunnilall, and C. Becher, "Highly efficient heralded single-photon source for telecom wavelengths based on a PPLN waveguide", Optics Express **24**, 23992 (2016).

[165] E. Waks, A. Zeevi, and Y. Yamamoto, "Security of quantum key distribution with entangled photons against individual attacks", Physical Review A **65**, 052310 (2002).

[166] S. Guha, H. Krovi, C. A. Fuchs, Z. Dutton, J. A. Slater, C. Simon, and W. Tittel, "Rate-loss analysis of an efficient quantum repeater architecture", Physical Review A **92**, 022357 (2015).

Acknowledgments

I am a great believer of collaboration among human beings and this thesis is the living proof of what can be done when meeting the right people.

To take a train to go to a wonderful place one just needs to present himself at the station at the right time with a ticket and jump in. This is the image I get when I look back at the academic journey that led me to write this last Section of my thesis. My only merit was being able to put myself in the right place at the right time, the rest just went by itself.

My biggest thanks goes to my supervisor, Prof. Rinaldo Trotta. He led me into the world of quantum and opened me the door to work together with an international group of excellent scientists. His leadership and scientific supervision always pulled out the best out of me. He helped me discover my value as a researcher and as a person. I value him as a scientific father, an older brother, and a close friend.

I feel very lucky to be a colleague of Dr. Francesco Basso Basset. Since the first time we met in Linz a deep feeling of friendship was established. His kind manners, his deep knowledge and foolproof method have been a great guidance and a security in the laboratory in these three years.

I would like to thank Dr. Davide Tedeschi, long lasting colleague, for his incredible support and the hard work we shared over the years. I have been enriched by his views on life and I wish him all the best for his new career.

I would like to thank Julia Neuwirth for her enthusiasm in any aspect of our laboratory life, both scientific and human. I would also like to thank all the other components of the Nanophotonics group, Emanuele Roccia, Matteo Savaresi, Giuseppe Ronco, Francesco Salusti, Federico Trezzini, and Claudio Pardo. Thank you for creating a splendid environment in the laboratory, each one of you with his own gifts. Thanks for all the meals we shared, the discussions we had, the chess matches we played, and all the music we listened together. A special thanks goes to Gabriele Lovicu, which suffered the accident of being under my supervision during his master thesis and managed to survive. Last, a huge thanks to Antonio Miriametro, the almighty technician of our Department, for repairing anything we managed to break.

A big thank you goes to the group of Minions which helped us building the laboratory when there was nothing more than a room and two optical tables: Christian Schimpf, Dr. Katharina D. Zeuner, and Prof. Klaus D. Jöns. The amount of work we did together was matched only by the amount of good food we ate during your visit.

I would like to thank Prof. Armando Rastelli of JKU in Linz for giving me the opportunity to visit his group and spend a fundamental part of my thesis in the cleanroom facilities of his Institute. His approach to science and his acute intelligence won my admiration and I am glad of having the opportunity to collaborate with him. I would like to thank Tobias M. Krieger, which started with me the journey into the terrible world of cavity processing. I saw him growing in his scientific abilities and I was given the opportunity to lead him in this process. I would like to thank Dr. Xueyong Yuan, Dr. Saimon F. Covre da Silva, Huiying Huang, Johannes Aberl, and Dr. Javier Martín-Sánchez for having shared with me their expertise and for their help in the cleanroom, and Dr. Santanu Manna for his help with the simulations of the CBR cavities. I would also like to thank all the technicians of the Institute, in particular Alma Halilovic, Ursula Kainz, and Albin Schwarz, without their support all this work would not have been possible, and the secretariat of the Institute, Susanne Schwind, true deus ex machina for any difficult administrative situation in Linz.

A special thanks goes to Dr. Giorgio Pettinari, who hosted me in the cleanroom of the CNR and helped me to continue the processing of optical cavities in Rome. He taught me all the best tricks to use in a cleanroom and introduced me to the dangerous world of dry etching. A great thanks also to our collaborator in Würzburg, Dr. Magdalena Moczała-Dusanowska and Quirin Buchinger, the high quality of their work allowed for some of the beautiful results shown in this thesis.

I would like to thank also the Ph.D. secretariat in Rome, Alba Perrotta, and the Ph.D. coordinator, Prof. Fabio Sciarrino, for all their support and hard work, especially during these trying times of the pandemic.

Last, I would like to thank all the people which shared a part of this journey with me. You are too many to write here and to remember, and you will excuse me if I forgot somebody.